

The Pennsylvania State University

The Graduate School

College of Engineering

**MAGNETOELECTRIC FLEXURAL GATE TRANSISTOR WITH NANOTESLA  
SENSITIVITY**

A Dissertation in

Electrical Engineering

by

Feng Li

© 2012 Feng Li

Submitted in Partial Fulfillment

of the Requirements

for the Degree of

Doctor of Philosophy

Aug 2012

The thesis of Feng Li was reviewed and approved\* by the following:

Suman Datta  
Monkowsi Professor of Electrical Engineering  
Dissertation Advisor  
Co-Chair of Committee

Qiming Zhang  
Distinguished Professor of Electrical Engineering  
Dissertation Co-Advisor  
Co-Chair of Committee

Srinivas Tadigadapa  
Professor of Electrical Engineering

Yuan Xie  
Professor of Computer Science Engineering

Kultegin Aydin  
Professor and Interim Department Head of Electrical Engineering

\*Signatures are on file in the Graduate School

## ABSTRACT

In this dissertation, we have successfully demonstrated the prototype of a chip-scale magnetoelectric (ME) sensor system at room temperature towards biomedical imaging applications, such as magnetocardiography (MCG), magnetoencephalography (MEG). Preliminary results on different approaches to enhance bulk laminate sensor performance have been investigated together with my colleague by Zhao Fang. To achieve sensor integration, an easily controlled deposition process—ion milling sputtering for Metglas<sup>®</sup> ( $\text{Fe}_{85}\text{Si}_{10}\text{B}_5$ ) thin film has been developed and in-situ magnetic domain alignment can be accomplished at room temperature as the film is being deposited. The thin film has been characterized by X-ray Photoelectron Spectroscopy (XPS) for atom composition, SQUID measurement for domain alignment and deflection measurement for magnetostrictive (MS) coefficient.

The first direct integration of thin film Metglas<sup>®</sup>/  $\text{Pb}(\text{Zr}_{0.52}\text{Ti}_{0.48})\text{O}_3$  (PZT) cantilevers shows the quality factor enhancement at the resonant frequency and sensitivity of 1.8 V/T. To improve the integrated sensor performance, a Metglas<sup>®</sup> thin film based magnetoelectric flexural gate transistor (MEFGT) has been realized with the capability of tiny vector magnetic field sensing. The device combines the benefits of high-deflection property of MS cantilever sensors with FET based motion sensing by integrating a magnetostrictive thin film micromechanical cantilever directly atop a sensing and amplifying transistor. Both optical and electrical measurements show the advantage of MEFGT in small magnetic field detection. A sensitivity of 1.5 mV/ $\mu\text{T}$ , which corresponds to 150 pT/ $\sqrt{\text{Hz}}$  minimum detectable field (MDF), has been reported as the most sensitive integrated ME sensor to date.

Post simulations of MEFGT have been done to analyze both the mechanical and electrical performance. Device noise modeling and analysis on transistor flicker noise has been established. A strained  $\text{Si}_{0.5}\text{Ge}_{0.5}$  quantum well FET is introduced as the readout transistor

candidate which exhibits the lowest reported flicker noise performance for future low noise sensor devices.

Building on the results of MEFGTs, several readout circuits has been demonstrated. Onboard signal conditioning circuits of charge mode and voltage mode have been realized for both bulk sensors and thin film sensors. Design and simulation for the front-end readout amplifier has been also demonstrated for the on-chip magnetic sensor system. Moreover, post signal processing circuit for real time brain wave signal has been proposed by using a customer designed lock-in amplifier.

## TABLE OF CONTENTS

LIST OF FIGURES .....	vii
LIST OF TABLES .....	xii
ACKNOWLEDGEMENTS .....	xiii
Chapter 1 Introduction .....	1
1.1 Magnetic Sensor Overview .....	1
1.2 Research Objectives and Thesis Organization .....	7
Chapter 2 Magnetolectric Laminates Bulk Sensors (Preliminary Results) .....	11
2.1 Magnetic Flux Concentration Effect .....	13
2.2 Multilayer Structure .....	16
2.3 Resonance Enhancement .....	18
2.4 Single Crystal Piezoelectric Laminates .....	20
Chapter 3 Magnetostrictive Thin Films .....	22
3.1 Magnetostrictive Materials .....	23
3.2 Deposition System and Conditions .....	25
3.3 Magnetic Characterization .....	28
Chapter 4 Thin Film Magnetolectric Sensors .....	33
4.1 Thin Film Magnetolectric Laminate Cantilever Sensors .....	33
4.1.1 Fabrication Process .....	33
4.1.2 Sensor Performance .....	36
4.2 Magnetolectric Flexural Gate Transistors .....	43
4.2.1 Design Considerations .....	43
4.2.2 MEFGT Fabrication .....	46
4.2.3 MEFGT Performance .....	51
4.2.4 MEFGT Noise Modeling .....	66
4.2.5 SiGe Quantum Well Transistors Noise Modeling .....	69
Chapter 5 Front End Readout Circuit Design and Simulation .....	80
5.1 Signal Conditioning Circuit Design .....	80
5.2 Post Signal Processing Circuit .....	83
5.2.1 Front End Operational Amplifier Design .....	85
5.2.2 On-chip Lock in Amplifier .....	88

Chapter 6 Conclusions and Future Work.....	92
6.1 Conclusion.....	92
6.2 MEFGT Sensitivity Improvement.....	95
6.3 In-plane Magnetoelectric Flexural gate Transistors:.....	98
Reference .....	101
Appendix A Metglas <sup>®</sup> /PZT ME Cantilever Process Flow .....	111
Appendix B Metglas <sup>®</sup> MEFGT Process Flow .....	113
Appendix C Process Facilities .....	116

## LIST OF FIGURES

Figure 1-1. Magnetic Sensor Market 2012. ....	1
Figure 1-2. Estimate of sensitivity of different magnetic sensors. ....	2
Figure 1-3. Schematic of SQUID. ....	2
Figure 1-4. The basic fluxgate principle. The ferromagnetic core is excited by the ac current into the excitation winding. If the measure dc field is present, the associated core flux is changing and this results in an output induced voltage in the pickup coil. ...	3
Figure 1-5. Spin valve TMR configuration: an antiparallel is shown on the right and a parallel on the left. FM stands for ferromagnetic metal, ITB for insulating tunnel barrier, $\uparrow$ is a spin up electron and $\downarrow$ is a spin down electron. The vertical black arrows in the FM layers show the direction of the magnetization. The arrows across the spin valves show the electron path. A bend in the path shows that an electron was scattered. ....	4
Figure 1-6. Schematic of Hall Effect sensors. ....	5
Figure 1-7. Schematic of a magnetoelectric laminate. ....	6
Figure 1-8. Comparison of several low-field magnetic sensor technologies. Sensitivity and cost indicated for each sensor. ....	7
Figure 2-1. Illustration of (a) magnetostriction (b) piezoelectricity (c) magnetoelectricity. ...	12
Figure 2-2. (a) Magnetic flux density distribution in Metglas <sup>®</sup> under a uniform external magnetic field in free space; (b) Magnetic flux density of the Metglas <sup>®</sup> sheet along the x-axis (length direction) at $y=0, z=0$ (The origin is at the center of Metglas <sup>®</sup> sheet) with various aspect ratios of $W_m/L_m$ . (The length and thickness are fixed at 30 mm and 25 $\mu\text{m}$ respectively, and the width $W_m$ is varied from 20mm to 1 mm). The external magnetic field is 1 Oe ( $10^{-4}$ T) [30]. ....	14
Figure 2-3. (a) $\alpha_{ME}$ as a function of dc bias magnetic field for Metglas <sup>®</sup> /PVDF laminates with PVDF bonded on different regions of Metglas <sup>®</sup> sheet. (b) $\alpha_{ME}$ as a function of dc bias magnetic field for Metglas <sup>®</sup> /PVDF laminates with varying $W_m$ . The data was measured at 20 Hz and $H_{ac}=0.38$ Oe [30]. ....	15
Figure 2-4 (a) ME voltage of the sensor system as a function of dc bias magnetic field for Metglas <sup>®</sup> /PVDF laminates with different number of PVDF layers. The data were measured at 200 Hz and ac magnetic field $H_{ac}=0.08$ Oe. (b) Comparison of experimentally measured ME voltage with analytical estimation [78]. ....	17

Figure 2-5. (a) $\alpha_{ME}$ coefficient as a function of frequency for a ME laminate sensor with Metglas <sup>®</sup> /PZT, showing an enhanced sensitivity at the resonance, 78 kHz. (b) $\alpha_{ME}$ as a function of frequency for Metglas <sup>®</sup> /PZT laminate composites in FF, FC, and CC modes. The Metglas <sup>®</sup> layer is 10 mm×1 mm×25 $\mu$ m and PZT layer is 5mm×1 mm×100 $\mu$ m (Inset: Schematic for different structures.).....	19
Figure 2-6. (a) $\alpha_{ME}$ as a function of dc bias magnetic field for Metglas <sup>®</sup> /PMN-PT laminates with different cut orientation and cut direction of single crystal PMN-PT. The data were measured at 20 Hz and $H_{ac}$ =0.8 Oe. (b) $\alpha_{ME}$ as a function of frequency for Metglas <sup>®</sup> /PMN-PT laminates with different cut orientation and cut direction of single crystal PMN-PT.....	21
Figure 3-1. (a) Magnetostriction and (b) Magnetostrictive coefficient as a function of magnetic field for Terfenol-D (red), Galfenol (blue) and Metglas <sup>®</sup> (black). .....	24
Figure 3-2. Ion Mill Sputtering System Schematic.....	26
Figure 3-3. Schematic of In-situ magnetization Ion Mill Sputtering system. ....	27
Figure 3-4. XPS results at 100nm depth of Metglas films.....	28
Figure 3-5. Hysteresis B-H loop measured by SQUID system.....	29
Figure 3-6. (a) Magnetostrictive coefficient measurement setup. (b) Magnetostrictive coefficient comparison between normal sputtering and In-situ magnetization process. (c) Magnetostrictive coefficient of Metglas <sup>®</sup> thin films as a function of DC bias magnetic field (black dot: parallel field; red circle: perpendicular field). .....	32
Figure 4-1. Schematic of ME laminate cantilever sensor. ....	33
Figure 4-2. ME cantilever process flow.....	35
Figure 4-3. SEM image for the released ME cantilevers. ....	35
Figure 4-4. SEM image for the released ME cantilevers. ....	37
Figure 4-5. ME output voltage as a function of dc bias Magnetic field (The inset shows the measurement schematic). The data were measured at 20 Hz and $H_{ac} = 0.7$ Oe. ....	37
Figure 4-6. ME coefficient as a function of dc bias magnetic field: measurement versus calculation results.....	38
Figure 4-7. ME coefficient frequency response.....	39
Figure 4-8. Equivalent circuit for ME cantilever sensor and charge amplifier with noise source. ....	40
Figure 4-9. (a) Frequency response of ME laminate cantilever sensor capacitance and dielectric loss factor. (b) Sensor output noise density.....	42

Figure 4-10. (a) Schematic of the magnetoelectric flexural gate transistor (MEFGT). (b) The principle of operation of a magnetoelectric flexural gate transistor (MEFGT). .....	45
Figure 4-11. Schematic of the fabrication process (not to scale). (a) Deposition of 1 $\mu\text{m}$ thermal field oxide on p-type silicon wafer. (b) Pattern and wet etch field oxide for source drain formation via solid source diffusion. (c) Gate oxide pattern and deposition. (d) Gate electrode metallization using liftoff process. (e) Deposition of 500 nm-thick amorphous silicon for the sacrificial layer and lift-off Metglas/Ti. (f) Patterning to prevent unwanted undercutting during release step and release cantilever structure using $\text{XeF}_2$ isotropic etching. ....	49
Figure 4-12. (a) Scanning Electron Microscopy (SEM) of magnetoelectric flexural gate transistor (MEFGT). (b) A 300 $\mu\text{m}$ long and 100 $\mu\text{m}$ wide flexural gate.....	50
Figure 4-13. White light optical interference microscope (Zygo <sup>®</sup> NT100) image of the freestanding magnetostrictive top flexural cantilever gate structure (a) without annealing (b) with 350 $^{\circ}\text{C}$ annealing for 5 min. ....	52
Figure 4-14. (a) Schematic of optical measurement set-up using position sensitive photo detector. (b) PSD output varies linearly with input magnetic field. (Signal generator provides a triangle wave with 95%-5% symmetry at a frequency of 0.01 Hz, 5.95 $V_{pp}$ , with an offset of 3.0 V.) .....	54
Figure 4-15. Schematic of ac magnetic field measurement set-up. $H_{in}$ is the AC magnetic field to be detected. $H_{DC}$ is the DC bias magnetic field. ....	55
Figure 4-16. Flexural gate air gap capacitance (black) and differential capacitance (red) as a function of the applied magnetic bias field. ....	56
Figure 4-17. Three-dimensional view of the cantilever with the analytical 2D Bow approximation. ....	59
Figure 4-18. Three-dimensional view of the cantilever with the COMSOL <sup>®</sup> 3D simulation structure. ....	59
Figure 4-19. Differential capacitance versus DC magnetic bias field: comparison between measurement, 3D COMSOL simulation and 2D analytical approximation.....	60
Figure 4-20. Transfer characterization of common source readout circuit. ....	61
Figure 4-21. Small signal equivalent circuit for MEFGT. ....	61
Figure 4-22. Output voltage of common source readout amplifier circuit as a function of the DC magnetic field. The data was measured at 20 Hz and $H_{in} = 0.38$ Oe. ....	62
Figure 4-23. MEFGT frequency response measurement and simulation in both air and vacuum. ....	63
Figure 4-24. Output noise performance of MEFGT. ....	65

Figure 4-25. Frequency spectrum of 3 nanoTesla input ac magnetic field. (The DC magnetic bias field is set at 7 Oe. 3nT AC magnetic field is the minimum generated by the measurement setup.).....	65
Figure 4-27. (a) Measured effective hole mobility as a function of hole density for p-channel Si <sub>0.50</sub> Ge <sub>0.50</sub> QWFETs and Si MOSFETs (b) Six band k·p simulation of heavy and light hole energy dispersion for strained Si <sub>0.50</sub> Ge <sub>0.50</sub> QW and unstrained silicon (c) Measured interface state profile via charge pumping measurements.....	73
Figure 4-28. Normalized power spectral density (NPSD) of I <sub>d</sub> fluctuations ( $S_{I_d}/I_d^2$ ) in unstrained Si pMOSFETs and Si <sub>0.50</sub> Ge <sub>0.50</sub> strained QWFETs as a function of gate over drive voltage. The drain voltage is -50 mV. (b) NPSD of Si <sub>0.50</sub> Ge <sub>0.50</sub> strained QWFETs compared against Si pMOSFETs showing almost 10X improvement in noise spectral density at 10 Hz, especially at high gate voltage. The drain voltage is -50 mV.....	75
Figure 4-29. The equivalent input gate voltage noise characteristics, $S_{V_G} = S_{I_d}/g_m^2$ in (a) unstrained Si pMOSFETs and (b) Si <sub>0.50</sub> Ge <sub>0.50</sub> strained QWFETs as a function of gate over drive voltage. The drain voltage is -50 mV. The models used are correlated mobility fluctuation model (CMF) and Hooge mobility fluctuation model.....	77
Figure 4-30. (a) The normalized drain noise characteristics, $S_{I_d}/I_d^2$ , in Si <sub>0.50</sub> Ge <sub>0.50</sub> strained QWFETs and Si MOSFETs (ours and from Ref 73) (b) Extracted Hooge parameter as a function of gate overdrive voltage. ....	79
Figure 5-1. Two type of models for sensor: charge model and voltage model.....	80
Figure 5-2. Circuit diagram for (a) charge mode and (b) voltage mode amplifier. ....	81
Figure 5-3. Frequency response comparisons for voltage mode and charge mode readout circuit. ....	82
Figure 5-4. Schematic of post signal processing circuit for ME sensor.....	84
Figure 5-5. Circuit diagram for the operation amplifier with biasing circuit.....	85
Figure 6-1. MEFGT sensitivity benchmarked with current magnetic sensing technologies. ..	94
Figure 6-2. SNR as a function of effective air gap. The MEFGT shows the potential to achieve pico Tesla minimum AC magnetic field detection capability.....	95
Figure 6-3. SiGe buried channel transistor as a candidate for low noise application (a) schematic of Si surface channel FETs and SiGe quantum well FETs. (b) Flicker noise improvement. ....	97
Figure 6-4. The principle of operation of an in-plane ME RGT.....	99
Figure 6-5. (a) Micron strain gauge analytical modeling. (b) Interdigitated electrode (IDE) gate design.....	100



**LIST OF TABLES**

Table 1-1. The human brain magnetic-electric signal.....	8
Table 3-1. Ion Mill Sputtering Conditions.....	26
Table 3-2. XPS Atom Composition.....	29
Table 4-1. Parameters for Metglas <sup>®</sup> Flexural gate.....	60
Table 6-1. Resolution Comparison.....	93

## ACKNOWLEDGEMENTS

I would like to express my great gratitude to my advisor Professor Suman Datta for his guidance, support, and the stimulating discussions. Thanks to Dr. Qiming Zhang, my co-advisor, for those valuable guidance and advises. I would also like to thank my thesis committee members, Dr. Srinivas Tadigadapa for his time and discussion with device design and fabrication and Dr. Yuan Xie for his suggestions and helps on the circuit design.

This work has been made possible by a large group of collaborators, colleagues, and friends. First, I would like to thank all of the members of the research group Nanoelectronic Devices and Circuits Lab (NDCL) at Penn State, particularly Mr. Euichul Hwang and Dr. Ashkar Ali for mentoring and helping me the process fabrication. Second, I would like to thank the members in Dr. Thomas Jackson research group including Dr. Dalong Zhao, Ms. Yuanyuan Li, and especially Mr. Jose Israel Ramirez for the Ion Milling Sputtering. Third, I would like to thank Ms. Jing Xie, Yufei Wu, Mr. Lei Mei, Ninad Mokhariwale, Chris Curwen, and particularly Dr. Zhao Fang and Dr. Rajiv Misra for the exciting and fruitful collaboration. Specially, my appreciation gives to all collaborators from Penn State, National Nanotechnology Infrastructure Network (NNIN) for their help and support of all the fabrication in this work.

Finally, I would like to thank my family for their endless love, support, and encouragement over so many years of study.

This work was financially supported by NSF under grant No. ECCS-0824202 and Department of Electrical Engineering in the Pennsylvania State University.

## Chapter 1 Introduction

### 1.1 Magnetic Sensor Overview

Magnetic sensing technology has played an important role in electronics industry for many years and spreads a wide range of applications in automobiles, data storage, geophysical detection, and health care. It is expected that the magnetic sensor market will have an over \$1.5 billion in year 2011 with an increasing growth rate of 8.7% each year. As we can see in Fig. 1-1, Hall Effect sensors dominate with more than 70% market share, while newer technologies such as flux gate sensor, anisotropic magnetoresistance (AMR) and giant magnetoresistance (GMR) sensor are gradually gaining visibility. SQUID (superconducting quantum interference device) and other advanced magnetic sensing technologies such as spin resonance sensors stand the rest of the market.

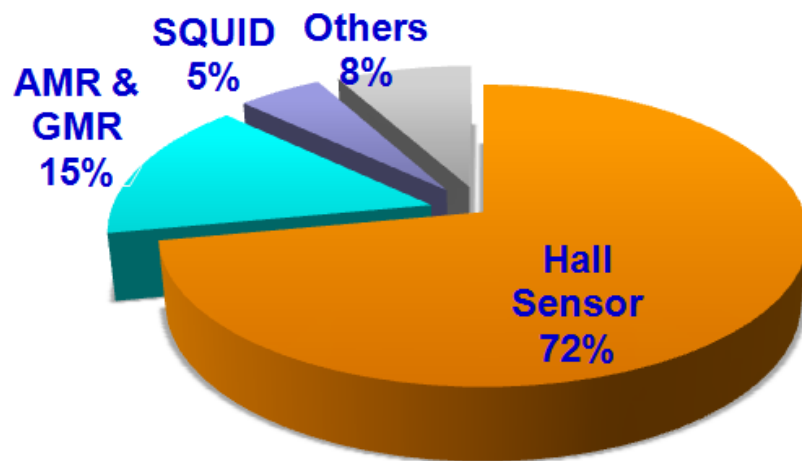


Figure 1-1. Magnetic Sensor Market 2012.



Fluxgate sensors measure the magnitude and direction of the dc or low-frequency ac magnetic field in the range of approximately  $10^{-11}$  to  $10^{-4}$  T, as shown in Fig. 1-4. The ferromagnetic core is excited by the ac current into the excitation winding and the output induced voltage in the pickup coil is proportional to the input DC magnetic field due to the associated core flux change. The frequency response of the sensor is limited by the excitation field and the response time of the ferromagnetic material [2]. The fluxgate sensor is widely used in the navigation and astronomical applications.

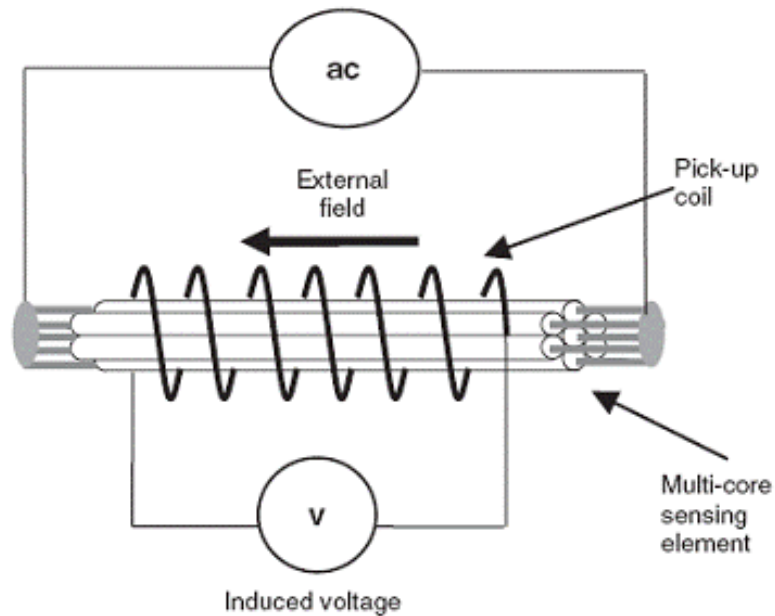


Figure 1-4. The basic fluxgate principle. The ferromagnetic core is excited by the ac current into the excitation winding. If the measure dc field is present, the associated core flux is changing and this results in an output induced voltage in the pickup coil.

Magnetoresistive magnetometers use a change in resistance  $\Delta R$  caused by an external magnetic field  $H$ . Figure 1-5 shows a typical example of magnetoresistive sensor, spin valve tunnel magnetoresistance (TMR) sensor. An electron passing through the spin-valve will be scattered more if the spin of the electron is opposite of the direction of the magnetization in the

ferromagnetic metal (FM) layer. This principle is used to construct an equivalent electric circuit representation of the two configurations of the spin-valve. Computation of the equivalent resistance for the antiparallel and parallel configurations shows that the parallel alignment has the lower resistance. Besides the traditional sensing applications, TMR has triggered the rise of a new field of electronics—spintronics which has been used extensively in the read heads of modern hard drives and magnetic sensors.

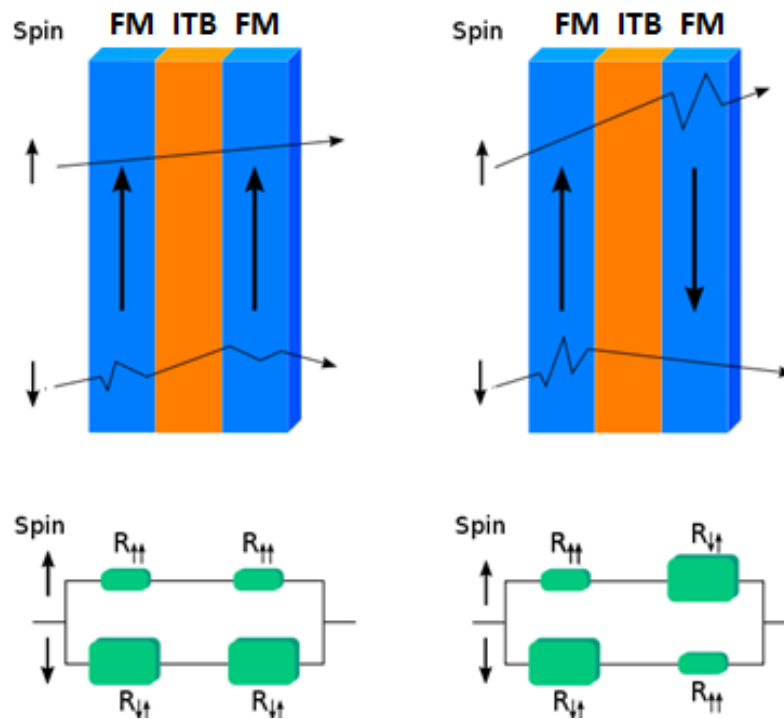


Figure 1-5. Spin valve TMR configuration: an antiparallel is shown on the right and a parallel on the left. FM stands for ferromagnetic metal, ITB for insulating tunnel barrier,  $\uparrow$  is a spin up electron and  $\downarrow$  is a spin down electron. The vertical black arrows in the FM layers show the direction of the magnetization. The arrows across the spin valves show the electron path. A bend in the path shows that an electron was scattered.

The Hall Effect sensor [3] is a widely used, low cost sensor whose operation is illustrated in Fig.

1-6. The sensor exploits a physical phenomenon discovered by Edwin H. Hall more than 100

years ago. He found that a voltage difference appears across a thin rectangle of gold placed in a strong magnetic field perpendicular to the plane of the rectangle when an electric current is sent along its length. An electron moving through a magnetic field experiences a force, known as the Lorentz force, that is perpendicular both to its direction of motion and to the direction of the field. It is the response to this force that creates the Hall voltage. Hall Effect sensors are generally made of silicon with a sensitivity range of 1 mT to 0.1 T. Higher sensitivity as low as 100 nT can be reached by III-V semiconductor indium antimonide.

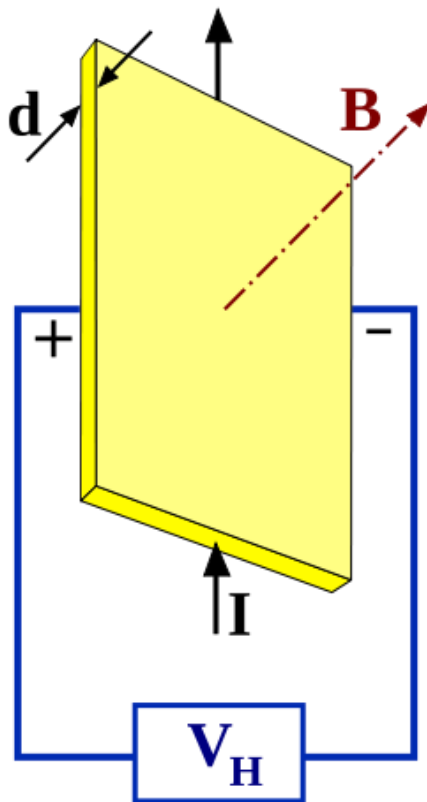


Figure 1-6. Schematic of Hall Effect sensors.

The magnetoelectric (ME) effect is the phenomenon of inducing electric polarization by applying an external magnetic field. Single phase magnetoelectrics were first shown in  $\text{Cr}_2\text{O}_3$  with a linear

coupling effect in 1959 [4]. For the past decade, composite laminate materials consisted of magnetostrictive layer and piezoelectric layer have drawn much attention due to the strong strain coupling effects [5-9]. Among various composite configurations investigated, the multilayer structures, comprising of alternating magnetostrictive alloy layer and piezoelectric layer with (Metglas<sup>®</sup> (FeSiB) /Pb(ZrTi)O<sub>3</sub> (PZT)) as schematically illustrated in Fig. 1-7, have shown picotesla sensitivity.

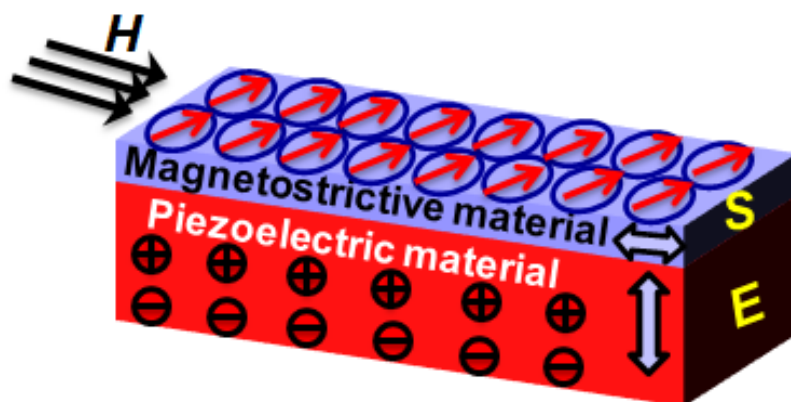


Figure 1-7. Schematic of a magnetolectric laminate.

## 1.2 Research Objectives and Thesis Organization

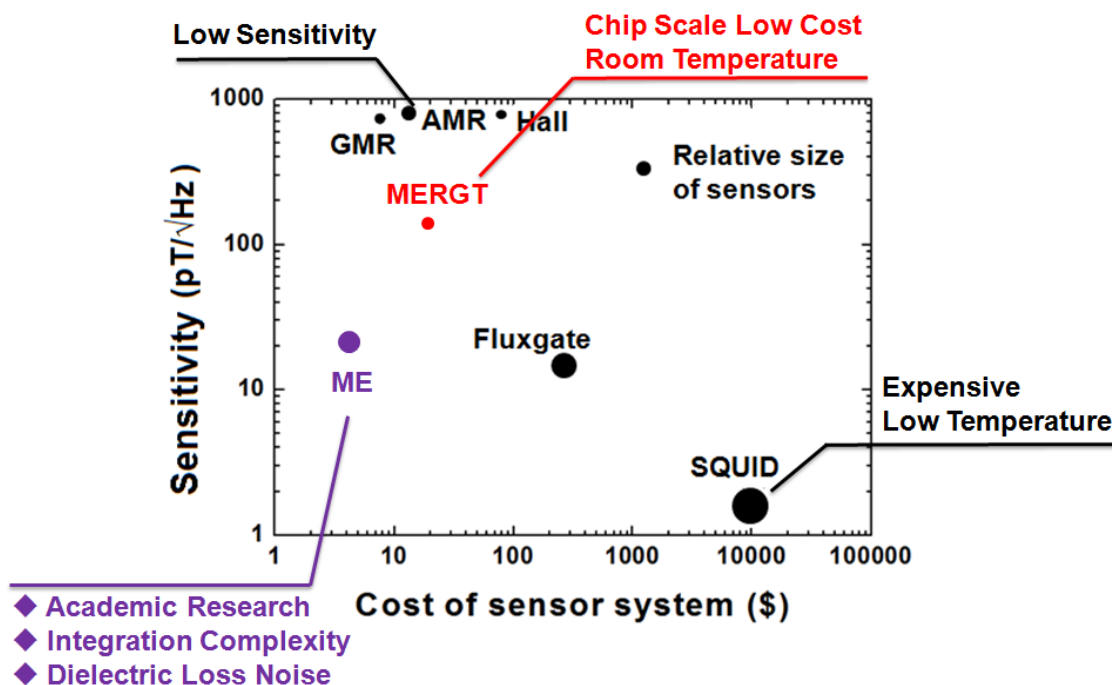


Figure 1-8. Comparison of several low-field magnetic sensor technologies. Sensitivity and cost indicated for each sensor.

Figure 1-8 shows the comparison of different magnetic sensing technologies listed previously. Hall Effect sensors and GMR sensors express the low cost, low power and small size properties; however, it hits the noise level of both. Fluxgate sensors have a better sensitivity near picoTesla, but the miniaturization of the sensor limits its applications in high special resolution. Spin resonance sensors and SQUID exhibit an extreme low sensitivity and extensive detectable range but a high price, high power consumption, large system volume and especially low temperature operation. For magnetoelectric sensors, it reveals a relatively larger size in comparison to Hall Effect sensors or magnetoresistive sensors yet lower cost and better sensitivity. This draws an

attractive research topic: for tiny magnetic field detection, which sensor system shows the best performance – portable, costless and still sensitive? Till date, most weak bio-magnetic signal detection is performed in bio-medical area such as magnetoencephalography (MEG). Typical human brain magnetic field produced by the neuronal currents is ranging from 10 to 0.1 picoTesla at low frequency (Table 1-1). Traditional magnetic sensors are limited by their sensitivity around nanoTesla, except for SQUID, however, its low temperature operation needs expensive and cumbersome cryogenics and prevents the portable applications.

Table 1-1. The human brain magnetic-electric signal

<b>Type</b>	<b>Frequency (Hz)</b>	<b>Location</b>	<b>Function</b>
<i>Delta</i>	up to 4	high amplitude waves	Sleep
<i>Theta</i>	4 – 7	not related to task at hand	Idling
<i>Alpha</i>	8 – 12	unsymmetrical distribution high amplitude	relaxed/reflecting closing the eyes
<i>Beta</i>	12 – 30	symmetrical distribution low amplitude waves	alert busy or anxious thinking active concentration
<i>Gamma</i>	30 – 100 +	Somatosensory cortex	Multi-task

In this work, we will develop a chip-scale, ultra-sensitive magnetoelectric sensor system at room temperature. The featured device will take the advantages low cost and low power of bulk magnetoelectric sensors and yield the sensor array fabrication towards biomedical imaging applications. Based on the preliminary results by Zhao Fang and me, we focus on the monolithic integration of magnetoelectric sensors which is compatible with Si microelectronic batch fabrication. A novel structure—a magnetoelectric flexural gate transistor (MEFGT) is presented with the direct capacitance coupling from the top cantilever gate to the extended transistor gate. Device modeling as well as sensitivity and noise analysis will be addressed in details for further understanding of the sensor operation. Noise modeling will be also discussed for future advanced

MEFGT. Besides, front end readout circuit design and on chip post signal processing circuit will be investigated.

Chapter 2 will review the previous results for magnetoelectric laminates bulk sensors demonstrated by Zhao Fang and me. Three different approaches to improve the magnetoelectric coefficient will be discussed. The sensitivity will be compared with the conventional sensors. The chapter will conclude with several limitations of bulk ME sensors which will be addressed in the following chapter.

Chapter 3 will describe properties of magnetostrictive thin film. It starts with the deposition and characterization of the Metglas<sup>®</sup> thin film. An in-situ magnetic domain alignment deposition method will be discussed. Characterization techniques include X-ray Photoelectron Spectroscopy (XPS), hysteresis loop and magnetostrictive coefficient measurements. This follows by optical and capacitance measurement to verify the functionality of the deposited thin film for sensing.

Chapter 4 will present the fabrication process and characterization of thin film magnetic sensors with Metglas<sup>®</sup>/  $\text{Pb}(\text{Zr}_{0.52}\text{Ti}_{0.48})\text{O}_3$  (PZT) laminates and the magnetoelectric flexural gate transistor (MEFGT). Main challenges associated with device fabrication will be fully discussed, including aspect ratio, residue stress and device isolation. Several characterization techniques, both optical and electrical, will illustrate the device performance. Sensitivity and noise density in vacuum (in air) at (off) resonant frequency will be analyzed. In the rest of this chapter, we focus on the MEFGT device noise modeling. Both transistor flicker noise and sensor thermal mechanical/magnetostrictive noise will be discussed. As a conclusion, a SiGE quantum well field effect transistors (QWFETs) with low flicker noise will be introduced and modeled as a candidate to the MEFGT readout transistors..

Chapter 5 will main describe the readout circuit design and simulation. Post stage signal modulation technique to improve the signal-to-noise ratio will be introduced in this chapter. This includes a two stage operational amplifier and an on-chip lock-in amplifier for signal processing.

Chapter 6 will conclude the thesis by summarizing the work in thin film ME sensors and proposing ideas for future work. The stability of single end clamp MEFGT is one of the most importance issues that need to be considered before practical applications, so in plane detection method will be suggested. Additionally, low flicker noise transistors will be adopted in future to reduce the device noise level. Material magnetostrictive properties improvement and on-chip hard magnet bias deposition will be expected to fulfill the entire sensor system integration.

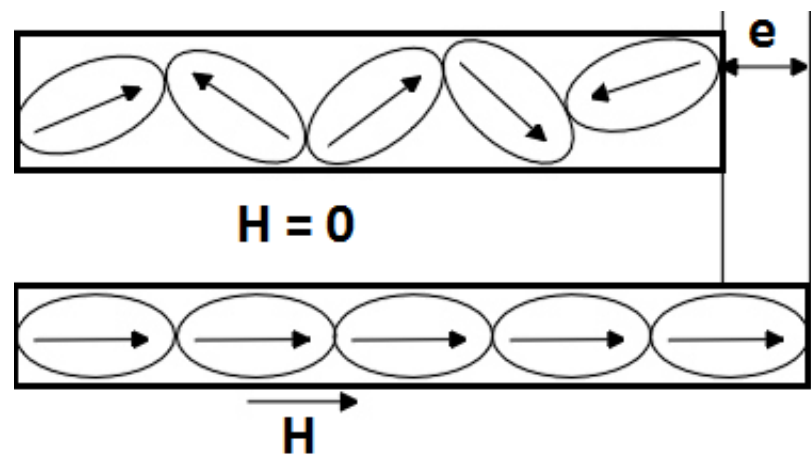
## Chapter 2 Magnetoelectric Laminates Bulk Sensors (Preliminary Results)

Multiferroic materials have the feature of exhibiting ferroelectricity and ferromagnetism simultaneously. Particularly the ME effect, which is the appearance of an electrical signal upon applying a magnetic field  $H$  and/or the appearance of a magnetic signal upon applying an electric field  $E$ , has been studied most because of their scientific interest and application potentials for a broad range of advanced technologies. Although the ME effect was first observed in single phase materials [4], such as antiferromagnetic  $\text{Cr}_2\text{O}_3$  crystals, rare earth ferrites and yttrium iron garnets, their ME responses are either relatively weak or at low temperature for practical application. In contrast, the laminate composites consisting of ferromagnetic phases (e.g. Terfenol-D and Metglas<sup>®</sup>) with magnetostriction (Fig. 2-1 (a)) and ferroelectric phases (e.g.  $\text{Pb}(\text{ZrTi})\text{O}_3$  and Polyvinylidene fluoride (PVDF)) with piezoelectricity (Fig. 2-1 (b)) have shown strong electromagnetic coupling effect between the two phases (Fig. 2-1 (c)) [9-24].

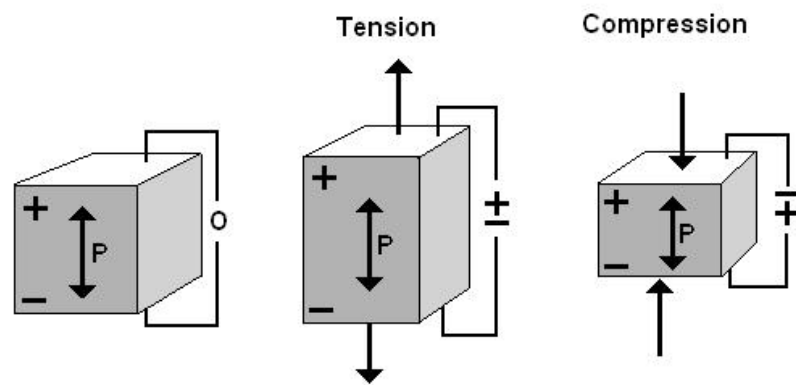
The electromagnetic coupling effect is characterized by the ME coupling coefficient  $\alpha_{ME}$ ,

$$\alpha_{ME} = \frac{\Delta E}{\Delta H} = \frac{\Delta E}{\Delta S} \cdot \frac{\Delta S}{\Delta H}$$

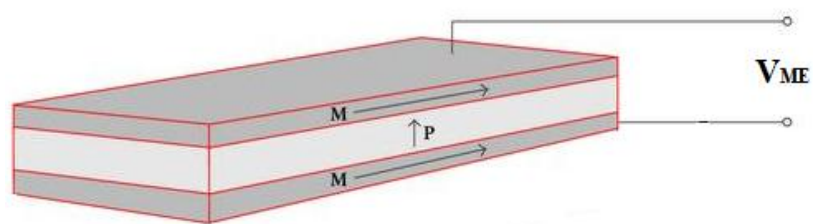
where  $E$  is the induced electric field across the piezoelectric layer,  $S$  is the magnetostrictive strain caused by the application of magnetic field and  $H$  is the external magnetic field. In the past decade, extensive research has been conducted to enhance  $\alpha_{ME}$ . In this chapter, we review three preliminary approaches (by Zhao Fang and me) to improve  $\alpha_{ME}$ : magnetic flux concentration effect, resonance enhancement and single crystal piezoelectric laminates.



(a)



(b)



(c)

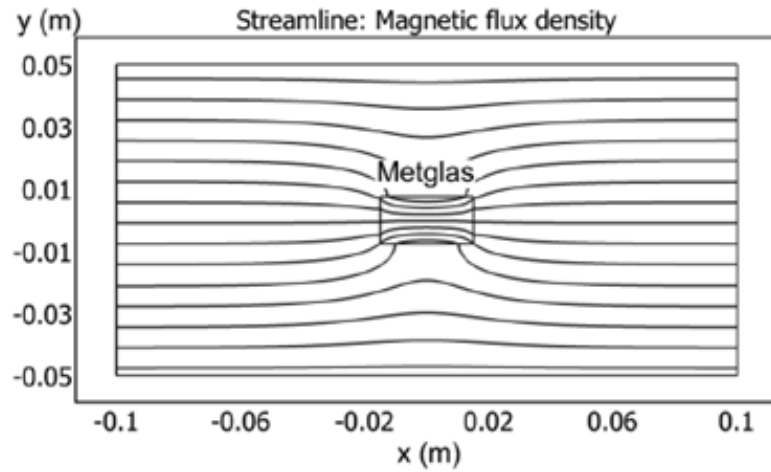
Figure 2-1. Illustration of (a) magnetostriction (b) piezoelectricity (c) magnetoelectricity.

## 2.1 Magnetic Flux Concentration Effect

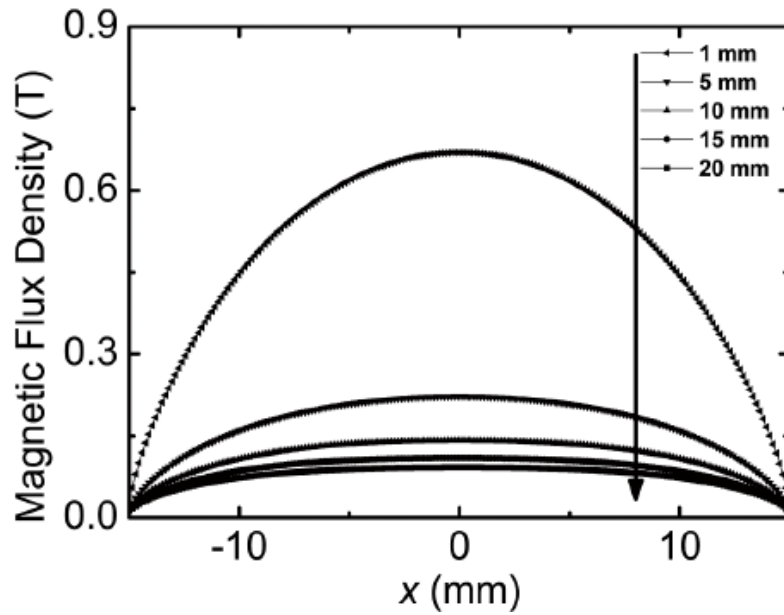
One of the methods which can lead to improvement of sensitivity is utilizing the flux concentration effect [30]. For magnetic materials with very high permeability such as Metglas<sup>®</sup> ( $\mu_r > 45,000$ ), the magnetic flux concentration effect can be quite significant. Illustrated in Fig. 2-2 (a) is a 2-D COMSOL MULTIPHYSICS<sup>®</sup> [25] simulation result of the flux concentration effect for a Metglas sheet with a width (along the y-direction)/length (along the x-direction) ratio of 0.5 in free space. As can be seen, the flux density inside the Metglas<sup>®</sup> is much higher than that in free space. Figure 2-2 (b) shows that for the Metglas sheet with  $W_m=1$  mm,  $B_M$  at  $x=0$  is about 0.7 T, almost 7 times larger than that for  $W_m=20$  mm.

The ME coefficient  $\alpha_{ME}$  is presented in Metglas<sup>®</sup> 2605SA1 (30 mm×15 mm×25  $\mu\text{m}$ ) /PVDF (10 mm×1 mm×25  $\mu\text{m}$ ) composite laminates. When the piezoelectric layer is bonded to different sites of a Metglas<sup>®</sup> sheet, the variation of magnetic flux in Metglas sheet can cause the variation of the ME voltage coefficient, shown in Fig. 2-3 (a). The measured  $\alpha_{ME}$  is the largest where PVDF placed at the center of a Metglas<sup>®</sup> sheet (the inset of Fig. 2-3 (a)). Figure 2-3 (b) presents the experimental results of ME for the Metglas/PVDF laminates with varying  $W_m$  from 20 mm to 1 mm. As can be seen ME increases with decreasing  $W_m$ , while peaking at a lower dc bias field.

Comparing the experimental results in Fig. 2-3 with the simulation results of Fig. 2-2 reveals that although there is an increase of ME with decreased aspect ratio of the Metglas<sup>®</sup> sheet, the experimental increase is much smaller than that of the simulation. This is mainly caused by the bonding epoxy which becomes an extra load for Metglas<sup>®</sup> and reduces the coupling effect.

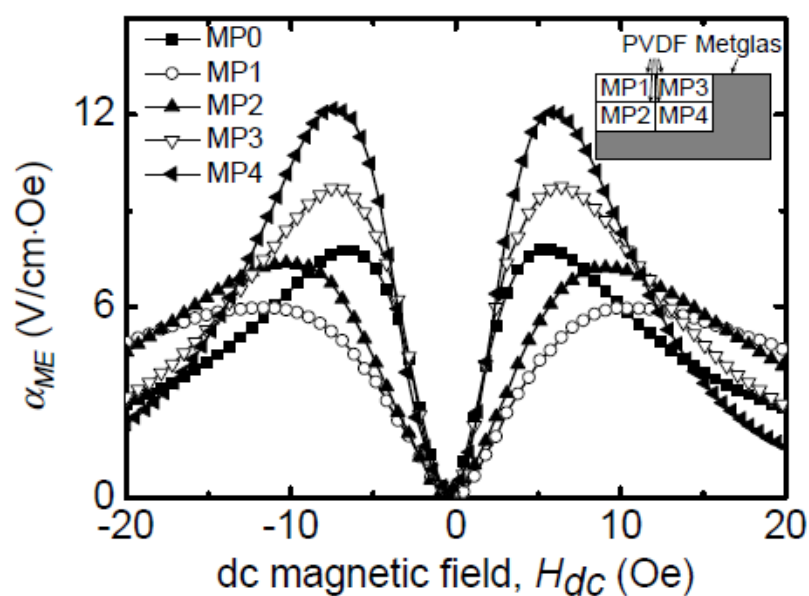


(a)

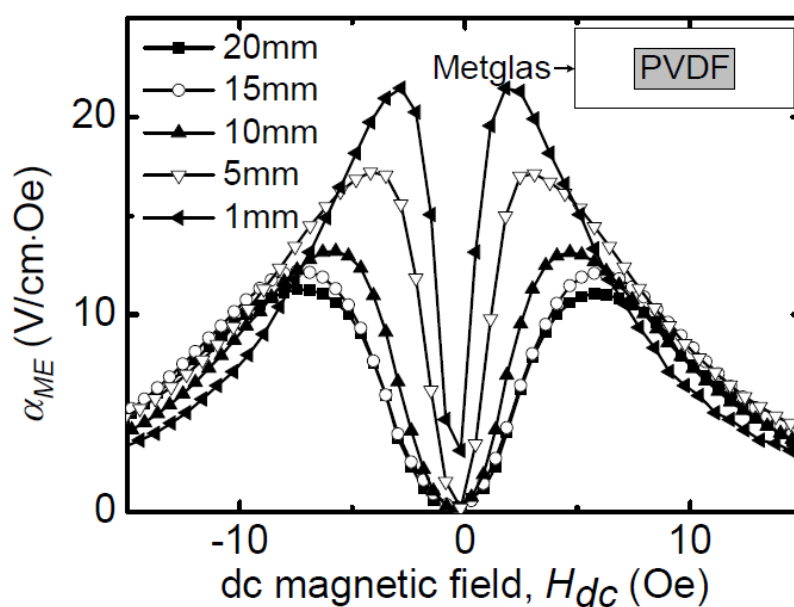


(b)

Figure 2-2. (a) Magnetic flux density distribution in Metglas<sup>®</sup> under a uniform external magnetic field in free space; (b) Magnetic flux density of the Metglas<sup>®</sup> sheet along the x-axis (length direction) at  $y=0$ ,  $z=0$  (The origin is at the center of Metglas<sup>®</sup> sheet) with various aspect ratios of  $W_m/L_m$ . (The length and thickness are fixed at 30 mm and 25  $\mu\text{m}$  respectively, and the width  $W_m$  is varied from 20mm to 1 mm). The external magnetic field is 1 Oe ( $10^{-4}$  T) [30].



(a)

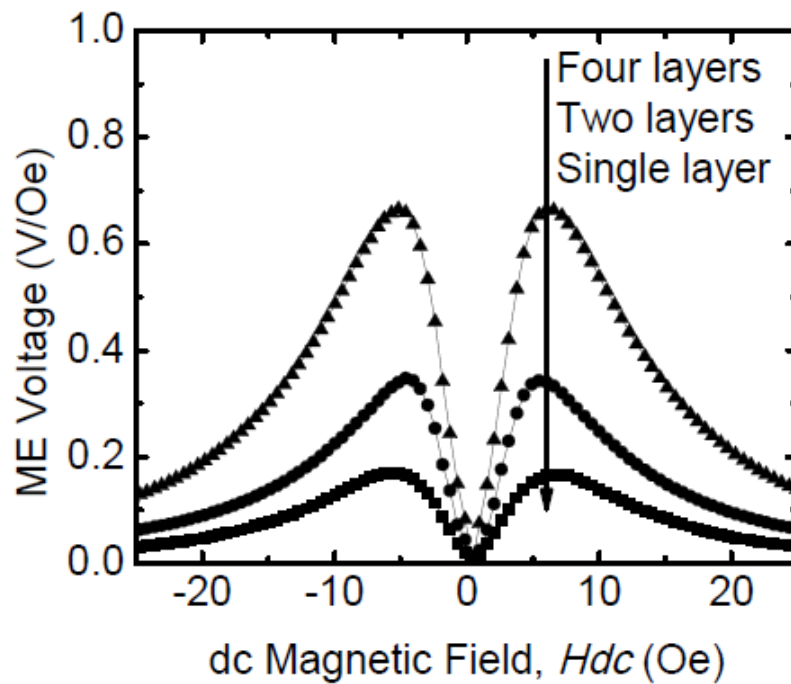


(b)

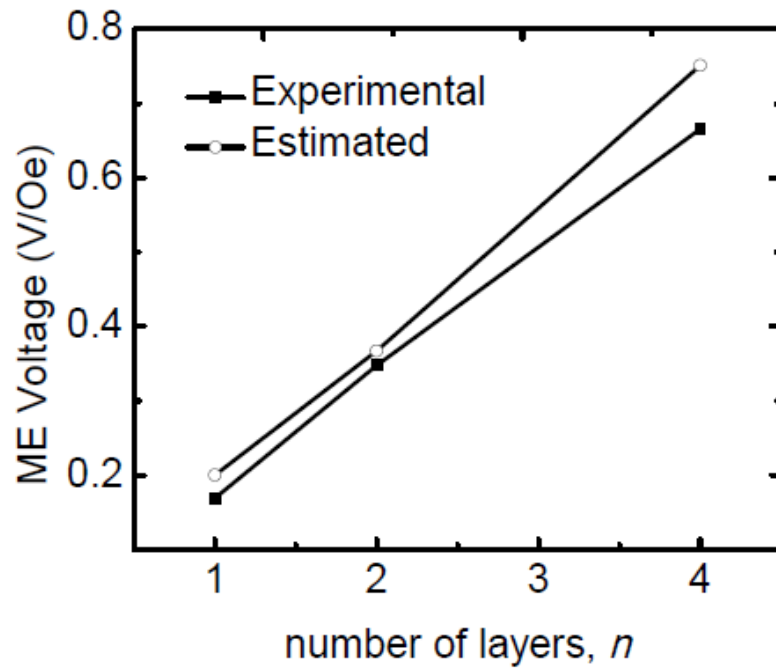
Figure 2-3. (a)  $\alpha_{ME}$  as a function of dc bias magnetic field for Metglas<sup>®</sup>/PVDF laminates with PVDF bonded on different regions of Metglas<sup>®</sup> sheet. (b)  $\alpha_{ME}$  as a function of dc bias magnetic field for Metglas<sup>®</sup>/PVDF laminates with varying  $W_m$ . The data was measured at 20 Hz and  $H_{ac}=0.38$  Oe [30].

## 2.2 Multilayer Structure

The output ME voltage is proportional to the induced polarization charge in the piezoelectric materials, so by increasing the effective piezoelectric capacitance, for example, increasing the effective area or reduce the effective thickness of the piezo layer will improve the sensitivity of the ME laminate sensors [78]. Indeed, as shown in Fig. 2-4 (a), increasing the piezo polymer PVDF layer numbers in the ME laminate composites from one to four yields a four times increase in the sensitivity of the integrated magnetic sensor. Figure 2-4 (b) presents a comparison of the results from the analytical estimation using the magnetostrictive coefficient of Metglas<sup>®</sup> reported and the properties of PVDF piezoelectric films with the experiment data of Fig. 2-4 (a) [24], which shows a good agreement.



(a)



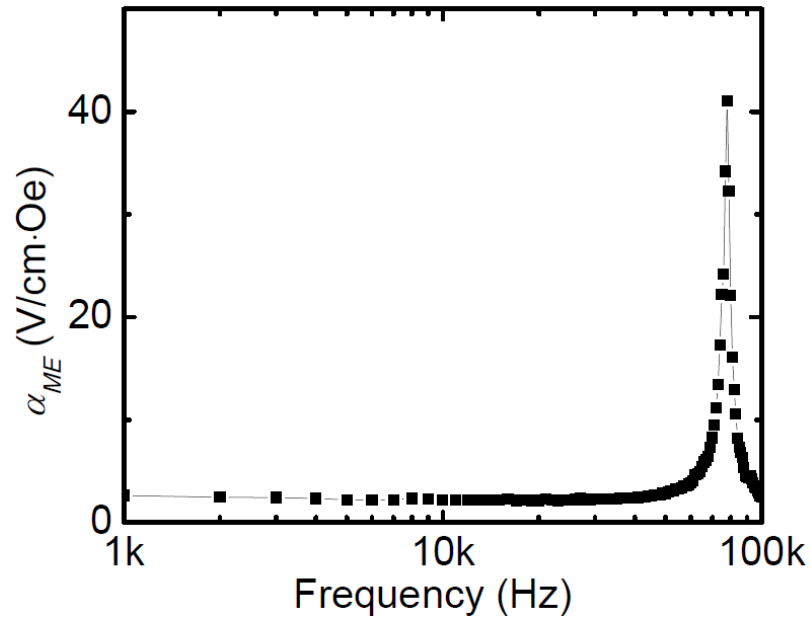
(b)

Figure 2-4 (a) ME voltage of the sensor system as a function of dc bias magnetic field for Metglas<sup>®</sup>/PVDF laminates with different number of PVDF layers. The data were measured at 200 Hz and ac magnetic field  $H_{ac}=0.08$  Oe. (b) Comparison of experimentally measured ME voltage with analytical estimation [78].

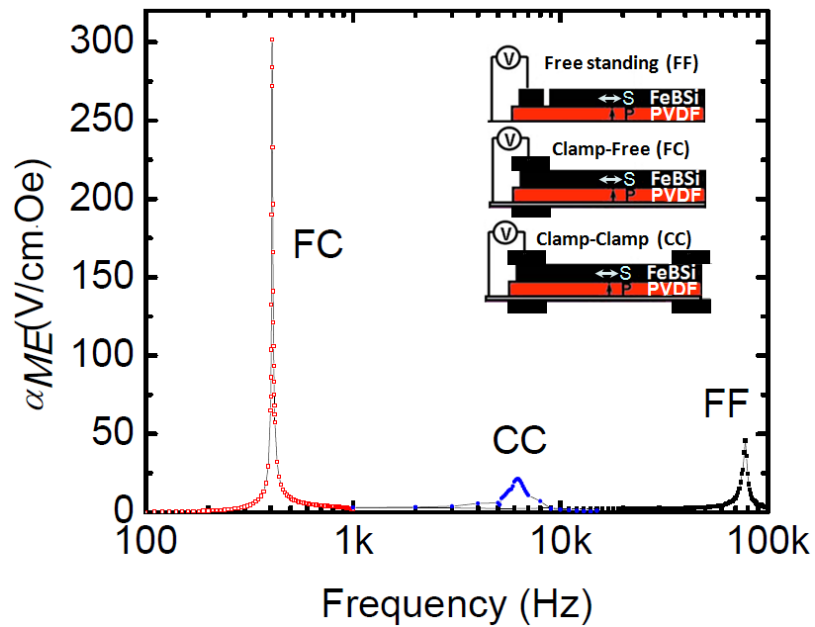
### 2.3 Resonance Enhancement

In physics, resonance is the tendency of a system to oscillate at greater amplitude at some frequencies than at others. These are known as the system resonant frequencies at which small periodic driving forces can produce large amplitude oscillations, because the system stores vibration energy. The studies on the ME resonance response have shown that  $V_{out}/H_a$  can be increased significantly at resonant frequencies. [26-28]. The laminate composites can accumulate much more energy internally at resonant frequencies than at other frequencies, consequently strain response produced by weak magnetic signal can be enhanced by accumulating over many periods at resonant frequencies. The laminate composites we use are Metglas<sup>®</sup> layer 10 mm×1 mm×25 μm and PZT layer 5mm×1 mm×100 μm. Figure 2-5 (a) shows frequency response of a Metglas<sup>®</sup>/PZT laminate sensor in free-free (F-F) mode.

In a practical applications, a stable structure is needed in order to get a reliable ME response. The two commonly used modes are Free-Clamped (F-C) and Clamped-Clamped (C-C) mode, in which the transverse wave propagation and consequently bending resonance is dominant. The comparison of ME coefficient as a function of frequency is shown in Fig. 2-5 (b) for Metglas<sup>®</sup>/PZT laminate composites in freestanding (FF), FC, and CC modes. It's found that FC mode has the largest ME at the resonant frequency.



(a)

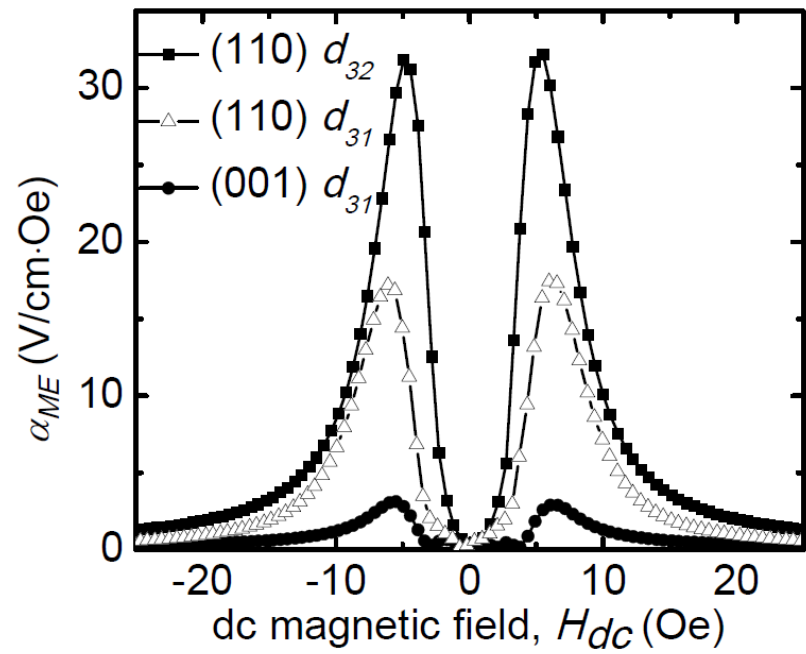


(b)

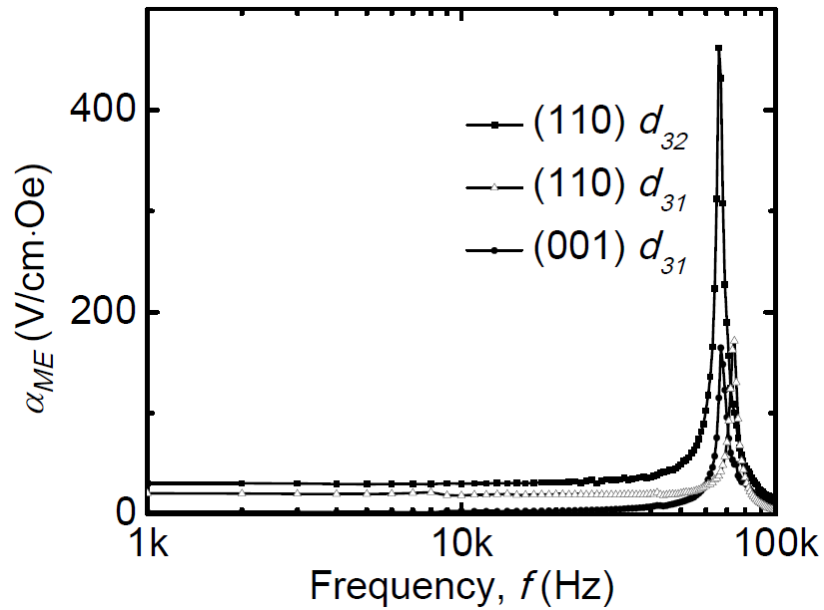
Figure 2-5. (a)  $\alpha_{ME}$  coefficient as a function of frequency for a ME laminate sensor with Metglas<sup>®</sup>/PZT, showing an enhanced sensitivity at the resonance, 78 kHz. (b)  $\alpha_{ME}$  as a function of frequency for Metglas<sup>®</sup>/PZT laminate composites in FF, FC, and CC modes. The Metglas<sup>®</sup> layer is 10 mm×1 mm×25  $\mu$ m and PZT layer is 5mm×1 mm×100  $\mu$ m (Inset: Schematic for different structures.).

## 2.4 Single Crystal Piezoelectric Laminates

The output polarization charge of ME laminates sensors are determined by the elastic, piezoelectric, and dielectric features of the piezoelectric layers. As the piezoelectric layers, relaxer based piezoelectric single crystals (e.g. PMN-PT ( $\text{Pb}(\text{Mg}_{1/3}\text{Nb}_{2/3})\text{O}_3\text{-PbTiO}_3$ )) show a remarkable improvement in magnetoelectric coefficient  $\alpha_{ME}$  compared to PVDF and PZT due to exceptional piezoelectric coefficients  $d_{31}$  and low dielectric losses. Here PMN-PT is used as the piezoelectric layer to improve the  $\alpha_{ME}$  and consequently enhance the sensitivity of the ME sensors. As shown in Fig. 2-6 (a), (110)  $d_{32}$  sample has the largest ME coefficient due to the highest piezoelectric coefficient. Figure 2-6 (b) shows the ME coefficient frequency response of the ME samples with different cut orientation and cut direction of single crystal PMN-PT. (110)  $d_{32}$  sample has the highest peak value (461.6 V/cm Oe) at resonance frequency.



(a)



(b)

Figure 2-6. (a)  $\alpha_{ME}$  as a function of dc bias magnetic field for Metglas<sup>®</sup>/PMN-PT laminates with different cut orientation and cut direction of single crystal PMN-PT. The data were measured at 20 Hz and  $H_{ac}=0.8$  Oe. (b)  $\alpha_{ME}$  as a function of frequency for Metglas<sup>®</sup>/PMN-PT laminates with different cut orientation and cut direction of single crystal PMN-PT.

### Chapter 3 Magnetostrictive Thin Films

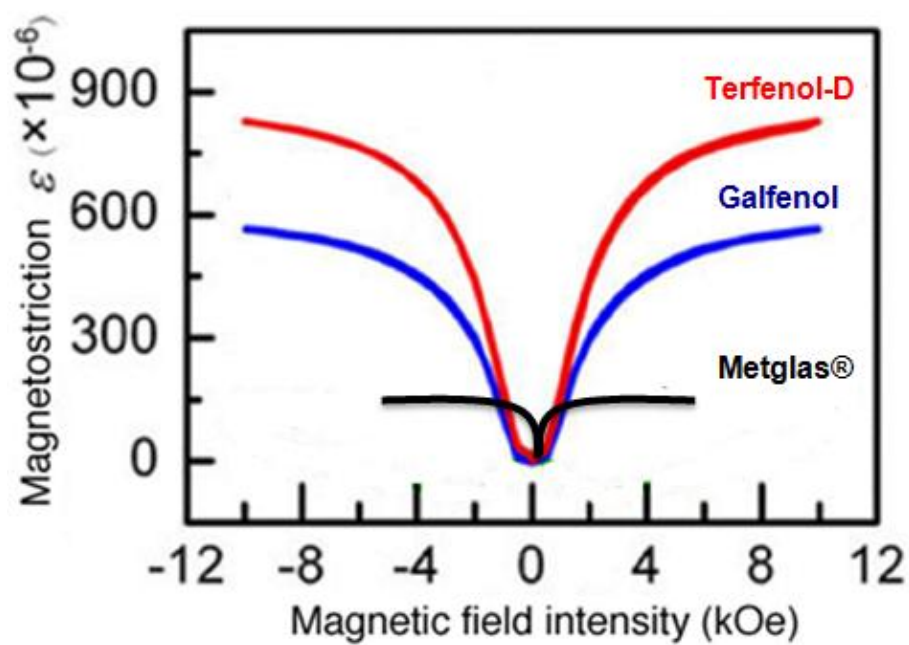
The operation principle of bulk ME laminates sensors and several sensitivity enhancement methods have been discussed. Such bulk sensors made by ME laminates were reported to exhibit large ME coupling coefficient of 21.46 V/cm•Oe and a resolution of  $2 \times 10^{-11}$  T/ $\sqrt{\text{Hz}}$  [29, 30]. Yet, considering the applications of magnetic field sensing, these bulk sensors suffer from several problems. First, the size of the current prototypes, ranging from 2 cm to more than 10 cm, is too large for sensing/imaging applications and cannot be integrated monolithically with CMOS based signal processing circuit on a silicon substrate for realization of smart sensor systems. Second, the coupling of the magnetic field induced strain to the piezoelectric layer is reduced by the bonding epoxy layer. The epoxy layer not only increases the mechanical loading of the magnetostrictive layer, but also perturbs the magnetic domain structure that was previously optimized by annealing [30-32]. To overcome these shortcomings, it is desirable to reduce the sensor size into the micro-scale size range and integrate magnetostrictive materials directly to the piezoelectric layer. Thus, an integrated magnetoelectric laminates sensor meets the urgent requirements. Thin films magnetostrictive/piezoelectric material deposition by MEMS and standard semiconductor fabrication processes becomes critical factors in the sensor's performance. In this chapter, the deposition and characterization of the Metglas<sup>®</sup> thin film are investigated and analyzed.

### 3.1 Magnetostrictive Materials

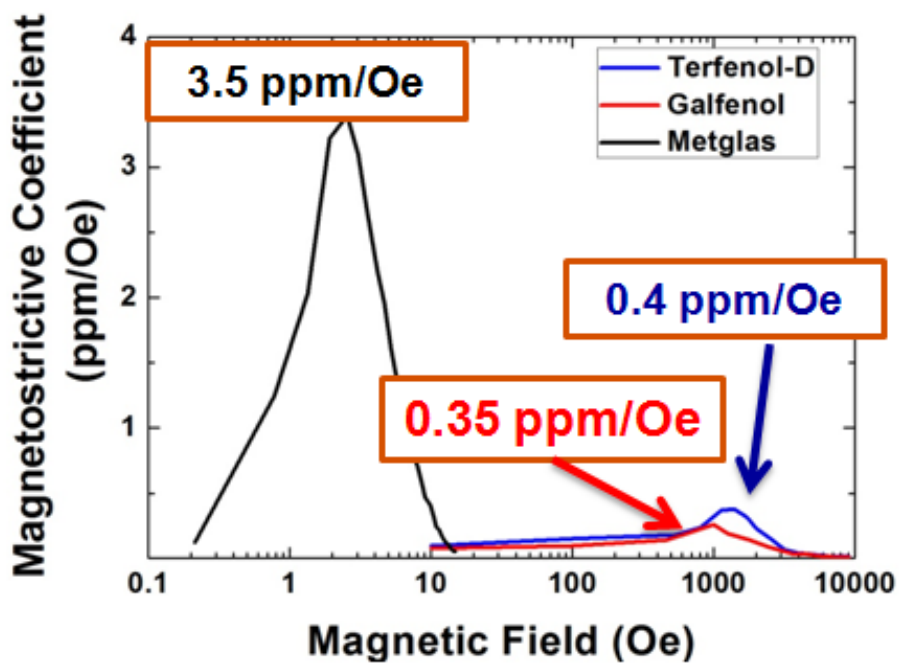
Most commonly used and studied magnetostrictive materials are Terfenol-D [16, 81], Galfenol [82] and Metglas<sup>®</sup>. Terfenol-D exhibits the highest magnetostriction (> 800 ppm) and the largest saturation field (~ 4 KOe) among all the materials, as shown in Fig. 3-1 (a). Galfenol shows lower magnetostriction compared to Terfenol-D, however, it has a much higher permittivity. Metglas<sup>®</sup> shows the lowest magnetostriction (~ 30ppm), the smallest saturation field (20 ~ 100 Oe) and the highest permeability ( $\mu_r > 45,000$ ).

For the AC magnetic field detection, we should consider the magnetostrictive coefficient, which is the slope of the curves in Fig. 3-1 (a). As we can see in Fig. 3-1 (b), the MS coefficient of Metglas<sup>®</sup> is the highest among all three materials and it requires very low DC bias magnetic field, so we choose Metglas<sup>®</sup> as the magnetic field sensing material in this project. Particularly, Metglas<sup>®</sup>2605SA1 ( $\text{Fe}_{85}\text{Si}_{10}\text{B}_5$ ) has been chosen for the current study because of its superior magnetic properties and relatively simple chemical composition among the Metglas<sup>®</sup> family.

To achieve a device quality Metglas<sup>®</sup> thin film, three requirements have to be satisfied: the right alloy composition, the correct microstructure, and fully aligned magnetic domains in the desired direction. Besides the thin film technology has to be incorporated with the IC process, to make possible the integration of the sensor.



(a)



(b)

Figure 3-1. (a) Magnetostriction and (b) Magnetostrictive coefficient as a function of magnetic field for Terfenol-D (red), Galfenol (blue) and Metglas<sup>®</sup> (black).

### 3.2 Deposition System and Conditions

We use sputtering as the deposition method because of its ease of composition control. The major advantage of sputtering over other deposition techniques is that it can transfer the stoichiometry of an alloy target to the substrate as long as the target is made of non-volatile elements, and no direct high energy particle bombardment (or reverse sputtering) occurs at the substrate. Hence the alloy composition of the thin film can be controlled simply by choosing the right composition for the target.

Traditional DC magnetron sputtering system is not a good choice for Metglas<sup>®</sup> sputtering because of the high permeability of the target. The target may shunt the magnetic field of the system magnet and result in a low plasma density. The target has to be thin enough so that stable plasma density could be generated within the chamber to achieve a constant sputtering rate. In this project, we find the critical thickness for the commercial Metglas<sup>®</sup> target by trial and error, however, the target is worn-out in a very short time. Finally, we stop using this inefficient method and come up with a better sputtering system for Metglas<sup>®</sup>.

The sputtering system was developed by upgrading an Ion Milling etching tool as shown in Fig. 3-2. The vacuum is provided by a standard mechanical rough pump and a base pressure of  $10^{-6}$  Torr is achieved with the help of a cryo pump. The alloy composition of the film is accomplished by DC ion milling sputtering. The ion gun will shoot directly on the Metglas<sup>®</sup> target which is 60 degree oriented from level and the reflect particles will directly deposit on the substrate holder. The substrate holder is designed with rotation to improve the uniformity of the deposited film.

Targets were built by pasting 25  $\mu\text{m}$  Metglas<sup>®</sup>2605SA1 sheets to the six inch target bond with vacuum epoxy. Each target can be used for 2 hours and a half before the middle part of the target burn through. Table 3-1 summarizes the deposition parameters.

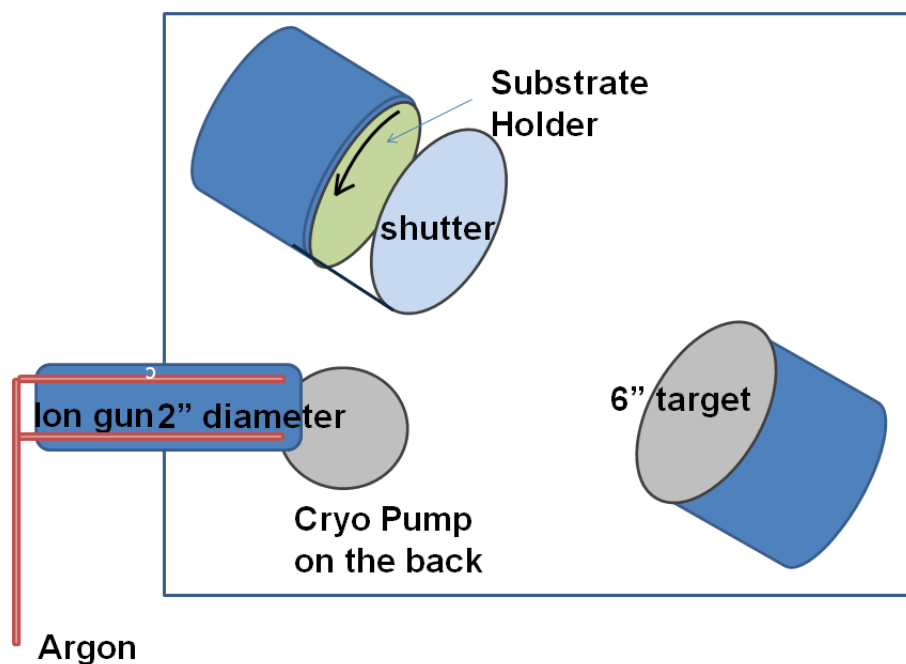


Figure 3-2. Ion Mill Sputtering System Schematic.

Table 3-1. Ion Mill Sputtering Conditions.

Current (mA)	30
Voltage (V)	1500
Power (W)	45
Pressure (mTorr)	0.5
Temperature (K)	300~350
Deposition Rate (nm/hr)	100

In-situ magnetization as the film is being formed is the key to the success of the aligned thin film domain structure. Post field annealing on the Metglas<sup>®</sup> thin film is found to be not as effective as its ribbon counterpart. This may be attributed to the difference in thermal expansion coefficients

between the film and the substrate. Stress at the film-substrate interface will build up upon heating and cooling, pulling the magnetic domains away from the direction of magnetization field. In-situ domain alignment is accomplished by placing a permanent magnet near the substrate to magnetize the thin film as the deposition process proceeds (Fig. 3-3).

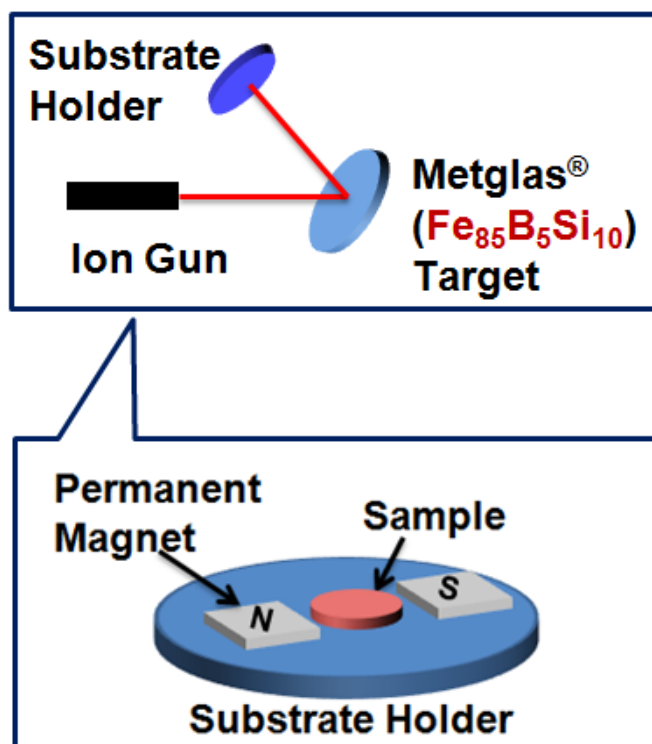


Figure 3-3. Schematic of In-situ magnetization Ion Mill Sputtering system.

### 3.3 Magnetic Characterization

The only possible volatile element is Boron. To ensure the thin film has the right stoichiometry, X-ray Photoelectron Spectroscopy (XPS) analysis (Fig. 3-4) has been performed, which confirmed that there is no deficiency in boron in our thin film samples. The data were measured at 100 nm depth of the sample films instead of at the film surface since the sample is oxidized as soon as it exposes to the air. Table 3-2 summarizes all the elements concentration percentage from the sample films. The unexpected Indium and Oxygen elements come from the residues of the bonding epoxy when the pasting the Metglas<sup>®</sup> sheet to the substrate holder.

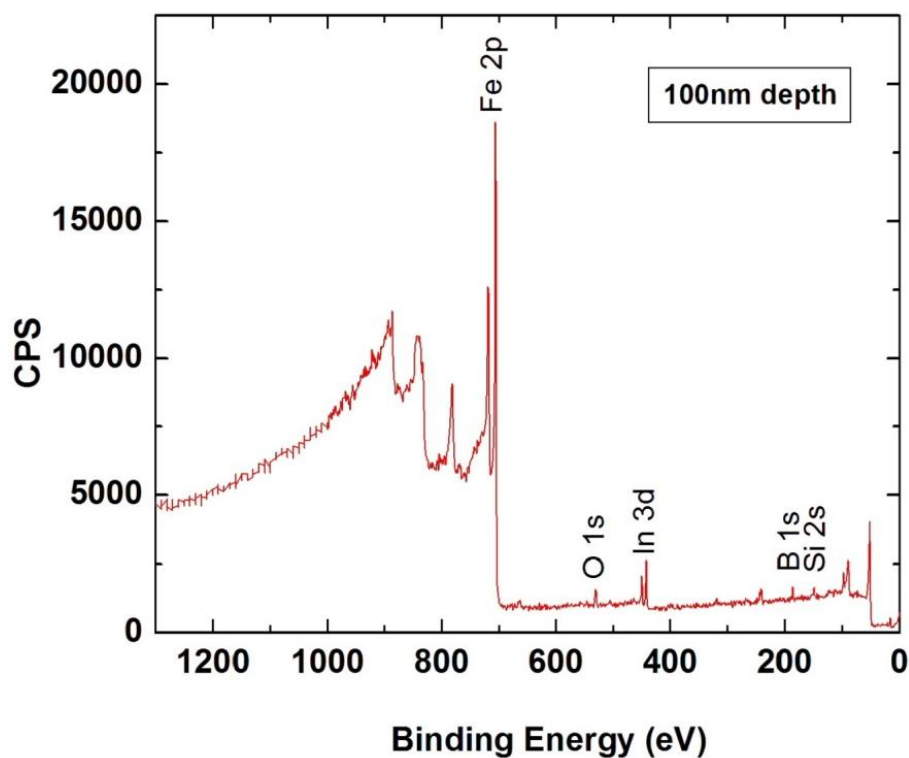


Figure 3-4. XPS results at 100nm depth of Metglas films.

Table 3-2. XPS Atom Composition.

Elements	%Concentration
Fe (2p)	85.0234
O (1s)	3.2268
In (3d)	0.6647
Si (2s)	9.3278
B (1s)	4.7573

To verify if the domains of the thin film have been successfully aligned during the sputtering process, a magnetization measurement has been performed on the as-deposited samples. The magnetic properties measurement system [Quantum Design Inc. MPMS System] was used for the thin film hysteresis loop measurement. The largest magnetization change was found when the pre-magnetized axis of the sample was coincident with the measurement field direction. The typical coercivity ( $H_c$ ) of the samples is around 6 Oe (Fig. 3-5). The films also show a high magnetization ~2 Tesla

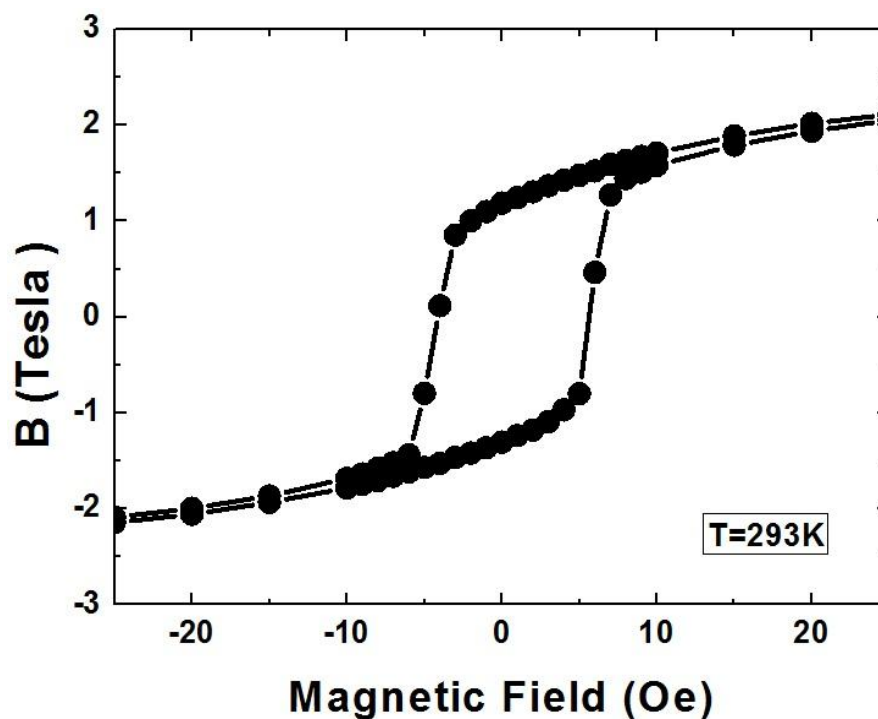


Figure 3-5. Hysteresis B-H loop measured by SQUID system.

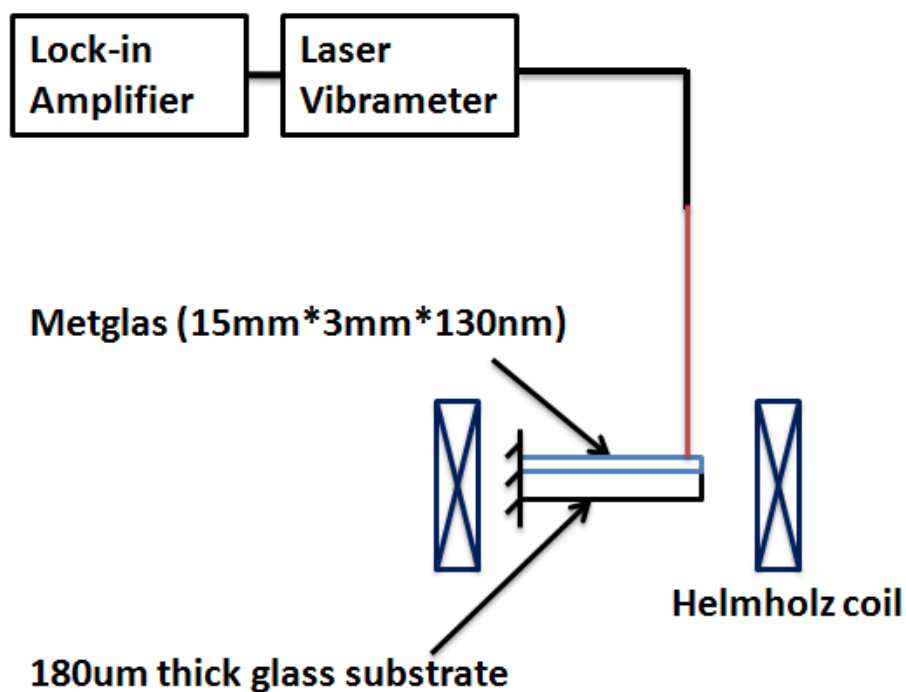
Once the easy axis is indentified, the magnetostrictive coefficient of the samples is characterized in the setup shown in Fig. 3-6 (a). The sample with 180  $\mu\text{m}$  glass substrate and 0.13  $\mu\text{m}$  thin film Metglas<sup>®</sup> is cut into 15 mm  $\times$  3 mm strips and clamped one end to form a cantilever structure. The custom made Helmholtz coil provides the input ac magnetic field and the dc field is generated by an external magnet. The deflection of the cantilever is captured by the laser vibrometer and read out by the lock-in amplifier.

The deflection of the beam can be calculated by the following equation [34, 35]:

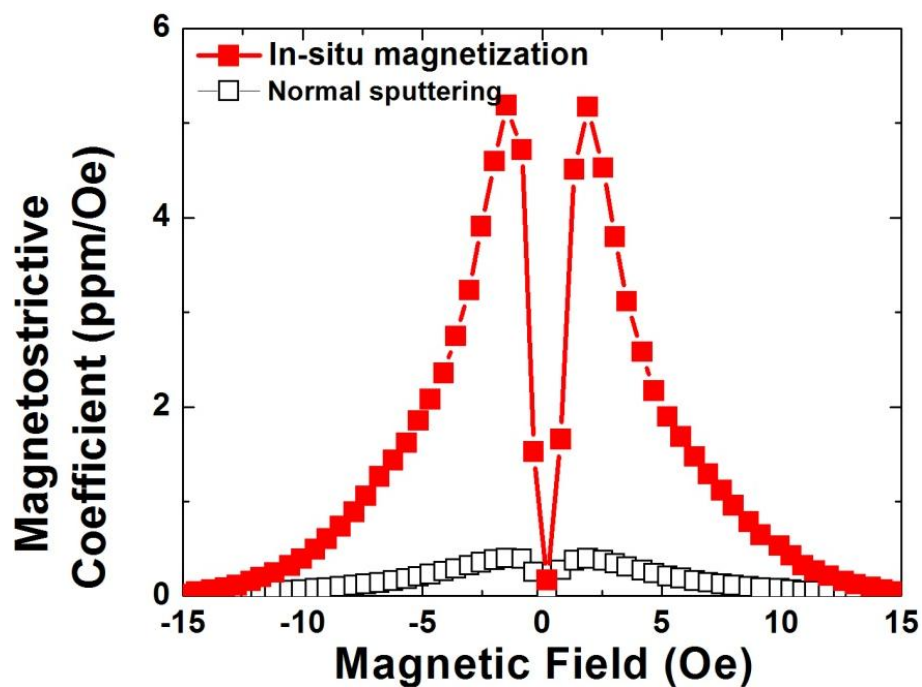
$$\Delta\delta = \frac{3l^2}{t_a} \frac{AB(B+1)}{D} d_{31}^m \Delta H$$

where  $A = E_p / E_a$ ,  $B = t_p / t_a$ ,  $D = A^2 B^4 + 2A(2B + 3B^2 + 2B^3) + 1$ . Here,  $E_p$  and  $E_a$  are the elastic constant,  $t_s$  and  $t_m$  are the thickness of the passive layer (glass) and the active layer (Metglas<sup>®</sup>) respectively,  $\Delta\delta$  is the cantilever deflection,  $\Delta H$  is the input ac magnetic field, and  $d_{31}^m$  is the magnetostrictive coefficient. The measured magnetostrictive coefficient against DC magnetic field is shown in Fig. 3-4 (b). Comparing to the normal radio frequency magnetron enhanced sputtering method, the in-situ magnetization ion mill sputtering shows a significant improvement. The highest magnetostrictive coefficient around 3.5 ppm/Oe has achieved, which is comparable to that of bulk Metglas<sup>®</sup> materials. Also, both parallel and perpendicular field has been applied to sample and the result shows the strong directional dependent to the magnetic field (Fig. 3-4 (c)). The maximum magnetostrictive coefficient in the perpendicular direction (i.e. applied magnetic field is orthogonal to the magnetization (poling) direction of the Metglas<sup>®</sup> film) is  $\sim 7$  times smaller than in the parallel direction and therefore provides a clear directional (vector)

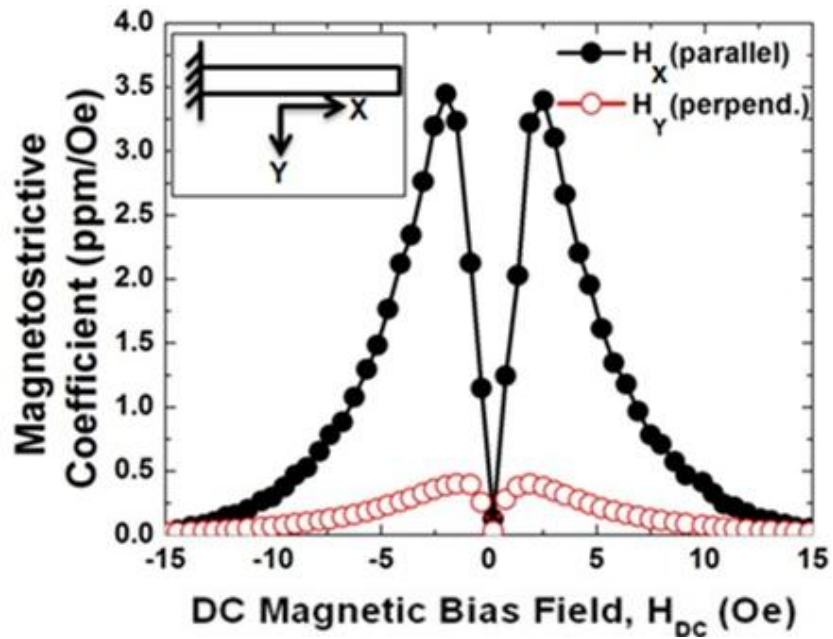
sensitivity to the applied magnetic field. This indicates that Metglas<sup>®</sup> is a potential material for the vector magnetic field sensing applications.



(a)



(b)



(c)

Figure 3-6. (a) Magnetostrictive coefficient measurement setup. (b) Magnetostrictive coefficient comparison between normal sputtering and In-situ magnetization process. (c) Magnetostrictive coefficient of Metglas® thin films as a function of DC bias magnetic field (black dot: parallel field; red circle: perpendicular field).

## Chapter 4 Thin Film Magnetolectric Sensors

### 4.1 Thin Film Magnetolectric Laminate Cantilever Sensors

#### 4.1.1 Fabrication Process

Based on the high performance of thin film Metglas<sup>®</sup>, the monolithic nanofabrication of  $\text{Pb}(\text{Zr}_{0.52}\text{Ti}_{0.48})\text{O}_3$  (PZT)-Metglas<sup>®</sup> ME laminate cantilevers on silicon substrate is presented, as shown in Fig. 4-1.

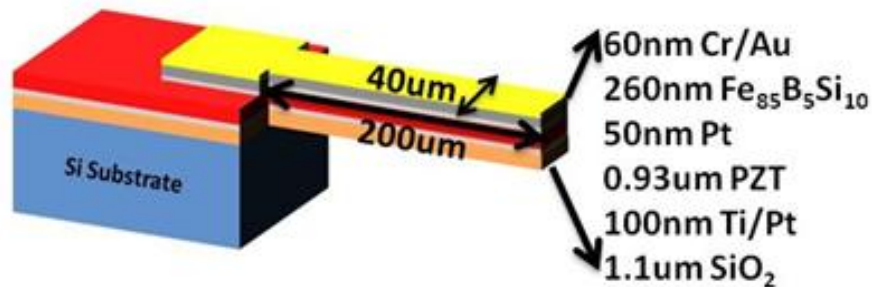


Figure 4-1. Schematic of ME laminate cantilever sensor.

The process flow is outlined in this section and depicted in Fig. 4-2. Fabrication begins with 100 nm Pt sputter deposition (sputtered at 5 mTorr, 200W dc) as the bottom electrode on a SOI substrate. Lead-based piezoelectric thin films have been successfully prepared by sol-gel processing [37-39]. The PZT solution was deposited on the Pt coated SOI substrate by spin-coating at 1500 rpm for 30 seconds. After deposition, each layer was subjected to a two-stage pyrolysis sequence to drive out solvent and decompose organic compounds. This sequence consisted of a 60-second heat treatment at 300 °C followed by one at 450 °C (60 seconds). The

amorphous layer then was crystallized to phasepure perovskite at 700 °C for 60 seconds using the RTA. Each layer was about 0.2- $\mu\text{m}$  thick. A 0.93  $\mu\text{m}$  thick PZT films were fabricated by repeating this procedure to achieve the desired thickness. This follows by 50nm Pt adhesion layer, 260 nm Metglas<sup>®</sup> and a 60 nm Cr/Au (sputtered at 2.5mTorr, 200W dc) top electrode deposition to prevent Metglas<sup>®</sup> thin film from oxidation. The 15  $\mu\text{m}$  thick photo resist SPR220 (spin 3000 rpm for 45 s, bake at 95 °C, 115 °C and 95 °C for 90 s separately, multi-exposure 5 times at 8 mW/cm<sup>2</sup> for 10 s and 10 s wait in between, 30 min wait before develop in CD26 for 2 mins) was chosen to pattern 200  $\mu\text{m}$  x 200  $\mu\text{m}$  bottom contact pad because of the slow etch rate in PZT dry etch. The oxide etcher, Tegal 6500, etched through the PZT layer and accesses the bottom electrodes. A 75 nm/min etch rate has been achieved by using CF<sub>4</sub> (28 sccm)/Ar (7 sccm)/Cl<sub>2</sub> (45 sccm) at 615 W RF power. The etching was performed with consecutive steps 30 s long alternated with 60 s in Ar atmosphere to allow the wafer to cool down. This method was adopted to preserve the stability of the photo resist. The cantilever beam arrays (200  $\mu\text{m}$  x 40  $\mu\text{m}$ ) were then patterned by the second mask and etched down to the Si substrate. Finally, XeF<sub>2</sub> based dry etch (3 Torr, 40 cycles, 0.6  $\mu\text{m}$ /cycle) was used to release the cantilevers [40]. More process details can be find in Appendix A. Figure 4-3 shows the SEM image for the ME cantilevers after releasing. The beam bends up about 50  $\mu\text{m}$  due to the residue stress between different films. This will result in a significant affection in the ME coefficient discussed in the following section.

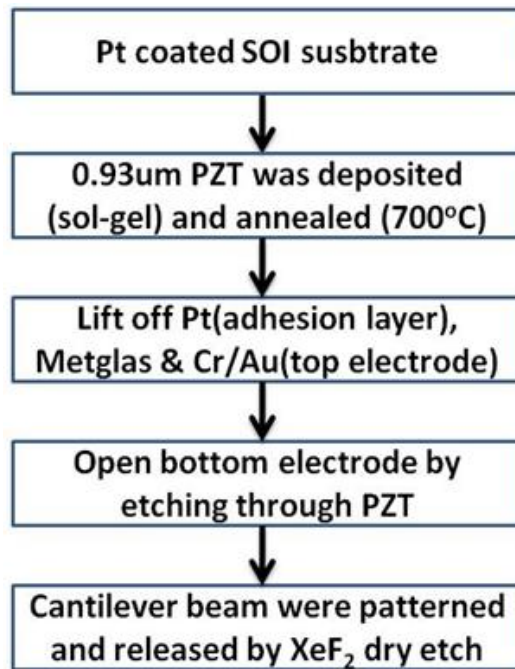


Figure 4-2. ME cantilever process flow.

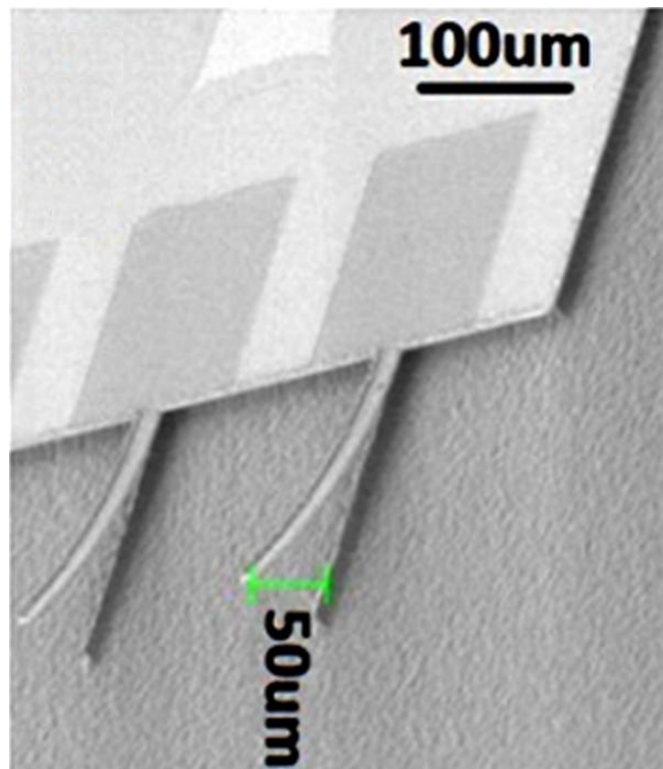


Figure 4-3. SEM image for the released ME cantilevers.

## 4.1.2 Sensor Performance

### 4.1.2.1 ME Coefficient Characterization

The thin film materials characterization is given by Fig 3-6 (b), Metglas<sup>®</sup> magnetostrictive coefficient (0.36 ppm/Oe without in-situ magnetization), and Fig. 4-4, PZT piezoelectric coefficient (7 C/m<sup>2</sup>) [41]. A dual in-line package was used for the sensor electrical connections made via conventional wire bonding and the output of the devices was carried out by a commercial charge amplifier. Figure 4-5 shows the ME cantilever output voltage as a function of DC bias magnetic field. The result exhibits an asymmetric property which is mainly caused by the beam bending, since the residue stress disturbs the magnetic domain alignment in the Metglas<sup>®</sup> thin film. The ME coefficient is then extracted and compared to the theoretical value calculated directly from the magnetostrictive coefficient and piezoelectric coefficient (Fig. 4-6). The difference between experimental and theoretical result arises from two main reasons. First, the Metglas<sup>®</sup> thin film is not only driving PZT layer, but the passive layers SiO<sub>2</sub> and Pt as well. These passive layers serve as a good substrate for PZT growth to maintain the high piezoelectric property. Secondly, the variation in aspect ratio between the cantilever sensors triggers the flux concentration effect difference.

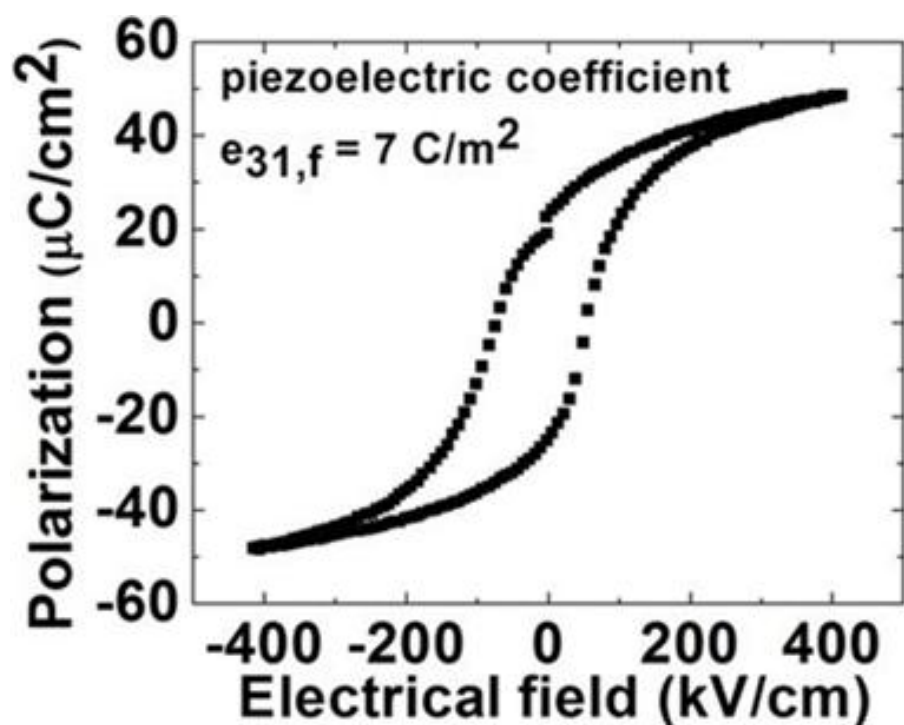


Figure 4-4. SEM image for the released ME cantilevers.

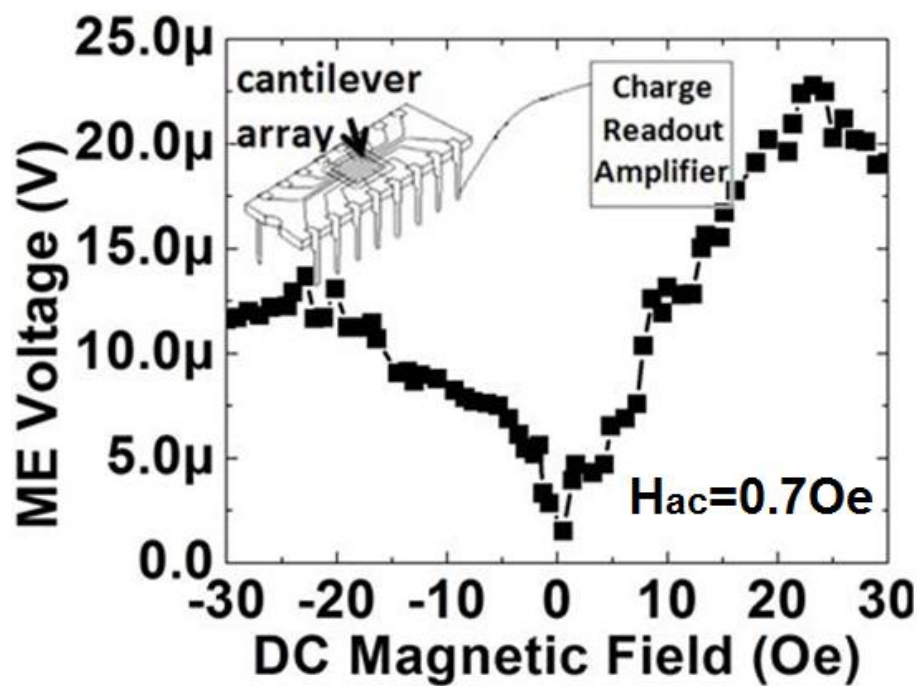


Figure 4-5. ME output voltage as a function of dc bias Magnetic field (The inset shows the measurement schematic). The data were measured at 20 Hz and  $H_{ac} = 0.7 \text{ Oe}$ .

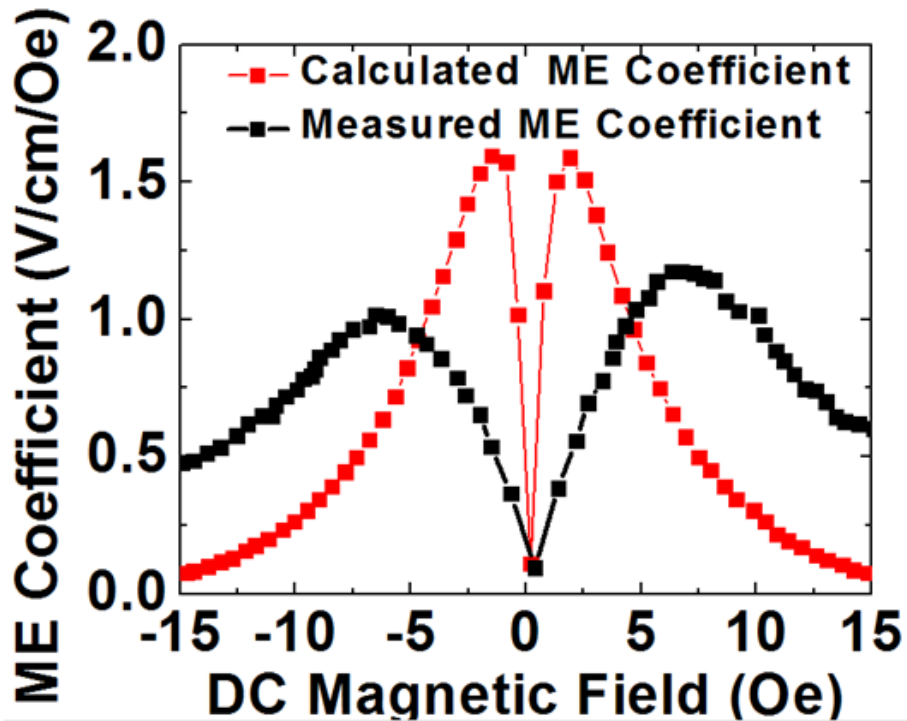


Figure 4-6. ME coefficient as a function of dc bias magnetic field: measurement versus calculation results.

The frequency response of ME cantilever sensor is also characterized in Fig. 4-7. The mechanical resonance in air happens at 8.4 KHz which boosts the ME coefficient (1.8 V/cm Oe) by the quality factor. The mechanical resonant improves the ME coefficient by about 5 times. The resonance frequency is in good agreement with the following equation [42]:

$$f = \frac{1}{4\pi} \frac{\lambda_1^2}{L^2} \sqrt{\frac{\hat{E}t^3}{3\rho t}}$$

where  $\lambda_1 = 1.8751$  for the first resonance mode,  $E$  is the effective Young's modulus,  $L$  and  $t$  are the length and thickness of the cantilever,  $\rho$  is the density of the material.

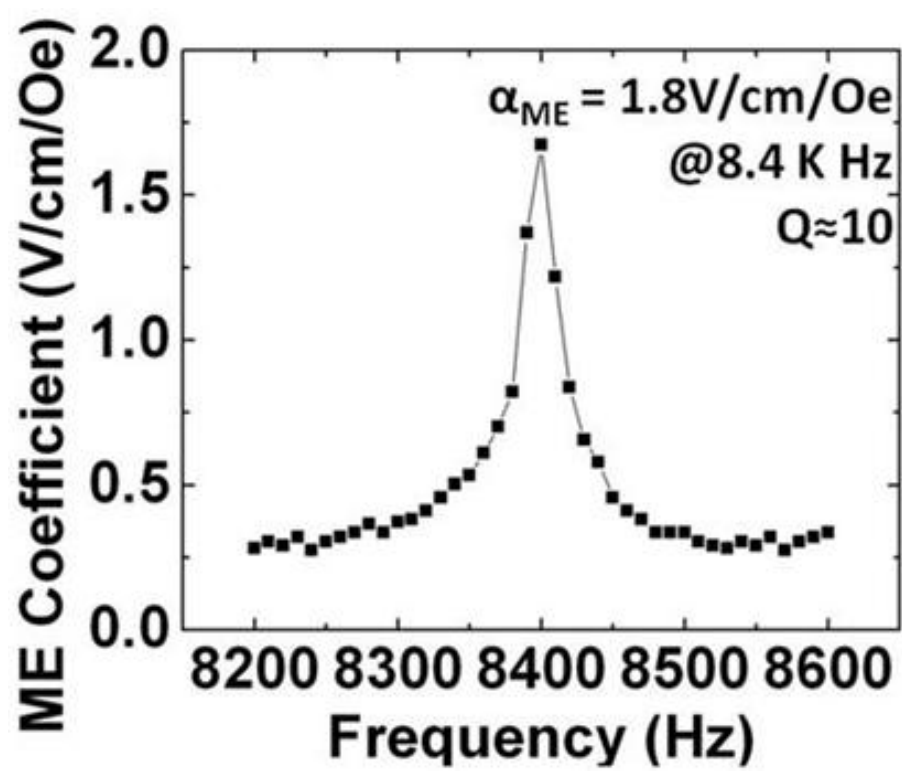


Figure 4-7. ME coefficient frequency response.

#### 4.1.2.2 Sensitivity and Noise Analysis

To analyze the performance of ME cantilever sensor system, the output characterization of ME cantilever sensors was characterized in the last section. At low frequency (20 Hz), the ME output voltage is 0.3 V/T while at resonance frequency (8.4 KHz), the ME output voltage is 1.8 V/T.

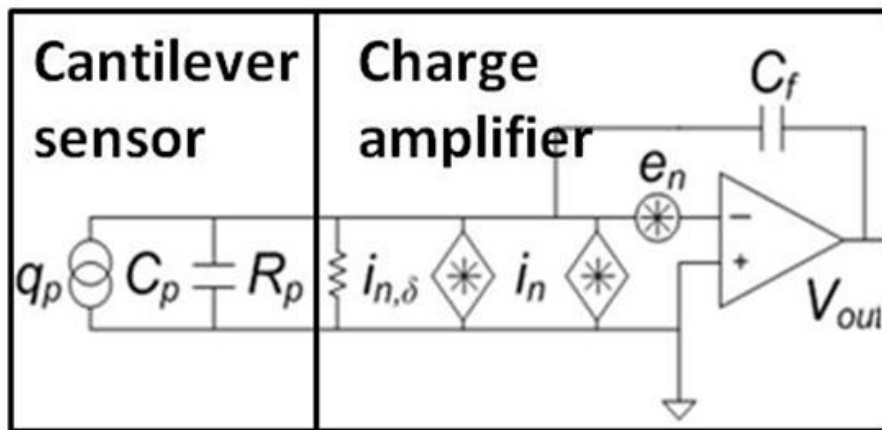


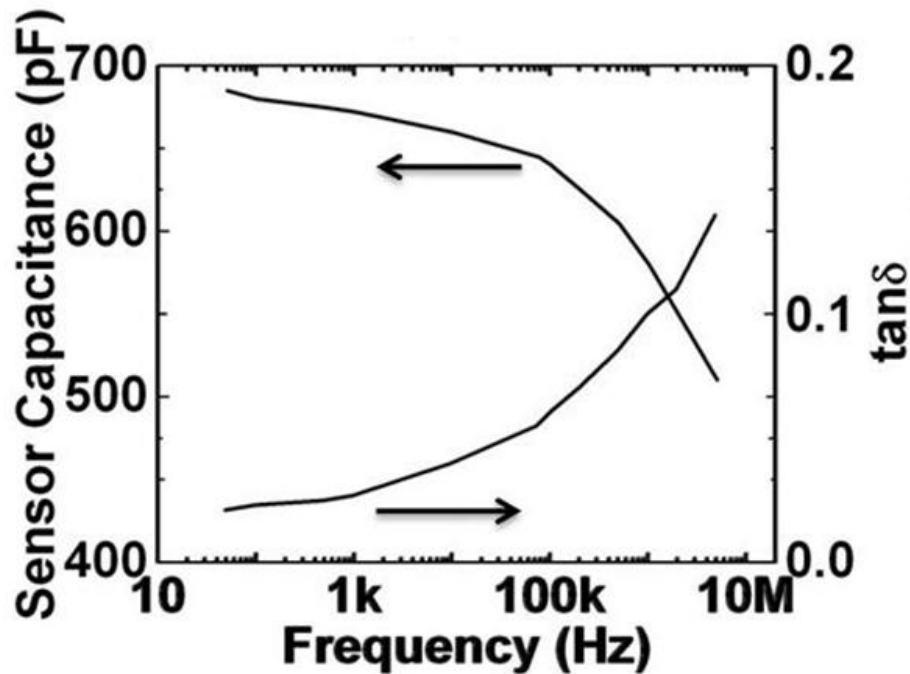
Figure 4-8. Equivalent circuit for ME cantilever sensor and charge amplifier with noise source.

The output noise performance was captured by a digital spectrum analyzer (DSA, hp 35670A). Figure 4-8 shows the equivalent small circuit diagram with noise source for both the ME cantilever sensor and readout charge amplifier. The total output noise density is mainly consisted of two types of noise: dielectric loss noise of the sensors and flicker noise of the charge amplifier. The dielectric loss noise is the major noise in the piezoelectric materials,

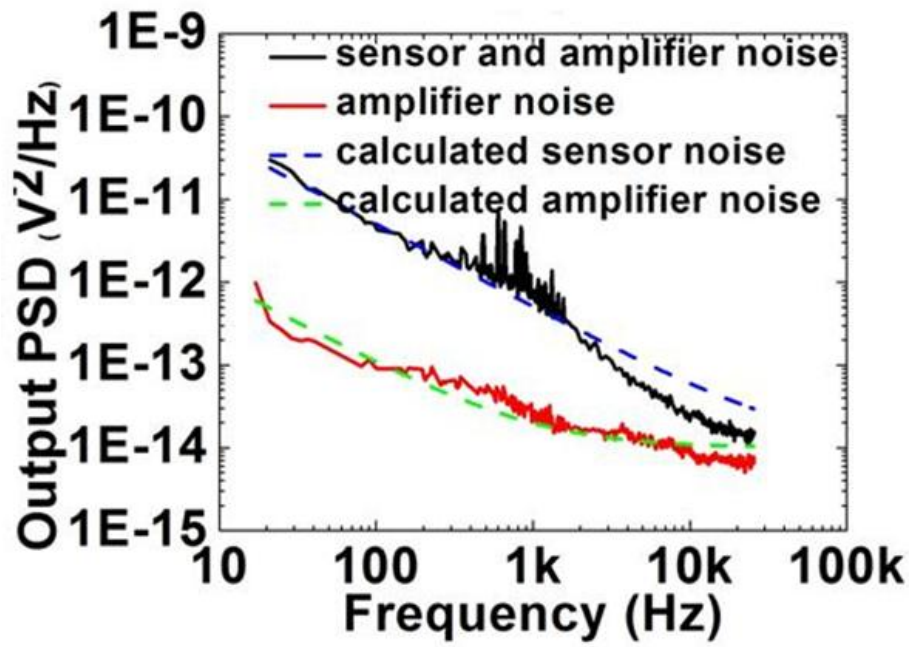
$$v_{sensor}^2 = i_d^2 * (R_{piezo} // C_{piezo})^2 = \frac{4kT}{\omega C_{piezo}} \frac{\tan \delta}{(1 + \tan \delta)^2}$$

where  $k$  is the Boltzmann constant,  $T$  the absolute temperature,  $\omega$  the angular frequency, and  $\tan \delta$  the loss tangent of the piezoelectric layer,  $C_{piezo}$  is the capacitance of PZT.

The sensor capacitance is dominated by the PZT capacitance, as shown in Fig. 4-9 (a), since Metglas<sup>®</sup> thin film is metallic material with high conductivity. The output noise density of the whole sensor system is shown Fig. 4-9 (b). The commercial charge amplifier noise, which is given by the data sheet and verified by DSA, exhibits an order magnitude lower than the sensor noise. As a result, the whole system noise is limited by the dielectric loss noise from the ME cantilever sensor. Based on the analysis above, the resolution (minimum detectable field (MDF)) of the ME cantilever sensor system is  $50 \mu\text{T}/\sqrt{\text{Hz}}$  at 20 Hz and  $125 \text{nT}/\sqrt{\text{Hz}}$  at 8.4 KHz [43].



(a)



(b)

Figure 4-9. (a) Frequency response of ME laminate cantilever sensor capacitance and dielectric loss factor. (b) Sensor output noise density.

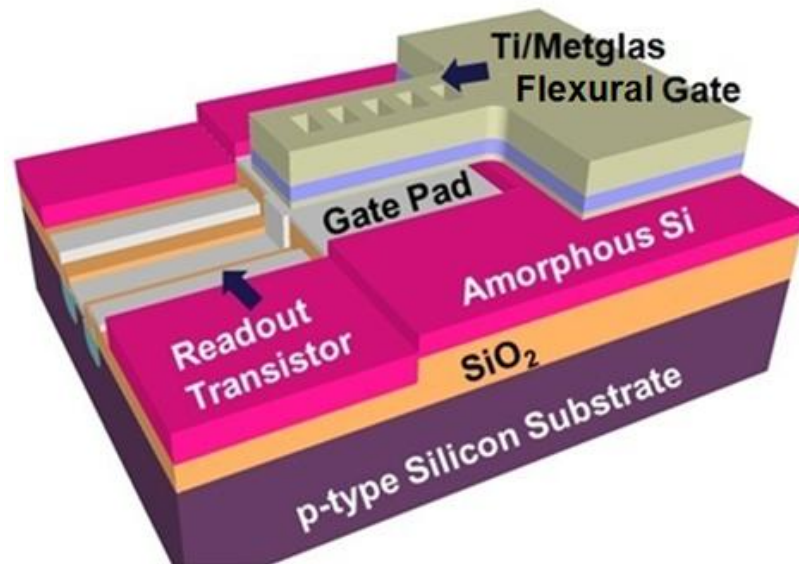
## 4.2 Magnetoelectric Flexural Gate Transistors

### 4.2.1 Design Considerations

In the last section, a monolithic nanofabrication of PZT/Metglas<sup>®</sup> ME laminate cantilevers sensor system has been demonstrated with 100 nT sensitivity at resonant frequency [44]. This device shows the compatibility of the nanofabricated cantilever ME sensors with the Si process technology and paves the way for the future magnetic sensors array integration with advanced Si nanoelectronics, however, the sensitivity is not comparable to the bulk ME laminate sensor and limits the practical applications. This is expected because the scaling in the sensor area results in the less polarization charge and platinum coated SOI substrate for PZT deposition forms an extra load for Metglas<sup>®</sup> thin film. Both leads to a lower output voltage from the ME cantilever sensors. Also, the dielectric loss noise from the piezoelectric layer limits the minimum detectable field and the complexity in PZT thin film process prevents the direct integration with CMOS technology.

In consideration of the need for high spatial resolution of magnetic field sensing applications, the current challenges in the state of the art pertain to the realization of high sensitivity magnetic sensor arrays. Motivated by this challenge, a novel structure is carried out to recover the sensor output voltage of integrated ME sensors from the scaling effect and eliminate the dielectric loss sensor noise. In this chapter, a new type of chip-scale magnetic sensors – a magnetoelectric flexural gate transistor (MEFGT) sensor by integrating a magnetostrictive (MS) Metglas<sup>®</sup> ( $\text{Fe}_{0.85}\text{B}_{0.05}\text{Si}_{0.1}$ ) thin film micromechanical cantilever directly atop a sensing and amplifying transistor, as shown in Fig. 4-10 (a). The device combines the merits of magnetoelectric laminates

[44] with the concepts of a flexural-gate transistor [45]. It replaces the piezoelectric stack layer (Pt/PZT/Pt/SiO<sub>2</sub>) with a single passive titanium layer. Several benefits arise from this simple structure. First of all, without the PZT stack layer, the whole process is more compatible to the advanced CMOS fabrication process. Second, this reduces the cantilever load from multilayer to single layer which improves the deflection of the cantilever. Finally and most importantly, the dielectric loss noise from the piezoelectric sensor is eliminated leaving only thermal-mechanical noise from air gap [46].



(a)

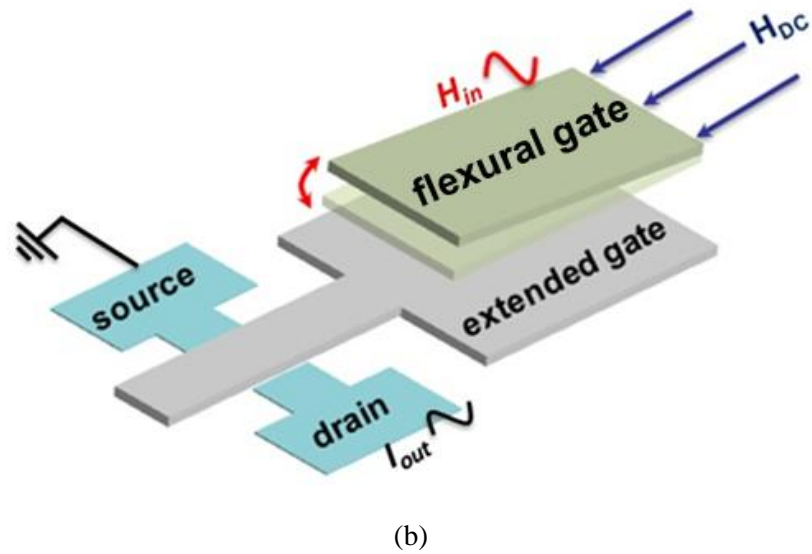


Figure 4-10. (a) Schematic of the magnetolectric flexural gate transistor (MEFGT). (b) The principle of operation of a magnetolectric flexural gate transistor (MEFGT).

Figure 4-10 (b) shows the operation principle of MEFGT. The MEFGT device consists of a freestanding unimorph cantilever made of magnetostrictive Metglas® film on a passive titanium film and is located directly atop an extended gate of a MOS readout transistor and with a small air gap in between [44]. Time varying ac magnetic field induces flexural bending motion in the suspended cantilever via magnetostriction effect which, in turn, modulates the air-gap capacitance. The air-gap capacitance modulation is sensed directly via modulation of the channel charge density in the field effect transistors (FETs) and is amplified by the transconductance of the FETs in the form of drain current modulation. Therefore, the MEFGT combines the benefits of high-deflection property of MS cantilever sensors with FET based motion sensing and amplification.

#### 4.2.2 MEFGT Fabrication

The magnetoelectric flexural gate transistor consists of a Metglas<sup>®</sup>/Ti top flexural gate and a capacitively coupled readout transistor [43]. The freestanding flexural gate uses a unimorph cantilever consisting of a Metglas<sup>®</sup> active sensing layer atop Ti passive layer. The major fabrication process steps shown in Fig. 4-11 include the following: 1) a standard NMOS transistor nanofabrication processes (a) – (d); 2) deposition of the sacrificial layer; 3) deposition and patterning of the active structure (e); and 4) final anneal and release (f). A total of six photolithographic steps were used in the fabrication of the MEFGT.

The fabrication process began with the growth of a 1  $\mu\text{m}$  thick field oxide ( $\text{SiO}_2$ ) on a single-side-polished,  $10^{15} \text{ cm}^{-3}$  doped, (100) p-type silicon wafer. The isolation silicon dioxide was deposited via wet thermal oxidation at 1050  $^\circ\text{C}$  at for 3 hours. The source and drain windows was then patterned by photoresist 3012 (4000rpm 45s) and contact aligner MA/BA 6 (8mW, 8s). Post bake at 120  $^\circ\text{C}$  is required before BOE (6:1 buffer oxide etchant) wet etching to improve the pattern window profile. This was followed by n+ doped source/drain formation via 20 min  $\text{POCl}_3$  liquid source pre-deposition at 1000  $^\circ\text{C}$  and 30 min 1050  $^\circ\text{C}$  wet oxidation drive-in annealing. The second mask was then used to pattern the gate oxide area. Gate dielectric was grown at 950  $^\circ\text{C}$  30 min using dry thermal oxidation and followed by a 30 min post annealing to improve the interface state. The third mask defined the source/drain via and BOE is used here to etch away the field oxide. The fourth mask was for the metal contact which is finished by the liftoff process. Electrode metallization for gate, source and drain used 10 nm/100 nm thick Ti/Pt metal deposition via RF sputtering at 200 W power under 2.5 mTorr Ar pressure. Up to this stage, a full

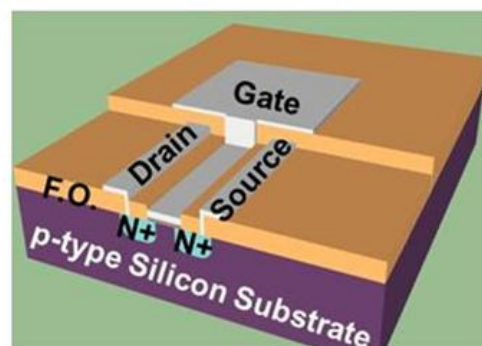
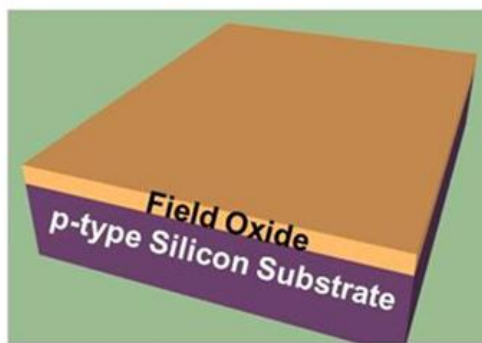
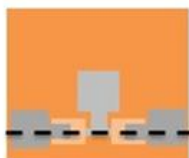
process sequence for 1  $\mu\text{m}$  NMOS Si transistors was complete, including field oxide deposition, source/drain diffusion, gate oxide deposition, contact via etching, and electrode patterning (Fig. 4-11 (b) - (d)). This was followed by the fabrication of the top flexural gate structure, for which a 500 nm amorphous silicon was chosen as the sacrificial material, deposited by plasma enhanced chemical vapor deposition. The use of an amorphous silicon sacrificial layer, ensures a rapid release of the cantilever structure while the use of the  $\text{XeF}_2$  minimizes damage of the transistor gate oxide and provides a highly selectivity to photo resist protection mask used to prevent the lateral undercutting of the anchor areas. PECVD deposition for A-Si used Ar as the carrier gas and  $\text{SiH}_4$  as precursors. The reason that we use Ar instead of commonly used  $\text{H}_2$  as carrier gas is to improve the adhesion between  $\text{SiO}_2$  and A-Si. Tape test has confirmed the good adhesion. The conditions for deposition were 200 W rf power and 2 Torr gas pressure at 220  $^\circ\text{C}$ . Next, a 500 nm thick layer of titanium and a 100 nm thick Metglas<sup>®</sup> films were deposited using a sputtering process, and defined using a lift-off technique to form a 300  $\mu\text{m} \times 100 \mu\text{m}$  MS cantilever, as shown in Fig. 4-11 (e). The in-situ magnetization ion mill sputtering was used to deposit Metglas<sup>®</sup> film, which was describe in the last chapter [47, 48]. Finally, the last lithography defined the region to release the cantilever structures were released by a xenon difluoride ( $\text{XeF}_2$ ) dry etching process and annealed at 350  $^\circ\text{C}$  on hotplate to release internal stress (Fig. 4-11 (f)). The photoresist protected the thin gate oxide from being attached in  $\text{XeF}_2$  etching and was removed after release by  $\text{O}_2$  plasma etching. More fabrication details can be found in Appendix B.

- Silicon
- SiO<sub>2</sub>
- Gate Oxide
- N diffusion
- Pt
- Amorphous Silicon
- Ti
- Metglas

Cross-sectional View



Top View



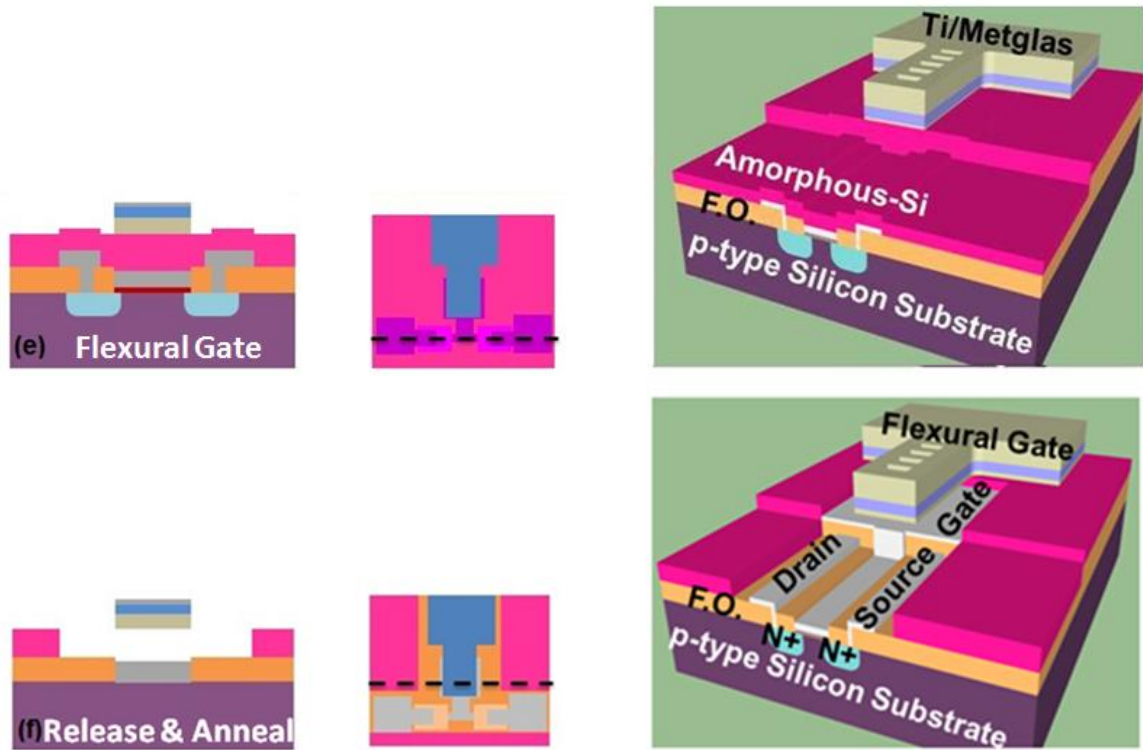


Figure 4-11. Schematic of the fabrication process (not to scale). (a) Deposition of 1  $\mu\text{m}$  thermal field oxide on p-type silicon wafer. (b) Pattern and wet etch field oxide for source drain formation via solid source diffusion. (c) Gate oxide pattern and deposition. (d) Gate electrode metallization using liftoff process. (e) Deposition of 500 nm-thick amorphous silicon for the sacrificial layer and lift-off Metglas/Ti. (f) Patterning to prevent unwanted undercutting during release step and release cantilever structure using  $\text{XeF}_2$  isotropic etching.

Figure 4-12 (a) and (b) show the SEM image of MEFGT and the freestanding cantilever gate structure, respectively. The offset between the cantilever tip end and the transistor gate pad arises from the cantilever bending. This will be confirmed by the optical characterization (in the following section) which is taken by the ZYGO<sup>®</sup> microscopy. The top flexural gate is bent-up by  $\sim 5 \mu\text{m}$  at the tip end due to the larger residual tensile stress in the Metglas<sup>®</sup> film in comparison to the Ti passive layer leading to a decrease in the air gap capacitance [49].

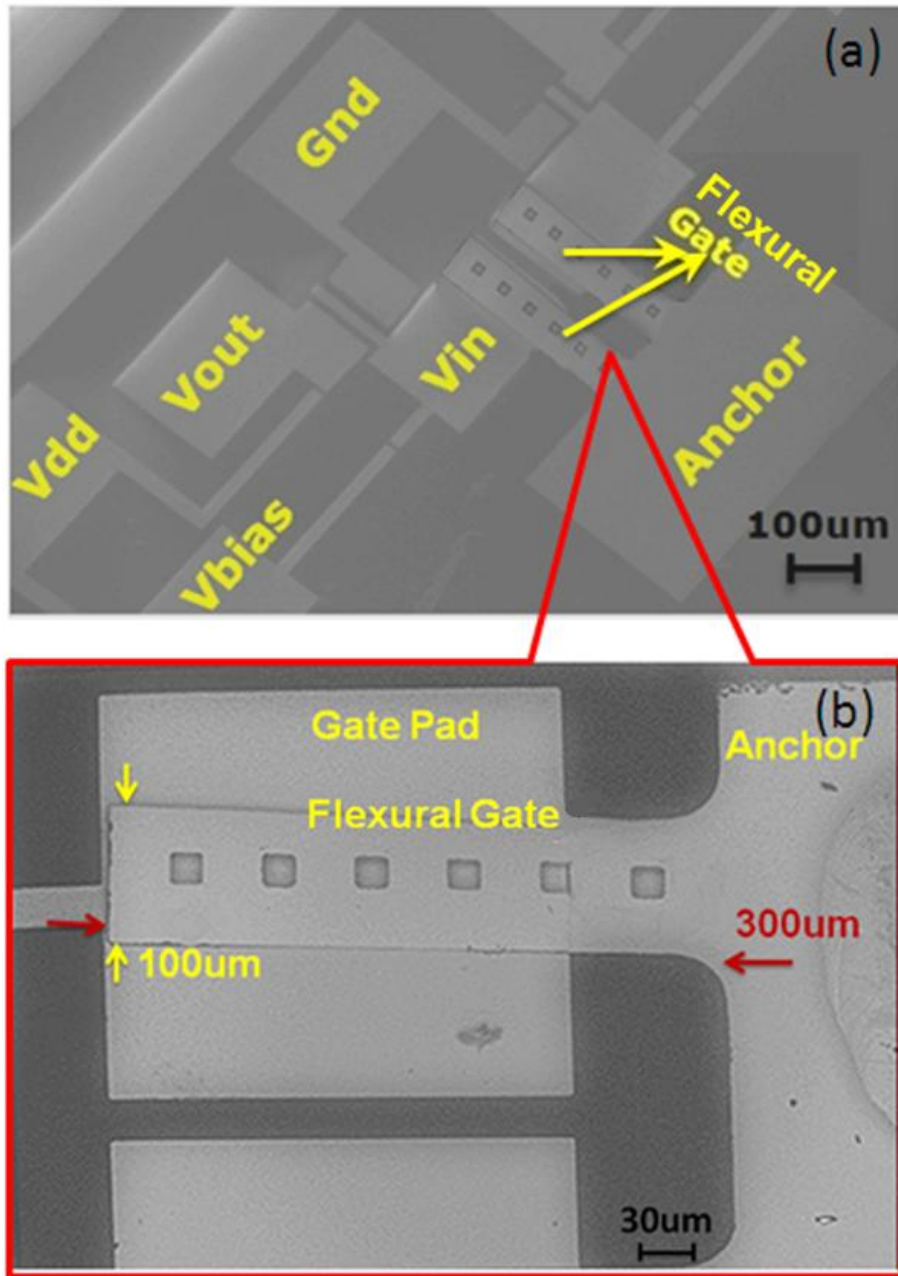
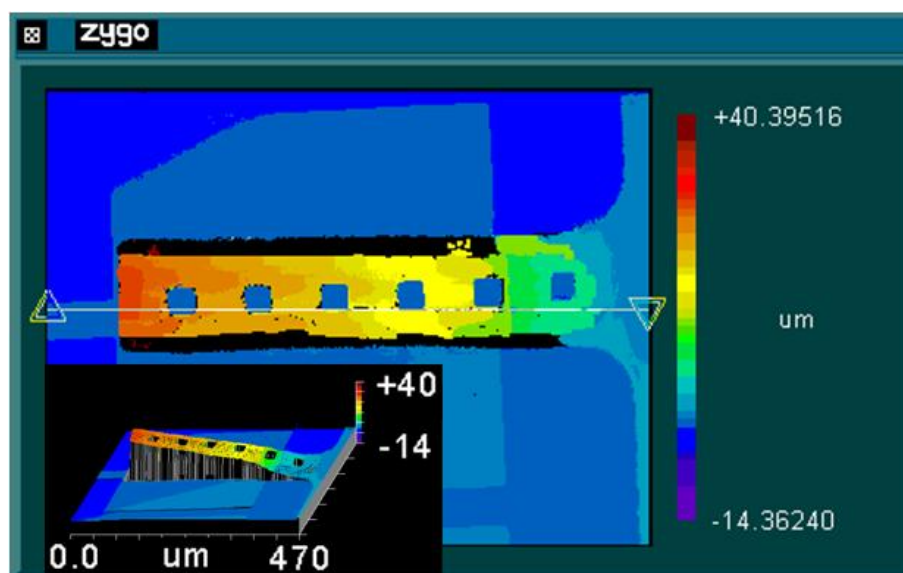


Figure 4-12. (a) Scanning Electron Microscopy (SEM) of magnetolectric flexural gate transistor (MEFGT). (b) A 300 μm long and 100 μm wide flexural gate.

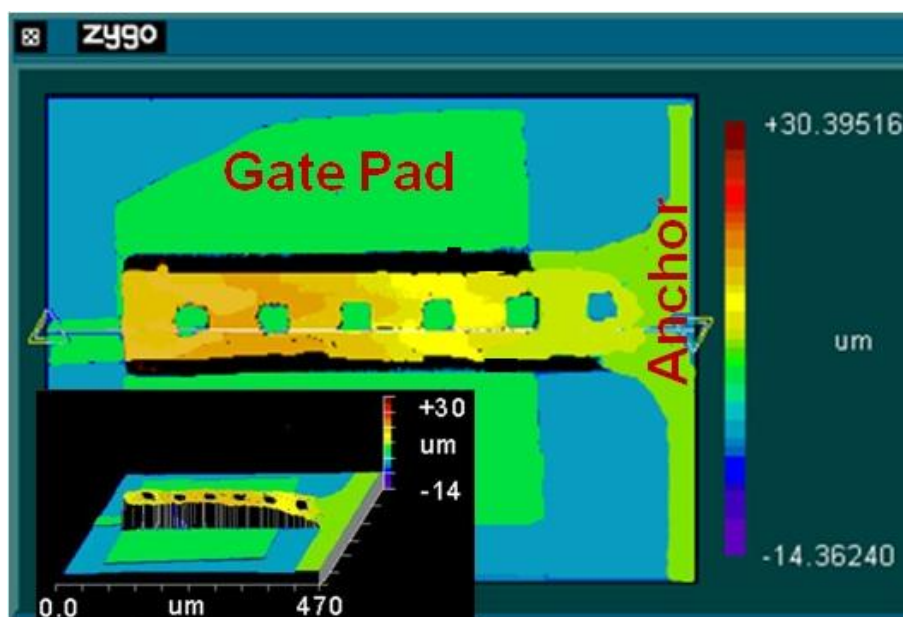
### 4.2.3 MEFGT Performance

#### 4.2.3.1 MEFGT Optical Characterization

An inherent problem associated with the bilayer thin film MS cantilevers is the zero field curvature of the released cantilever beam due to the residual stress mismatch between films. To verify the assumption of flexural gate bending, a white light interference (ZYGO<sup>®</sup>) microscopy was used to image the altitude of cantilever beam. Figure 4-13 (a) shows the ZYGO<sup>®</sup> image of the freestanding magnetostrictive cantilever forming the gate electrode of the MEFGT. As can be seen from the white light interferometric image of the cantilever at zero field (inset Fig. 4-11 (a)), the freestanding MS cantilever is bent upwards by 25  $\mu\text{m}$  at the tip end due to the larger residual tensile stress in the Metglas<sup>®</sup> film in comparison to that of the Ti passive layer and therefore results in a smaller air gap capacitance. The bending problem of the cantilever beam can be improved by thermal annealing, as seen in Fig. 4-11 (b), after 350  $^{\circ}\text{C}$  hot plate annealing for 5 min, the bending curvature reduces to 5  $\mu\text{m}$  (inset Fig. 4-4 (b)) but can hardly be avoided because of the thermal expansion coefficient difference. Moreover, the annealing time and temperature has been optimized: lower temperature and shorter time annealing has less effect while higher temperature and longer time disturbs the magnetic domain alignment and results in a less magnetostrictive coefficient.



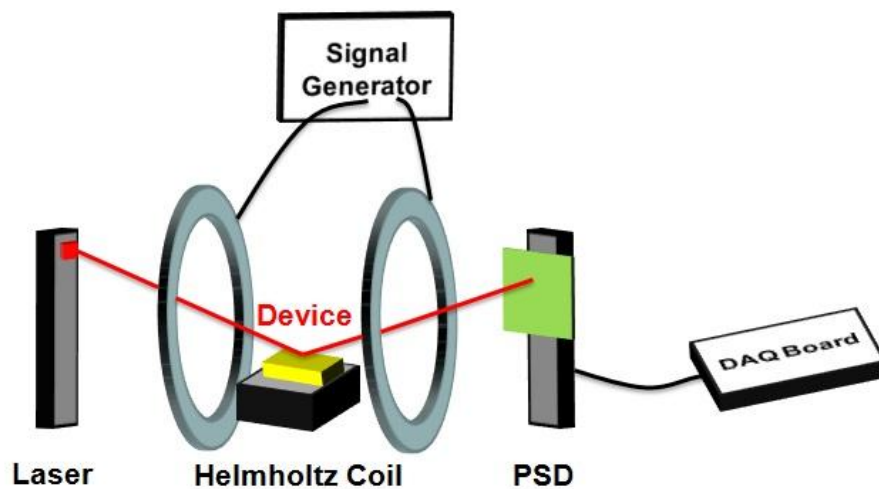
(a)



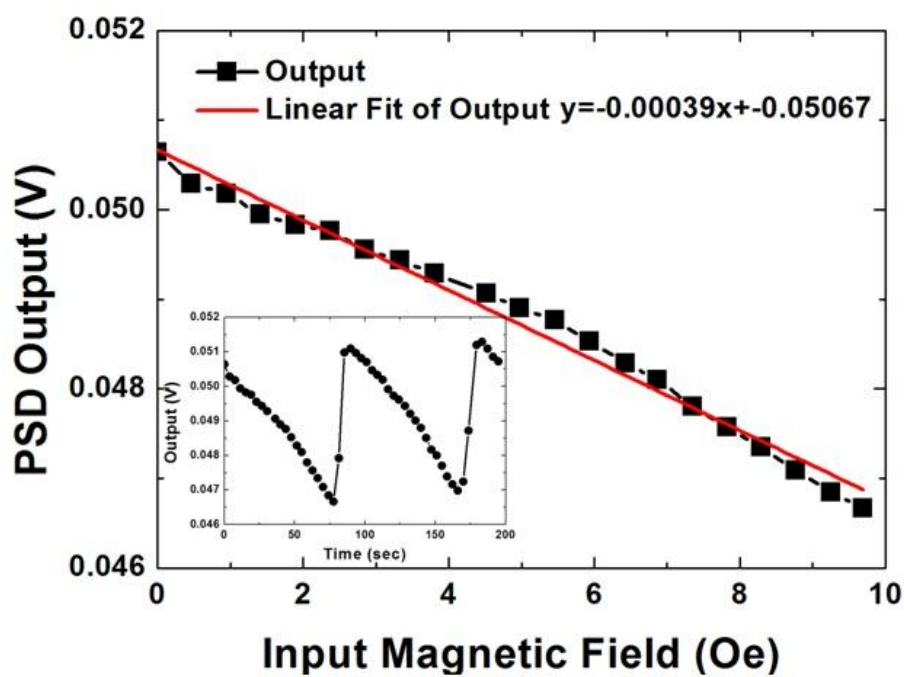
(b)

Figure 4-13. White light optical interference microscope (Zygo<sup>®</sup> NT100) image of the freestanding magnetostrictive top flexural cantilever gate structure (a) without annealing (b) with 350 °C annealing for 5 min.

To examine the functionality of the flexural gate, a custom designed optical measurement system has been setup. The experimental system uses a position sensitive photo detector (PSD) to measure the deflection of the beam, as illustrated schematically in Fig. 4-14 (a). A 600 nm wavelength laser was focused and directed onto the flexural gate tip and is actuated by the magnetic field generated using a Helmholtz coil. The reflected laser beam was detected by the Stiek Electro-Optics 2D PSD and the output was acquired using a National Instruments® data acquisition box. HP 3314A function generator was used to drive the Helmholtz coil using a triangle wave with 95%-5% symmetry to output a 0 – 1 Oe magnetic field. Figure 4-14 (b) plots the output of PSD, which shows a linearly decreasing output as a function of the applied magnetic field using the Helmholtz coil. This result confirms that the freestanding magnetostrictive cantilever responds to the incident magnetic signal via flexural bending. Calibrating the applied magnetic field the response of the PSD can be converted into an optically measured sensitivity of  $0.04 \text{ mV}/\mu\text{T}$ .



(a)



(b)

Figure 4-14. (a) Schematic of optical measurement set-up using position sensitive photo detector. (b) PSD output varies linearly with input magnetic field. (Signal generator provides a triangle wave with 95%-5% symmetry at a frequency of 0.01 Hz,  $5.95 V_{pp}$ , with an offset of 3.0 V.)

#### 4.2.3.2 MEFGT Electrical Characterization

For the complete electrical characterization, the devices were then placed in a dual in-line package and electrical connections were made via conventional wire bonding. The performance of the MEFGT was thereafter characterized using the configuration outlined in Fig. 4-15. The measurement was performed in a magnetically shielded enclosure to avoid the disturbance of the terrestrial field and the ambient electromagnetic noise. An electromagnet controlled by the function generator provides both input AC magnetic field,  $H_{in}$ , and DC bias magnetic field,  $H_{DC}$ . All the magnetic field of the Helmholtz coil and magnet in this measurement was calibrated by LakeShore 450 Gauss-meter. The input capacitance was captured using an Andeen Hagerling ultra precision capacitance bridge (AH2700A) setup and the output voltage was measured using a Stanford Research 830 Lock-in Amplifier and a 35670A HP Dynamic Signal Analyzer (DSA).

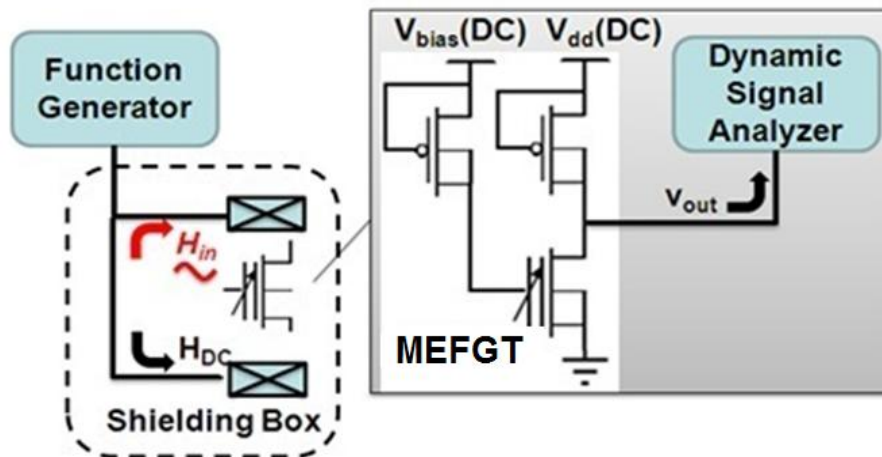


Figure 4-15. Schematic of ac magnetic field measurement set-up.  $H_{in}$  is the AC magnetic field to be detected.  $H_{DC}$  is the DC bias magnetic field.

The top flexural gate capacitor performance was first characterized. The change in the air-gap capacitance is captured at 100 Hz with a DC magnetic bias field. The DC air-gap capacitance as well as the differential AC capacitance between the top flexural gate and the extended transistor gate pad as a function of the DC magnetic bias field is shown in Fig. 4-16. As expected, the capacitance changes as a function of the DC bias magnetic field due to the magnetostrictive effect in Metglas<sup>®</sup>. The asymmetric AC response results from the fringe field magnetization during the sputtering process, which causes the magnetic domains located in a certain angle than expected. The domains need more moment change to rotate in one direction than the other. The AC peaks occur at 5 Oe & -7 Oe.

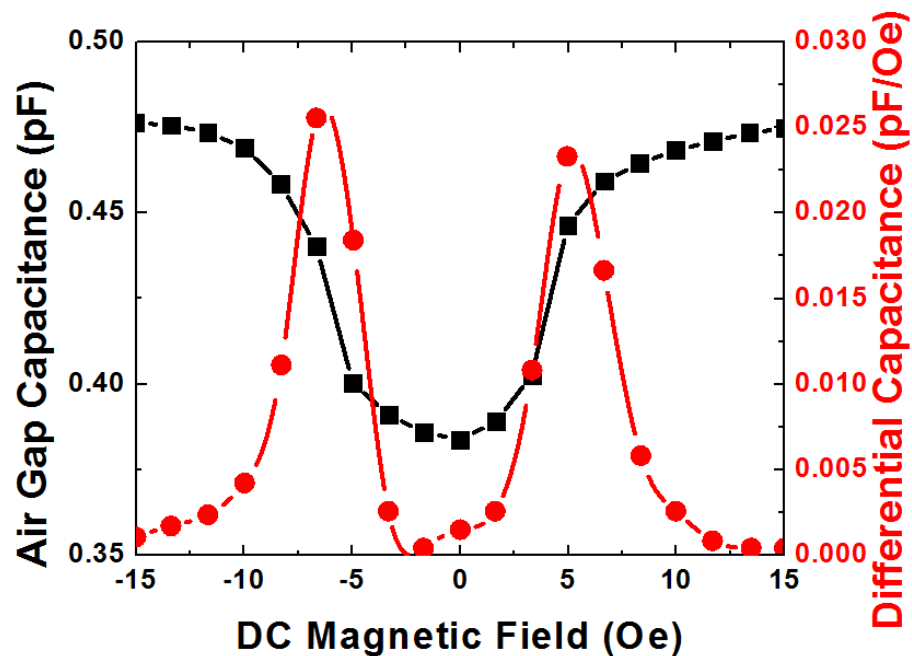


Figure 4-16. Flexural gate air gap capacitance (black) and differential capacitance (red) as a function of the applied magnetic bias field.

The analytical model of the static characteristics of the microcantilever is studied to understand how the bending problem affects the capacitance. The model expresses the relation between the

applied magnetic field and the differential capacitance. Due to the curvature of the cantilever beam, the parallel plate capacitance between the freestanding MS cantilever and the gate electrode assumption is no longer valid. Detailed modeling accounts for the anticlastic bending of the cantilever. A schematic illustration of the cantilever is shown in Fig. 4-17 which is extracted from the ZYGO® image. Not only the longitudinal stress but also the transverse stress affects the shape of the beam. By applying a two-dimensional (2D) bowing approximation, which results from the 2D residual stress, we extract two parameters, effective area,  $A_{eff}$  and effective gap,  $d_{eff}$ . An approximate expression for the effective width conditions using polynomial curve fitting is given by

$$w_{eff}(d) = w \left( 1 - 0.2 \frac{(d - 0.5)^2}{w} \right)$$

where  $w$  is the cantilever width and  $d$  is the distance between cantilever (top flexural gate) and bottom plate (transistor gate pad). Correcting for the fringing field effect, punch through via holes, and the cantilever length, the effective area  $A_{eff}$  is expressed as

$$A_{eff} = \alpha(A) \int_d w \left( 1 - 0.2 \frac{2(d - 0.5)}{w} \right) \Delta d$$

where  $\epsilon_0$  is air permittivity and  $\alpha(A)$  is the correction factor. Similarly, an approximation for the effective gap  $d_{eff}$  can be obtained as follows:

$$d_{eff}(x, y) = 0.5 + \frac{y^2}{18000} \Big|_l + \frac{x^2}{5000} \Big|_w$$

where  $l$  is the cantilever length. Taking into accounting both effective parameters described above, the effective capacitance  $C_{eff}(A,d)$  is given by

$$C_{eff} = \frac{\epsilon_0 A_{eff}}{d_{eff}} = \alpha(A) \epsilon_0 \int_A \frac{w(1-0.2 \frac{2(d-0.5)}{w})}{d} \Delta d$$

$$= \alpha(A) \epsilon_0 \int_{-w/2}^{w/2} \int_0^l \frac{w(1-0.2 \frac{2(\frac{y^2}{18000} + \frac{x^2}{5000})}{w})}{0.5 + \frac{2y}{18000} + \frac{2x}{5000}} \Delta x \Delta y$$

and the capacitance change is given by

$$\Delta C = C_{eff} \frac{\delta}{d_{eff}}$$

where  $\delta$  is the top flexural gate deflection, which can be calculated as[34, 35]

$$\delta = \frac{3l^2}{t_m} \frac{AB(B+1)}{A^2 B^4 + 2A(2B + 3B^2 + 2B^3) + 1} d_{31}^m H_{in}$$

where  $A=E_p/E_m$  is Young's modulus ratio,  $B=t_p/t_m$  is thickness ratio,  $d_{31}^m$  is magnetostrictive coefficient, and  $H_{in}$  is the input ac magnetic field.

Table 4-1 summarizes all the parameter values for the flexural gate differential capacitance study.

3D COMSOL<sup>®</sup> simulations with with antielastic stress (Fig. 4-18) were also performed to



Table 4-1. Parameters for Metglas® Flexural gate.

Symbol	Description	Value
$E_P$	Young's modulus for Ti, (GPa)	116
$E_M$	Young's modulus for Metglas, (GPa)	110
$t_p$	Thickness modulus for Ti, (nm)	500
$t_m$	Thickness modulus for Metglas, (nm)	100
$\rho_p$	Density for Ti, ( $\text{g/cm}^3$ )	4.5
$\rho_m$	Density for Metglas, ( $\text{g/cm}^3$ )	7.7
$w$	Width of flexural gate, ( $\mu\text{m}$ )	100
$l$	Length of flexural gate, ( $\mu\text{m}$ )	300
$\epsilon_0$	Permittivity of air, (F/m)	$8.84\text{e-}12$
$d_{31}^m$	Magnetostrictive coefficient, (ppm/Oe)	$3.4(@ 6 \text{ Oe})$

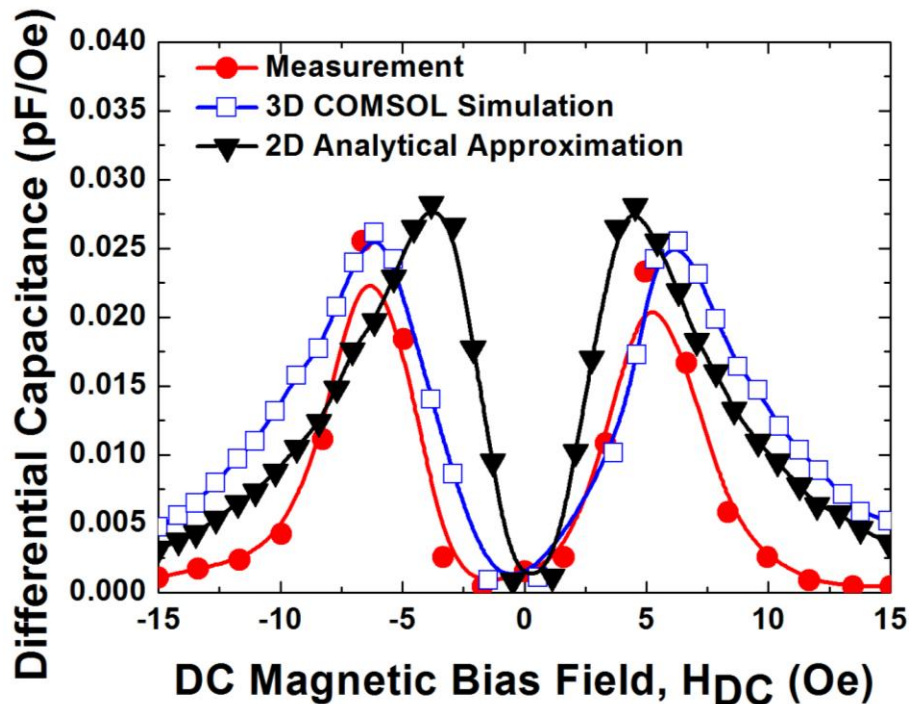


Figure 4-19. Differential capacitance versus DC magnetic bias field: comparison between measurement, 3D COMSOL simulation and 2D analytical approximation.

The transfer characteristic of the readout circuit is shown in Fig. 4-20. The transistors are biased at the peak transconductance point to get the maximum response. The equivalent circuit of MEFGT in Fig. 4-21 illustrates that capacitance modulation is amplified by the transconductance.

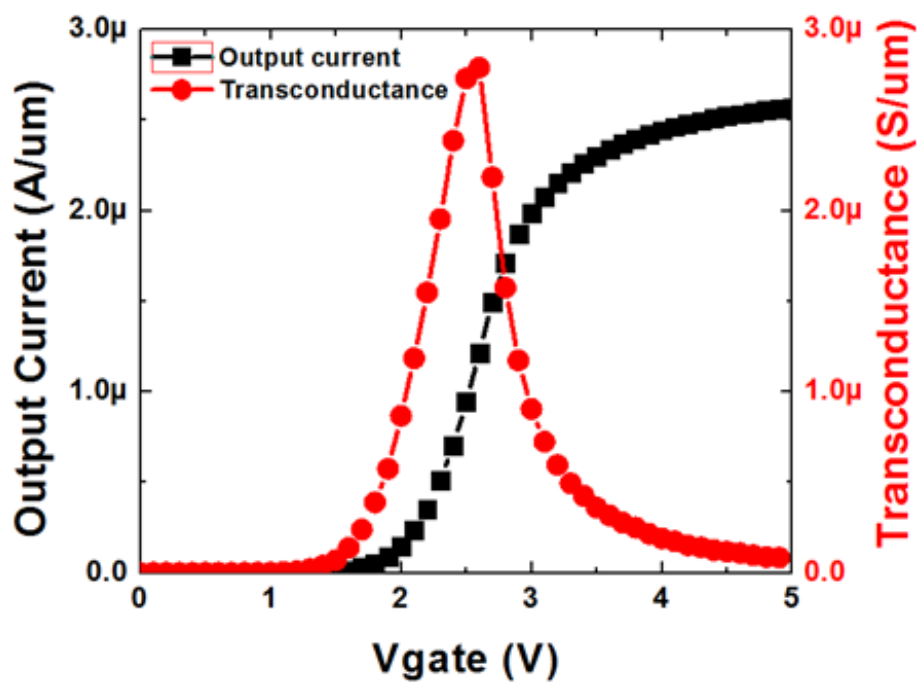


Figure 4-20. Transfer characterization of common source readout circuit.

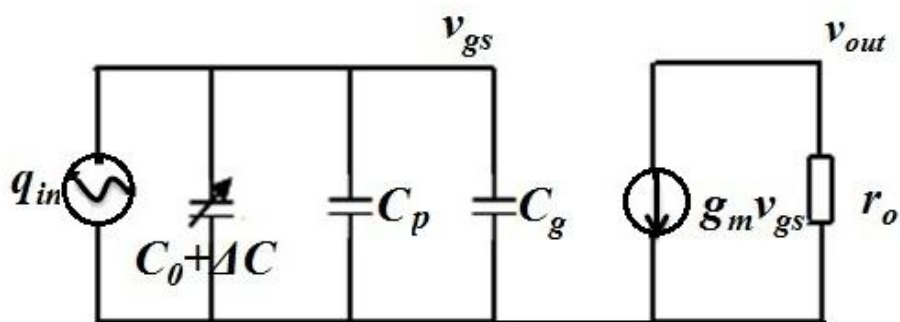


Figure 4-21. Small signal equivalent circuit for MEFGT.

Figure 4-22 presents the low frequency AC output voltage of the transistor integrated with the MS cantilever as a function of the applied DC magnetic bias field as measured by the common source readout amplifier circuit for a 0.38 Oe input AC magnetic field oscillating at 20 Hz. The

result shows that the output voltage follows the input capacitance change with DC magnetic bias field.

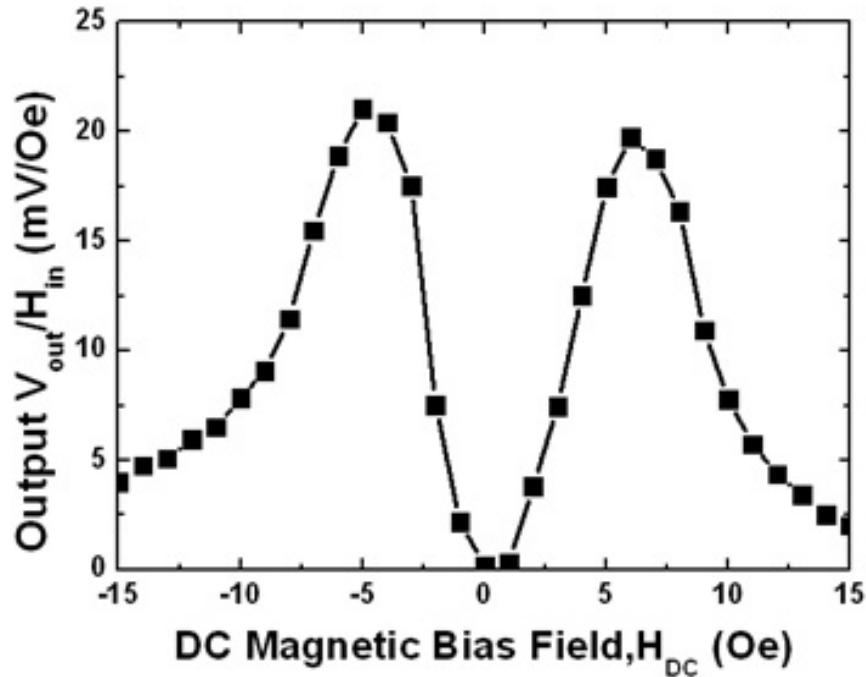


Figure 4-22. Output voltage of common source readout amplifier circuit as a function of the DC magnetic field. The data was measured at 20 Hz and  $H_{in} = 0.38$  Oe.

The frequency response of the MEFGT was studied both in air and vacuum ( $10^{-3}$  Torr), as shown in Fig. 4-23. The vacuum measurement was performed in a separate setup. A custom-made Helmholtz coil was used to generate the AC input magnetic field while the DC bias field was provided by a permanent magnet placed inside the chamber. The use of the permanent magnet avoids the coil from overheating due to the passage of large DC current. The magnetic field of the magnet was also calibrated by the Gaussmeter and the position of the sensor was adjusted to match the bias field corresponding to maximum output. The entire set-up was pumped down to mTorr pressure range using a dry pump. After the vacuum (pressure) in the chamber stabilized,

the chamber was valved off and physically disconnected from the pumping system to isolate it from the undesired mechanical vibration of the pump. The output of the sensor was measured by sweeping the frequency of the magnetic field at constant amplitude. The device resonance frequencies and the  $Q$ -factor were determined to be 4.27 kHz and 12 (in air) and 4.9 kHz and 24 (in vacuum) respectively. At resonance, the output voltage increases by  $\sim 10$  times (in air) and  $\sim 20$  times (in vacuum) in comparison to the off resonance output. The observed resonance behavior in both air and vacuum was confirmed using a modal analysis in COMSOL<sup>®</sup> finite element multi-physics software. By adjusting the mass damping parameter in the Rayleigh damping model, we were able to match the frequency response in air.

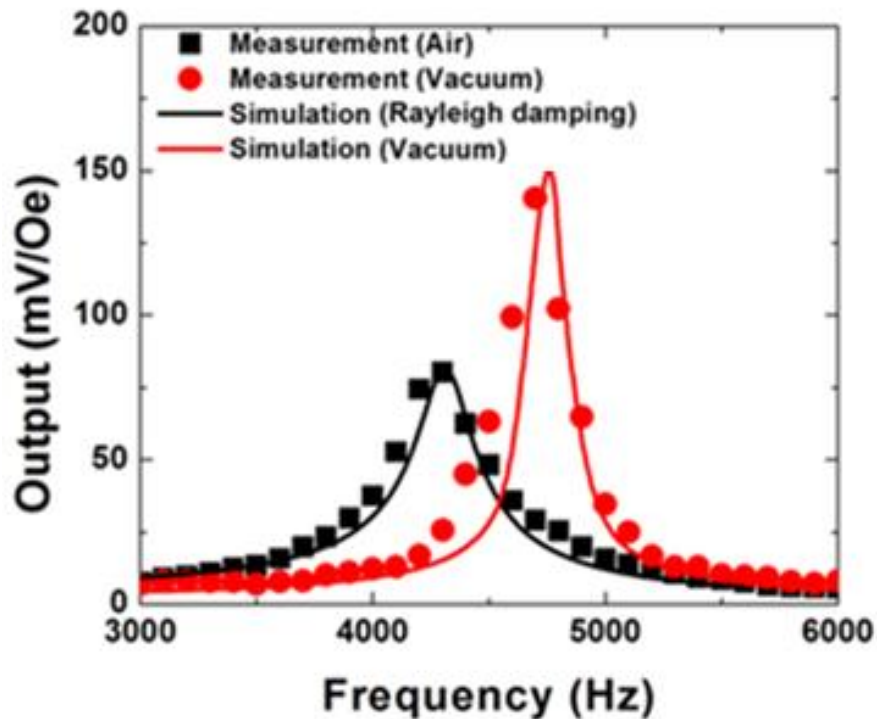


Figure 4-23. MEFGT frequency response measurement and simulation in both air and vacuum.

#### ***4.2.3.2 Sensitivity and Noise***

Noise measurement is taken to extract the noise voltage, shown in Fig. 4-24. It is seen that the flicker noise of the input transistor limits the noise floor of the entire system. At low frequency (20 Hz), the output noise density is  $1.5\text{E-}12 \text{ V}^2/\text{Hz}$  and at resonant frequency (4.9 KHz), the noise is  $2.9\text{E-}14 \text{ V}^2/\text{Hz}$ . Combining the output ME voltage of MEFGT, we achieved a sensitivity of  $0.22 \text{ mV}/\mu\text{T}$  at 1 Hz and  $1.47 \text{ mV}/\mu\text{T}$  at 4.9 KHz and a resolution (minimum detectable field) of  $60 \text{ nT}/\sqrt{\text{Hz}}$  at 1 Hz and  $150 \text{ pT}/\sqrt{\text{Hz}}$  at resonance. In Fig. 4-25, we demonstrate the detection of 3 nanoTesla input magnetic signal at the resonant frequency. This result represents a significant enhancement in comparison to the first integrated ME sensor demonstrated by Y. Lu and A. Nathan with 40 micro Tesla detectable field [50].

Table 4-2 summarized the resolution in different ME sensors presented in this work. It shows that the MEFGT has a significant improvement in comparison to ME cantilever sensors and approaches the sensitivity which bulk ME sensor has achieved. Comparing MEFGT to the current magnetic sensing technology [51], we have benchmarked our MEFGT performance in Fig. 4-17. The MEFGT is comparable to the flux gate magnetometer and has the potential to challenge the SQUID to achieve picoTesla minimum detectable field.

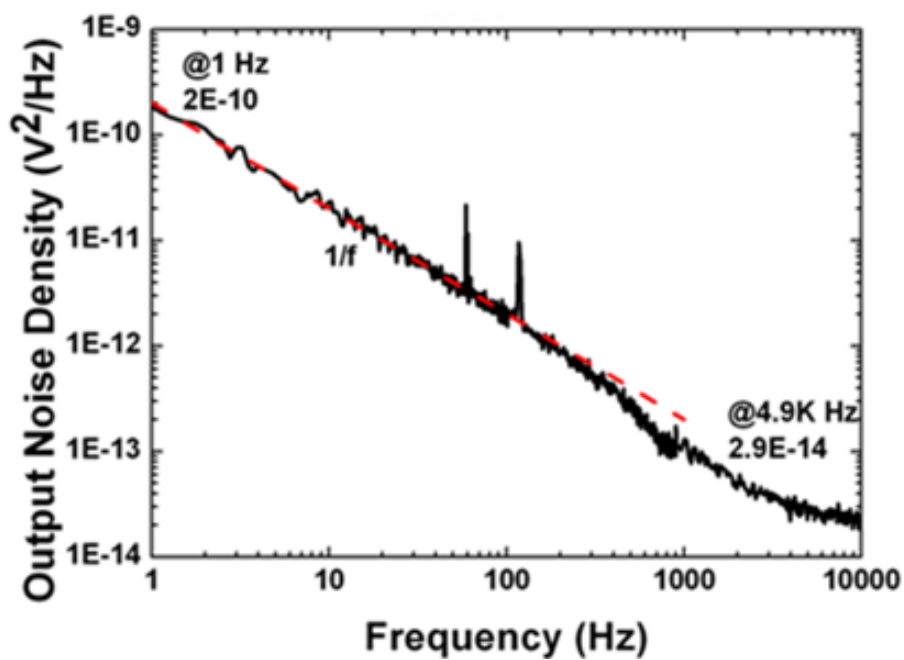


Figure 4-24. Output noise performance of MEFGT.

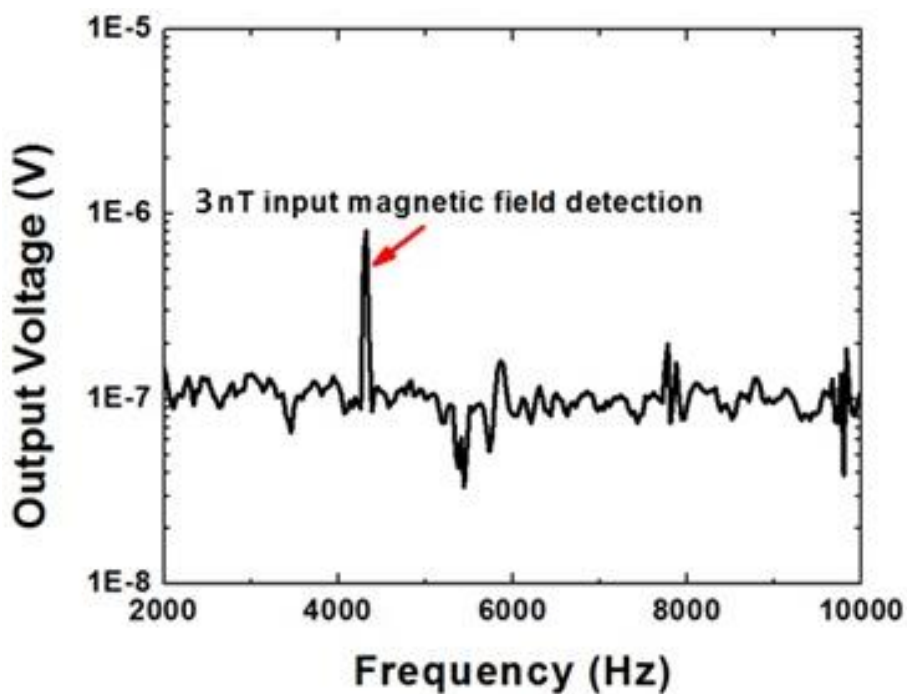


Figure 4-25. Frequency spectrum of 3 nanoTesla input ac magnetic field. (The DC magnetic bias field is set at 7 Oe. 3nT AC magnetic field is the minimum generated by the measurement setup.)

#### 4.2.4 MEFGT Noise Modeling

Low frequency noise has been used as an indication of the device quality and reliability. Previous noise analysis on the ME cantilevers sensors and MEFGT points out that noise density is an importance factor in affecting sensor performance. The device sensitivity can be simply improved only by noise reduction [52, 53]. Typical bulk ME laminates sensor noise is limited by the dielectric loss noise from the piezoelectric materials and thermal noise from the external biasing resistor [54], however, it should be noted that the noise level in the MEFGTs is limited by the flicker noise in the charge sensing readout transistors. To understand the noise mechanism in MEFGTs, detailed analysis is presented in this section.

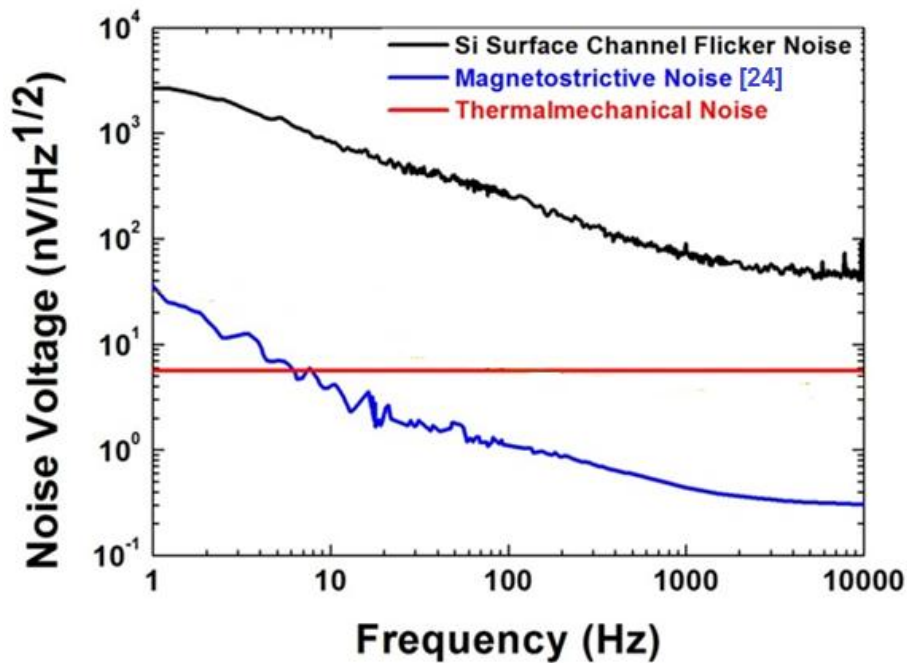


Figure 4-26. Noise density of MEFGT, including measured and modeled transistor flicker noise, modeled cantilever thermal fluctuation and magnetostrictive noise. The transistor flicker noise is dominant over the entire frequency range.

The overall noise sources in the MEFGT can be divided into three parts: transistor flicker noise, cantilever thermomechanical noise, and magnetostrictive noise. For the transistor in saturation, the expression for flicker noise spectrum is given by [55-57]

$$S_{v_g} = \frac{q^2 N_{ot}}{C_{ox}^2 WL} \frac{1}{f}$$

where  $C_{ox}$  is oxide capacitance per unit area,  $W$  and  $L$  are transistor width and channel length respectively,  $N_{ot}$  is the equivalent oxide trap density,  $q$  is the coulomb charge constant and  $f$  is the frequency. The  $1/f$  noise originates from fluctuations in the conductivity and can also be caused by the fluctuations in the mobility of the total number of charge carriers, or both.

Thermomechanical noise arises as a consequence of the cantilever being in thermal equilibrium with its environment. With the assumption that the thermomechanical noise spectrum is white (i.e. frequency independent), the cantilever deflection noise spectral density can be expressed as [58]

$$S_x = \frac{4k_B T}{k_{eff} \omega_0 Q}$$

where  $k_B$  is the Boltzmann constant,  $T$  is the temperature,  $\omega_0$  is the resonant frequency,  $Q$  is the quality factor, and  $k_{eff}$  is effective stiffness constant [59]. The equivalent cantilever thermomechanical output noise voltage is calculated by the cantilever deflection equation in last chapter.

Magnetostrictive noise yields a  $1/f$  type noise which is indicative of a localized low-frequency relaxation in the magnetostrictive response [60]. Figure 4-26 summarizes the output noise voltages originating from the three main noise sources. The transistor flicker noise, which is limited by the current fabrication process of surface channel transistors, is the dominant noise source in our MEFGT. One can reduce the noise density by introducing more advanced transistors with much lower flicker noise, for example, with the introduction of advanced SiGe quantum well buried channel transistors [61], there will be a significant reduction in the transistor noise level resulting in an enhanced integrated sensor performance. The noise performance of the SiGe quantum well FETs is discussed in the following section.

## 4.2.5 SiGe Quantum Well Transistors Noise Modeling

### 4.2.5.1 Background

Novel channel architectures incorporating strained quantum-wells are expected to enhance the performance and energy efficiency of future CMOS transistors [62]. High performance short channel PMOS transistors have been demonstrated using biaxial compressively strained SiGe quantum-well with Ge mole fraction  $\geq 50\%$  [63, 64]. As logic transistors continue to scale following Moore's Law, the More than Moore initiative calls for functional diversification in addition to scaling advances. One such application is direct integration of magnetoelectric sensors with CMOS transistors for developing chip-scale ultra sensitive magnetometers [32]. Since the sensitivity depends on the input gate noise of the readout transistor amplifier, the quantum-well transistor (QWFET) architecture is a promising option towards improving the noise performance.

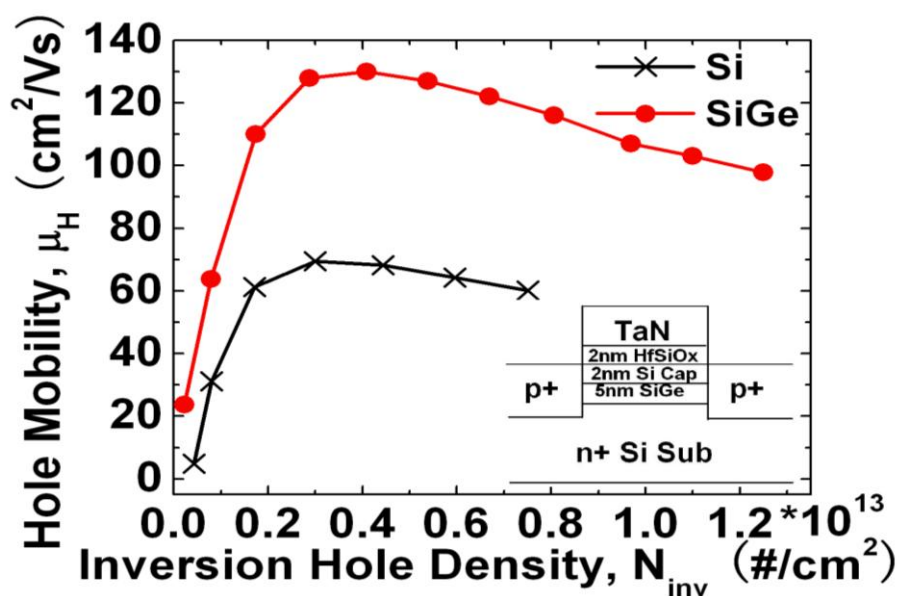
Superior noise performance for Si/Si<sub>1-x</sub>Ge<sub>x</sub> pMOSFETs has been reported by several groups [65-70] with various Ge mole fractions and varying Si cap layer thicknesses, albeit at long gate lengths ( $L_g$ ). However, most report loss of advantage at high  $V_g$  due to surface channel formation in the Si cap layer. Thinning of Si cap layer to prevent parasitic channel formation leads to increased  $D_{it}$  which in turn increases noise [71]. In this section, we will discuss record low flicker-noise characteristics in biaxial compressively strained p-channel Si<sub>0.50</sub>Ge<sub>0.50</sub> QWFETs with ultra-thin Si (~2 nm) cap layer, 1 nm EOT HfSiOx high- $\kappa$  dielectric/metal gate stack and 100 nm  $L_g$ . The noise improvement is demonstrated at high  $V_g$  due to the absence of parasitic surface channel formation in the Si cap layer resulting from 50% Ge concentration and minimal Ge out-

diffusion from low thermal budget processing [64]. The noise characteristics are comparable to Si near threshold due to the influence of the interface state density,  $D_{it}$ , which is maintained at acceptable level with 2nm Si cap layer.

$\text{Si}_{0.50}\text{Ge}_{0.50}$  p-channel QWFETs were fabricated at Sematech using a metal gate first CMOS flow [64]. A ~5 nm thick epitaxial  $\text{Si}_{0.50}\text{Ge}_{0.50}$  layer was pseudomorphically grown on Si substrate with a 2nm thick Si cap using ALD  $\text{HfSiO}_x$  dielectric. Millisecond annealing of source drain junctions was used to limit the thermal budget and suppress diffusion of Ge into Si substrate and gate stack [64]. Unstrained surface channel Si pMOSFETs were also fabricated as control samples to quantify the mobility and noise improvement.

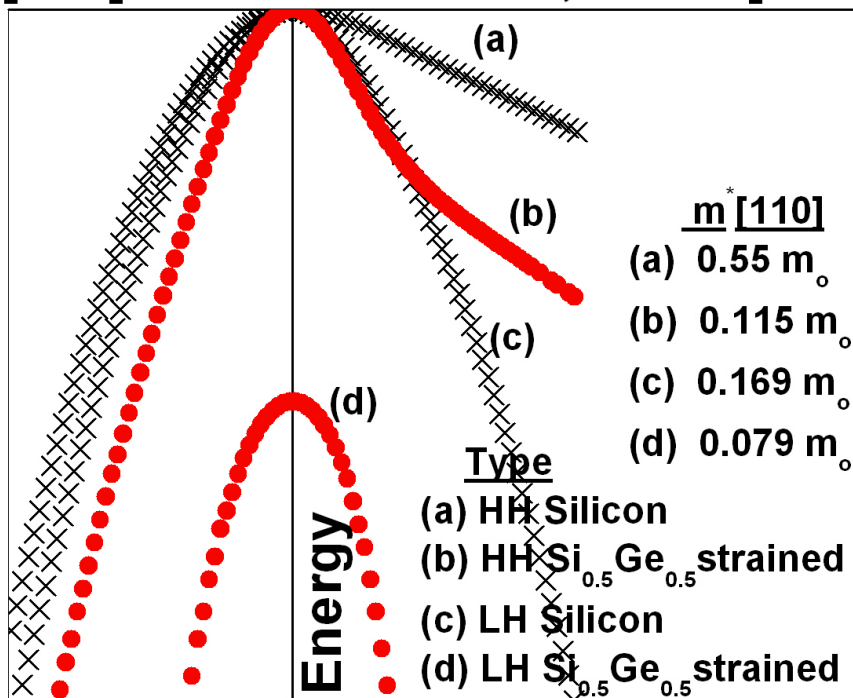
#### ***4.2.5.2 Flicker Noise Characteristics***

$\text{Si}_{0.50}\text{Ge}_{0.50}$  p-channel QWFETs were fabricated at Sematech using a metal gate first CMOS flow [64]. A ~5 nm thick epitaxial  $\text{Si}_{0.50}\text{Ge}_{0.50}$  layer was pseudomorphically grown on Si substrate with a 2nm thick Si cap using ALD  $\text{HfSiO}_x$  dielectric. Millisecond annealing of source drain junctions was used to limit the thermal budget and suppress diffusion of Ge into Si substrate and gate stack [64]. Unstrained surface channel Si pMOSFETs were also fabricated as control samples to quantify the mobility and noise improvement. Noise measurements were performed at room temperature on QWFETs and pMOSFETs with gate length and width of 100nm and 10  $\mu\text{m}$ , respectively, using SRS 570 low-noise preamplifier and HP35670A Dynamic Signal Analyzer. Figure 4-27 (a) shows the measured effective hole mobility in the  $\text{Si}_{0.50}\text{Ge}_{0.50}$  QWFET compared with the Si MOSFET as a function of the inversion hole density along with a schematic of the QWFET device structure. The hole mobility in strained  $\text{Si}_{0.50}\text{Ge}_{0.50}$  QWFETs improves by a factor of 2 (100%) compared to the Si control over a wide range of hole density. A six band k·p simulation predicts hole effective mass reduction by 5× from the strain induced warping of the heavy hole band along <110> direction. The lower than expected enhancement, at low field, is due to Coulomb scattering caused by higher  $D_{it}$  away from the valence band edge as shown by charge pumping measurements in Fig. 4-27 (c).

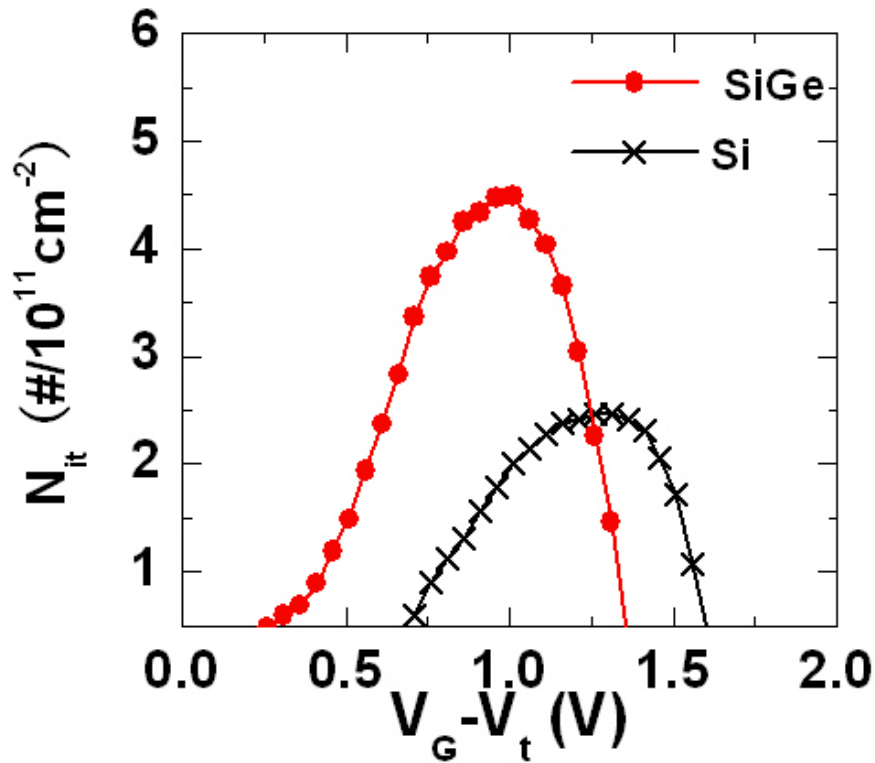


(a)

[100]-----Wave Vector,  $k$  -----[110]



(b)

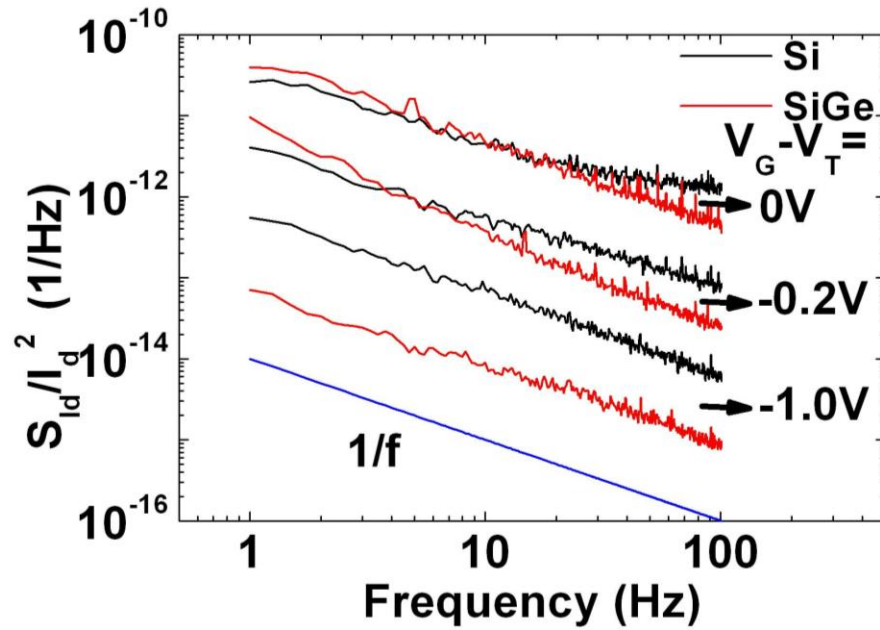


(c)

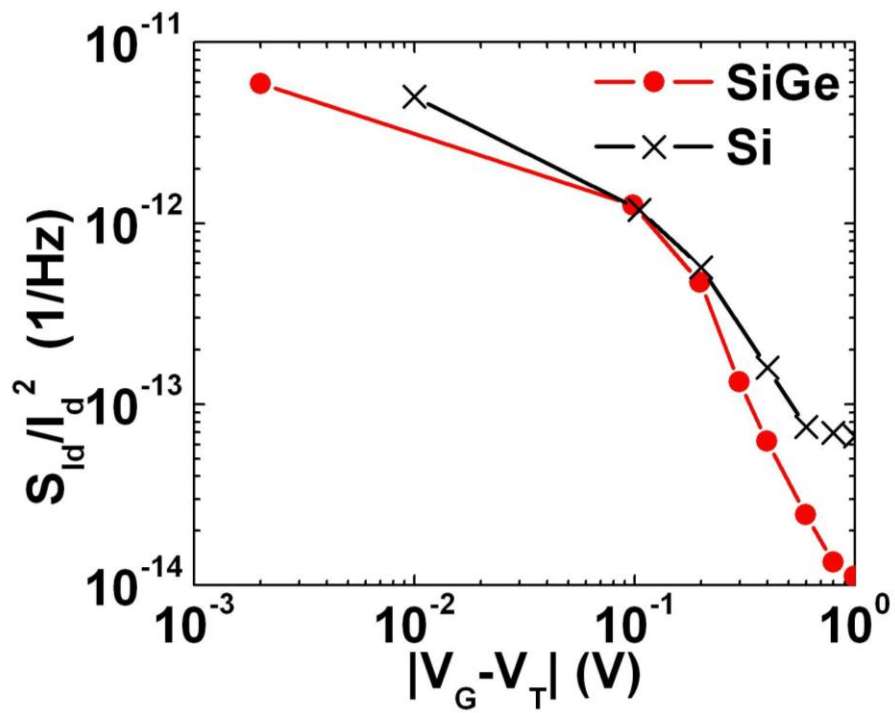
Figure 4-27. (a) Measured effective hole mobility as a function of hole density for p-channel  $\text{Si}_{0.50}\text{Ge}_{0.50}$  QWFETs and Si MOSFETs (b) Six band k-p simulation of heavy and light hole energy dispersion for strained  $\text{Si}_{0.50}\text{Ge}_{0.50}$  QW and unstrained silicon (c) Measured interface state profile via charge pumping measurements.

Figure 4-28 (a)-(b) show the measured room temperature normalized power spectral density ( $S_{I_d}/I_d^2$ ) of the drain current ( $I_d$ ) fluctuations in both the devices in linear region of operation as a function of gate overdrive. The strained  $\text{Si}_{0.50}\text{Ge}_{0.50}$  QWFETs show similar drain current noise spectral density at low gate overdrive but almost an order of magnitude reduction compared to the unstrained Si control devices, at the high gate overdrive of 1.0 V. The series resistance contribution to the total on-resistance is 33% and 20% for Si and  $\text{Si}_{0.50}\text{Ge}_{0.50}$  devices, respectively, at 100 nm  $L_g$ , thereby not playing a dominant role on noise characteristics even at high overdrive. This is confirmed in Fig. 4-28 (b), where both the devices show strong  $V_{gs}$  dependence, indicating

noise spectral density dominated by channel resistance except for very few last points for Si case when the noise spectral density flattens off showing series resistance effect.



(a)



(b)

Figure 4-28. Normalized power spectral density (NPSD) of  $I_d$  fluctuations ( $S_{I_d}/I_d^2$ ) in unstrained Si pMOSFETs and  $\text{Si}_{0.50}\text{Ge}_{0.50}$  strained QWFETs as a function of gate over drive voltage. The drain voltage is -50 mV. (b) NPSD of  $\text{Si}_{0.50}\text{Ge}_{0.50}$  strained QWFETs compared against Si pMOSFETs showing almost 10X improvement in noise spectral density at 10 Hz, especially at high gate voltage. The drain voltage is -50 mV.

Table 4-2 summarizes the normalized input referred noise spectral density,  $S_{V_G}$ , and the normalized output drain current noise spectral density,  $S_{I_d}/I_d^2$  as a function of i) Ge %, ii)  $\text{Si}_x\text{Ge}_{1-x}$  quantum-well thickness, iii) Si cap thickness, iv) dielectric, v) vertical electric field, and, finally, vi) the maximum thermal budget related to device processing. We conclude that the record flicker noise performance of our devices stems from a combination of high Ge concentration (50%) without strain relaxation, minimal Ge out-diffusion [64], the thinnest (2nm) possible silicon cap preventing parasitic channel formation at higher electric field and the lowest thermal budget processing attempted till date (enabled by source drain activation using millisecond flash anneal). We show that our own fabricated devices with higher Ge concentration (75%) processed with higher thermal budget results in higher noise current characteristics due to out-diffusion of Ge into the cap layer.

Table 4-2. NOISE BENCH MARK TABLE OF CURRENT Si/SiGe DEVICES

	Ge%	$t_{\text{SiGe}}$ (nm)	$t_{\text{SiCap}}$ (nm)	$t_{\text{ox}}$ (nm)	$E= V_g-V_{t1} /t_{\text{ox}}$ (V/cm)	S/D activation anneal	$S_{V_g} * L * W$ ( $\mu\text{m}^2 * \text{V}^2/\text{Hz}$ ) @10Hz	$S_{I_d}/I_d^2 * L$ *W ( $\mu\text{m}^2/\text{Hz}$ ) @10Hz
Si (this work)	N/A	N/A	N/A	2 (HfSiO <sub>x</sub> )	$5 \times 10^6$	1100C Flash Anneal	$6.02 \times 10^{-13}$	$6.66 \times 10^{-14}$
uniaxial strained Si [57]	25%	S/D	N/A	3.6 (HfSiO <sub>x</sub> )	$10^6$	1050C spike anneal	$1.5 \times 10^{-10}$	$3 \times 10^{-10}$
SiGe (this work)	50	5	2	2 (HfSiO <sub>x</sub> )	$5 \times 10^6$	1100C Flash Anneal	$2.3 \times 10^{-14}$	$1.12 \times 10^{-14}$
SiGe (this work)	75	3	3	2 (HfSiO <sub>x</sub> )	$5 \times 10^6$	RTA S/D Anneal 10s	$6.16 \times 10^{-14}$	$2.72 \times 10^{-14}$
SiGe[56]	20	20	7	170 (SiO <sub>2</sub> )	$0.2 \times 10^6$	750C 0.5h Anneal	$10^{-7}$	$10^{-9}$
SiGe[58]	20	20	4.7	7 (SiO <sub>2</sub> )	$10^6$	-	$2.03 \times 10^{-11}$	$3 \times 10^{-11}$
SiGe[60]	10	20	0	3 (SiO <sub>2</sub> )	$3.3 \times 10^6$	spike anneal 1050 C	-	$9.6 \times 10^{-9}$
SiGe[62]	25	-	10	(SiO <sub>2</sub> )	-	-	-	$10^{-12}$
SiGe[63]	20	-	0	5 (Al <sub>2</sub> O <sub>3</sub> )	$2 \times 10^6$	RTA Anneal 930C 10s	$10^{-9}$	$2 \times 10^{-10}$
SiGe[64]	30	-	5	3 (SiO <sub>2</sub> )	$3.3 \times 10^6$	-	-	$7 \times 10^{-11}$

### 4.2.5. 3 Noise Modeling

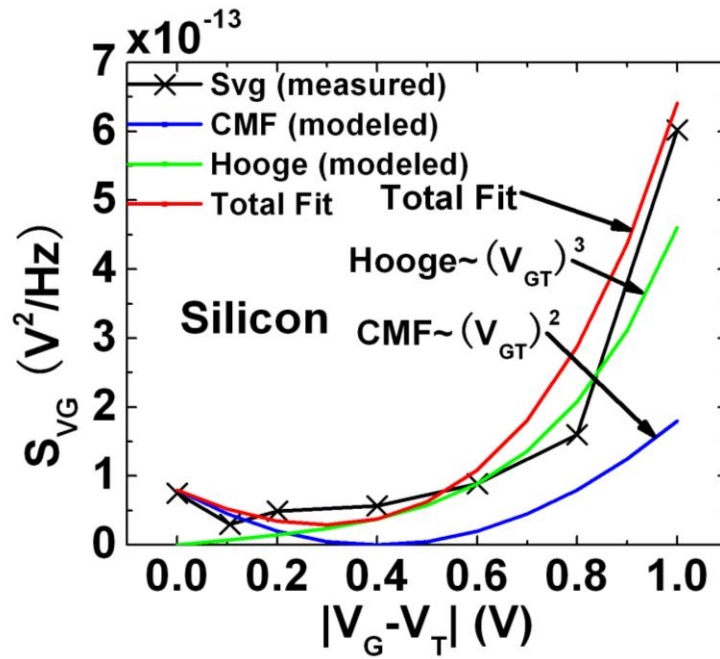
To understand the physical mechanisms determining the noise performance, we studied the evolution of the equivalent input gate voltage noise ( $S_{VG}$ ) as a function of the gate bias (Fig. 4-29) averaged over 5 devices. The input gate voltage noise caused by carrier number fluctuation (CNF) and mobility fluctuation correlated to number fluctuations (CMF) was modeled by:

$$S_{vg} = S_{vfb} [1 - \alpha \mu_0 C_{gate} (V_g - V_t)]^2$$

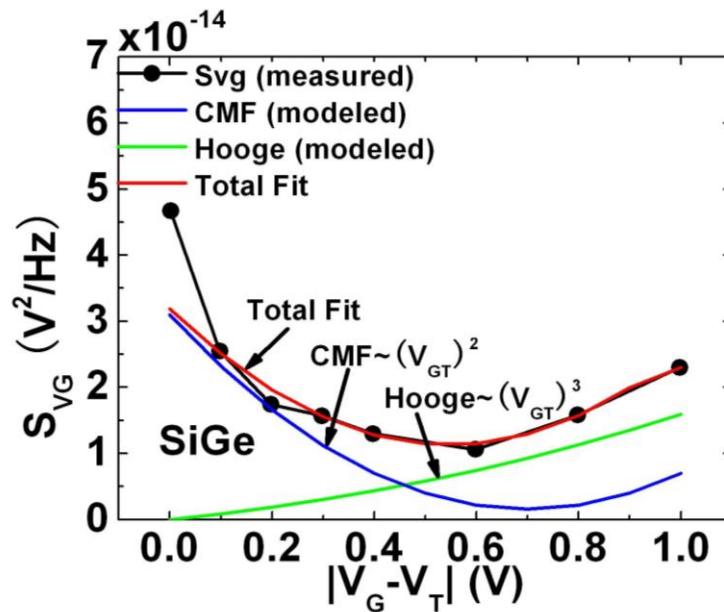
where  $S_{vfb} = 3.8 \times 10^{-14}$  ( $8 \times 10^{-14}$ )  $V^2 / \text{Hz}$ ,  $C_{gate} = 1.9$  (2.0)  $\mu\text{F}/\text{cm}^2$ ,  $\mu_0 = 153$  (64)  $\text{cm}^2\text{V}^{-1}\cdot\text{s}^{-1}$ ,  $\alpha = 4 \times 10^3$  ( $1.5 \times 10^4$ )  $\text{V}\cdot\text{s}\cdot\text{C}^{-1}$ , the Coulomb scattering parameter, are used for the strained  $\text{Si}_{0.50}\text{Ge}_{0.50}$  QWFETs (and Si pMOSFETs). The negative sign in front of the Coulomb scattering parameter indicates presence of acceptor traps which become neutral by trapping holes resulting in a negative correlation between the hole mobility and carrier fluctuation. At high gate bias, the input gate voltage noise is explained by Hooge mobility fluctuation:

$$S_{vg} = \frac{q \alpha_H}{W L f C_{gate}} (V_g - V_t) [1 + \theta_1 (V_g - V_t) + \theta_2 (V_g - V_t)^2]^2$$

where the Hooge parameter,  $\alpha_H = 10^{-8}$  ( $10^{-7}$ ) (Fig. 4-30 (b)) and the mobility attenuation coefficients,  $\theta_1 = 0.4621$ ,  $\theta_2 = 0$  ( $\theta_1 = 0.6$ ,  $\theta_2 = 2$ ) for  $\text{Si}_{0.50}\text{Ge}_{0.50}$  QWFETs (and Si pMOSFETs).



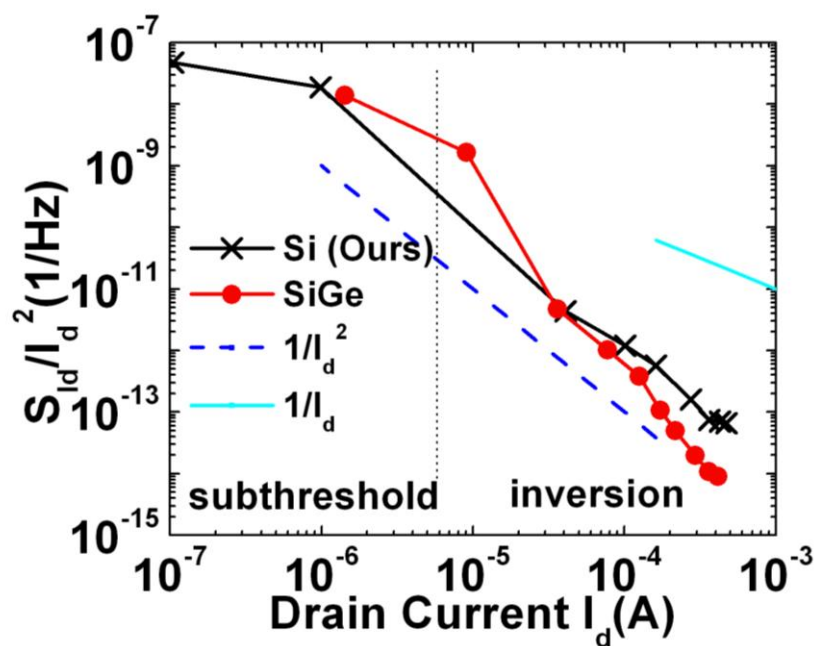
(a)



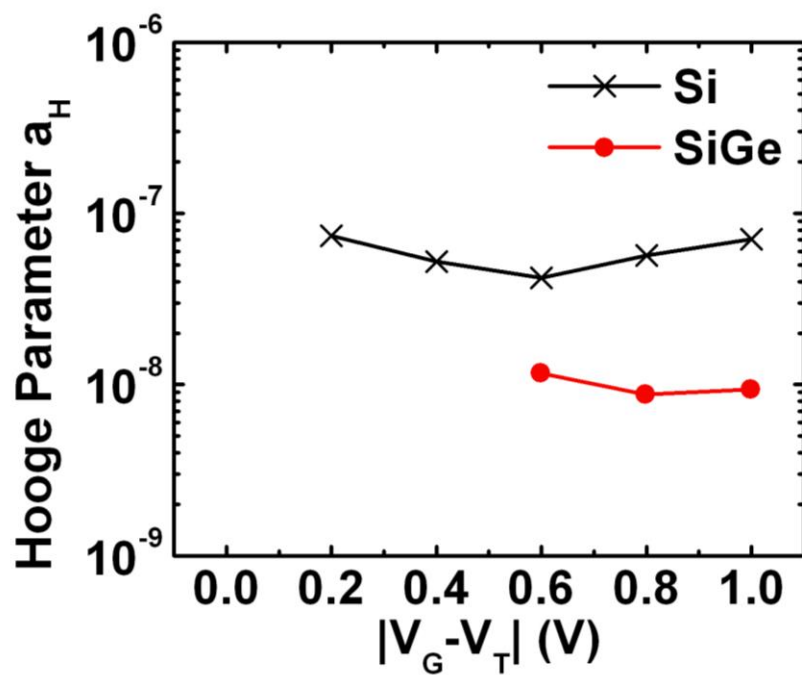
(b)

Figure 4-29. The equivalent input gate voltage noise characteristics,  $S_{VG} = S_{id}/g_m^2$  in (a) unstrained Si pMOSFETs and (b)  $Si_{0.50}Ge_{0.50}$  strained QWFETs as a function of gate over drive voltage. The drain voltage is -50 mV. The models used are correlated mobility fluctuation model (CMF) and Hooge mobility fluctuation model.

Our results show important differences between the strained  $\text{Si}_{0.50}\text{Ge}_{0.50}$  QWFETs and the surface channel Si pMOSFETs. The input gate noise in Si pMOSFETs is primarily determined by mobility-fluctuation-dominated mechanism. In strained  $\text{Si}_{0.50}\text{Ge}_{0.50}$  QWFETs, the input gate noise is reduced by an order of magnitude and limited by the correlated mobility fluctuation effect up to very high gate overdrive where the Hooge mobility fluctuation eventually dominates. Fig. 4-30 (a) plots the normalized drain current noise against the drain current for  $\text{Si}_{0.50}\text{Ge}_{0.50}$  QWFETs and Si MOSFETs from sub-threshold till strong inversion. Below threshold, for  $\text{Si}_{0.50}\text{Ge}_{0.50}$  QWFETs the carrier number fluctuation dominates due to interface traps present at the high- $\kappa$  and ultra-thin silicon interface whereas above threshold, the correlated mobility fluctuation dominates ( $\sim 1/I_d^2$ ). The Hooge mobility fluctuation becomes relevant at very high  $V_g$ , but the absolute value still remains low compared to the Si pMOSFETs (Fig. 4-30 (b)). This result is markedly different from Jiang et al [70], who reported degradation in the noise characteristics in their dual quantum well  $\text{Si}_{0.60}\text{Ge}_{0.40}$  devices at high  $V_g$  due to the formation of a parasitic surface channel in the Si layer. In our strained  $\text{Si}_{0.50}\text{Ge}_{0.50}$  QWFETs we prevent formation of parasitic surface channel in the Si layer at high  $V_g$  by a) aggressively scaling and preserving the top silicon barrier layer to less than 2 nm without sacrificing hole mobility b) by increasing the Ge mole fraction in the QW to 50% leading to better confinement of holes without any strain relaxation and c) by using millisecond flash anneal activation of dopants with no Ge out-diffusion as confirmed by EDX studies [64]. Previous attempt in integrating ultra-thin Si cap with strained SiGe or SiGeC quantum well resulted in degraded noise due to consumption of the Si cap during gate stack processing and disruption of the epi quality of the channel [71].



(a)



(b)

Figure 4-30. (a) The normalized drain noise characteristics,  $S_{I_d}/I_d^2$ , in  $\text{Si}_{0.50}\text{Ge}_{0.50}$  strained QWFETs and Si MOSFETs (ours and from Ref 73) (b) Extracted Hooge parameter as a function of gate overdrive voltage.

## Chapter 5 Front End Readout Circuit Design and Simulation

### 5.1 Signal Conditioning Circuit Design

The sensor model shown in Fig. 5-1 contains two equivalent modes, charge mode and voltage mode, so the corresponding readout circuit divides into two modes.  $C_p$  is the equivalent capacitance for piezoelectric layer and  $R_p$  accounts for the dissipation of static charge, which is usually very large. Charge mode readout circuit (Fig. 5-2 (a)) has been used when the sensor is remote from the circuit. The charge is transferred to the feedback capacitor  $C_f$  and this result in no stray capacitance effect, however, the  $C_f$  decides the low cut off frequency. The tradeoff between gain and bandwidth limits the performance of charge mode amplifier. Here,  $R_i$  is ESD protection and  $R_f$  bleeds out the charge preventing the output amplifier from being saturation. For voltage mode readout circuit (Fig. 5-2 (b)), the output is affected by the stray capacitor  $C_s$ , so usually sensor and circuit should be placed as close as possible.  $R_b$  is the biasing resistor which needs to be  $R_b \gg \frac{1}{\omega C} \parallel R_p$  in order to couple the input impedance.

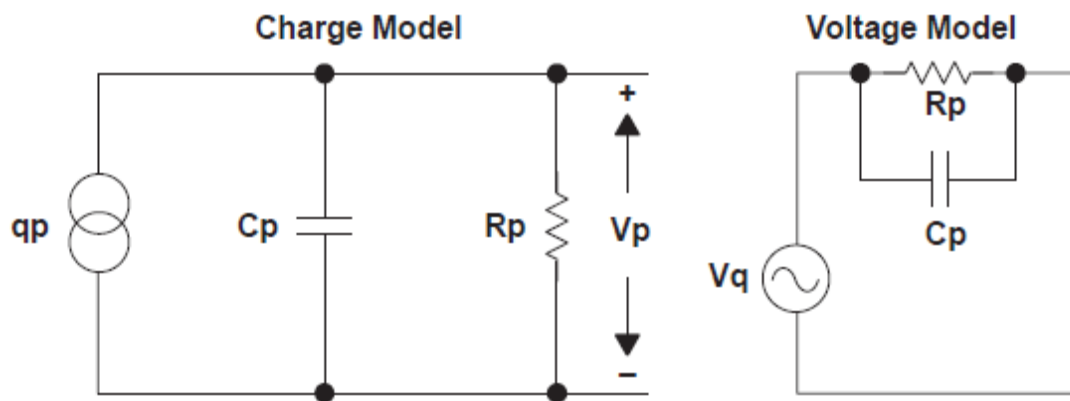


Figure 5-1. Two type of models for sensor: charge model and voltage model.

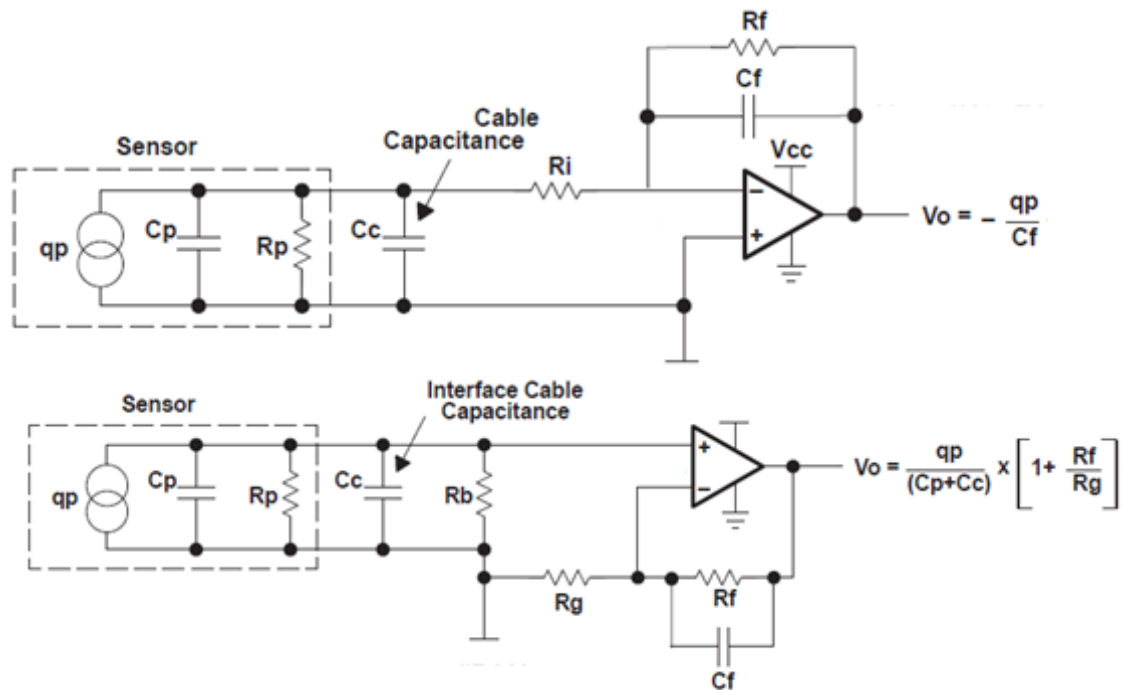


Figure 5-2. Circuit diagram for (a) charge mode and (b) voltage mode amplifier.

Figure 5-3 shows the comparison between different detection modes from ours and related work [53, 77]. We notice from the results that voltage mode amplifier has a good frequency response at low frequency and most charge amplifier suffers from the limitation of lower cutoff frequency.

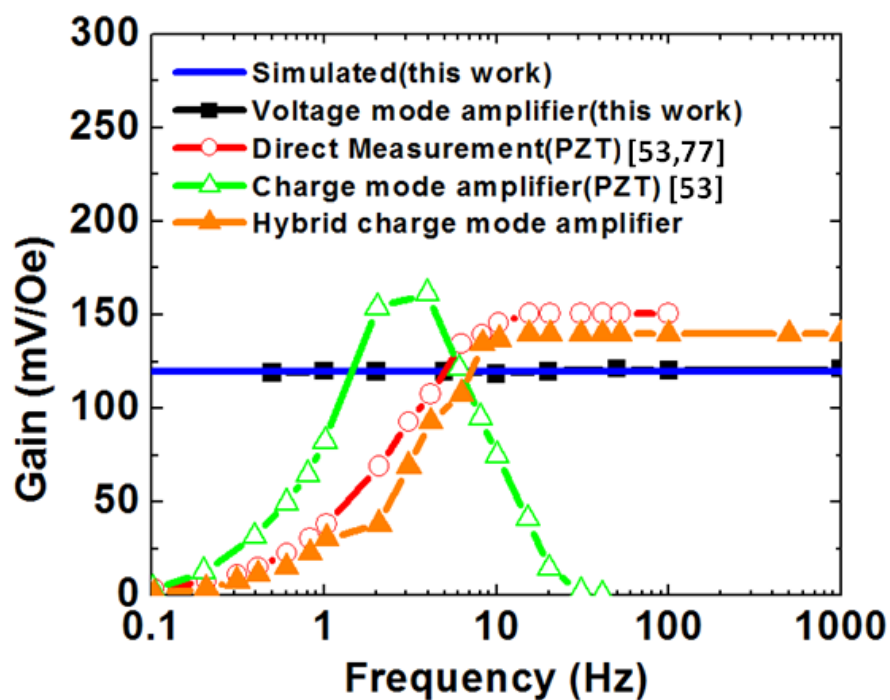


Figure 5-3. Frequency response comparisons for voltage mode and charge mode readout circuit.

## 5.2 Post Signal Processing Circuit

The signal-to-noise ratio (SNR) of this magnetic sensor system is defined as the input noise voltage over input referred noise voltage. For a linear system, SNR also equals to the output voltage over output noise voltage.

The output signal coming from the sensor output contains the low frequency components, usually below 100Hz for the human brain waves (Table 1-1). At such low frequency, the flicker noise is dominated in the readout circuit, so by modulating the output signal into high frequency is another efficient way to reduce the noise level and improve the sensitivity. Fig. 5-4 shows the block diagram form the signal processing circuit. The front-end readout circuit couples the signal from the sensor and amplifies it. Usually, sensing the low level of magnetic field below nano Tesla, the sensor output can reach only micro voltage level and can be suppressed by the environmental noise, so the front-end stage provide a high gain and high CMRR in order to raise the output level and eliminate the common mode noise, especially 60 Hz harmonics close to the frequency band of human brain. Then output signal from the front end stage goes to an analog lock in amplifier which will perform both amplification and modulation. With the band pass filter windowing the band of human brain signal, the total SNR can be improved by 30 times in comparison to the one without signal modulation. The demodulation mixer and low pass filter (LPF) filter out useless information at high frequency and recover the original signal.

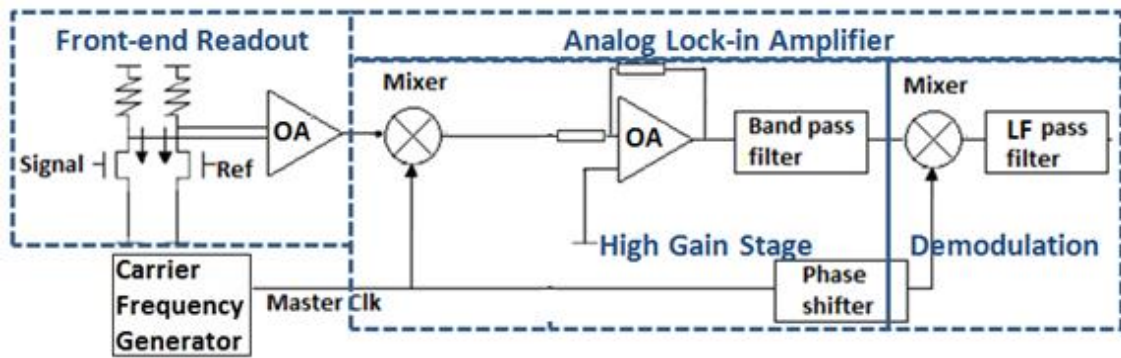


Figure 5-4. Schematic of post signal processing circuit for ME sensor.

### 5.2.1 Front End Operational Amplifier Design

The front-end differential readout stage consists of the voltage mode readout circuit, and a folded cascade operational amplifier (OA). The reference signal can be generated by placing the sensor in free space. In this case, both the reference and sensing signal contains the common mode signal from the environment. The output from the readout circuit goes to a folded cascade differential amplifier (Fig. 5-5) which shows a high gain ( $\sim 85\text{dB}$ ) and high common mode rejection ratio (CMRR $\sim 115\text{dB}$ ), as shown in Fig. 5-6. This highly reduces the common mode noise from the input especially the 60Hz power noise.

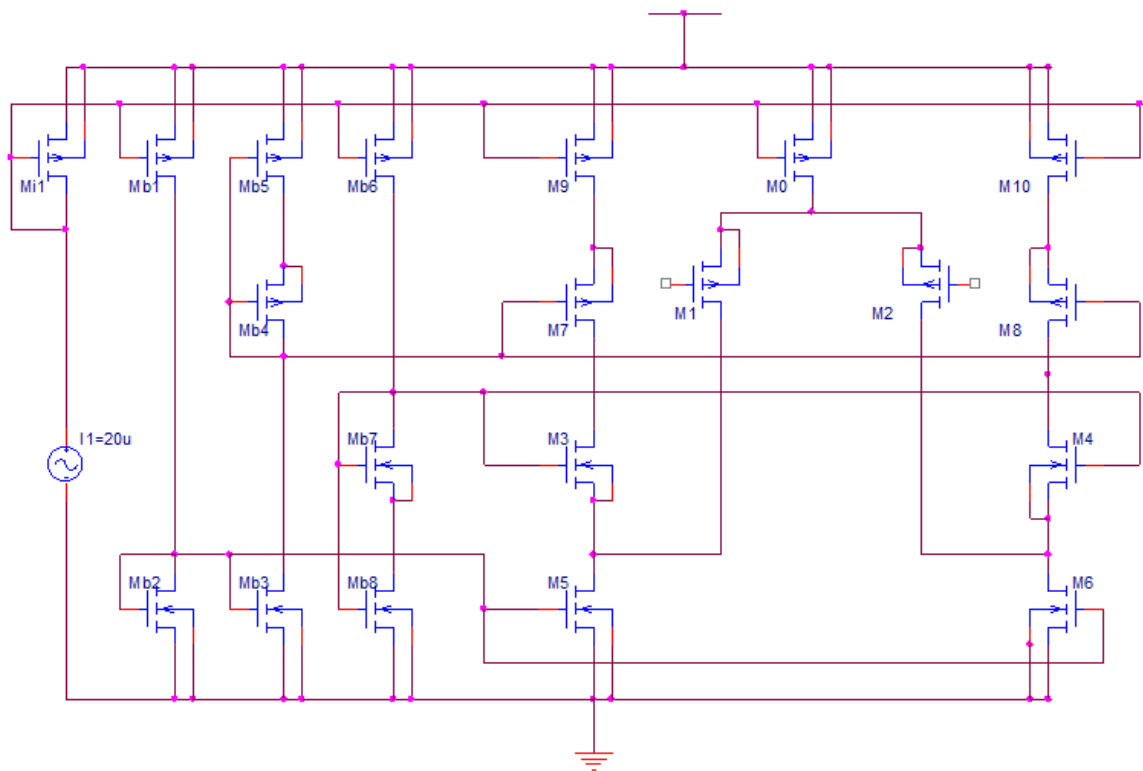
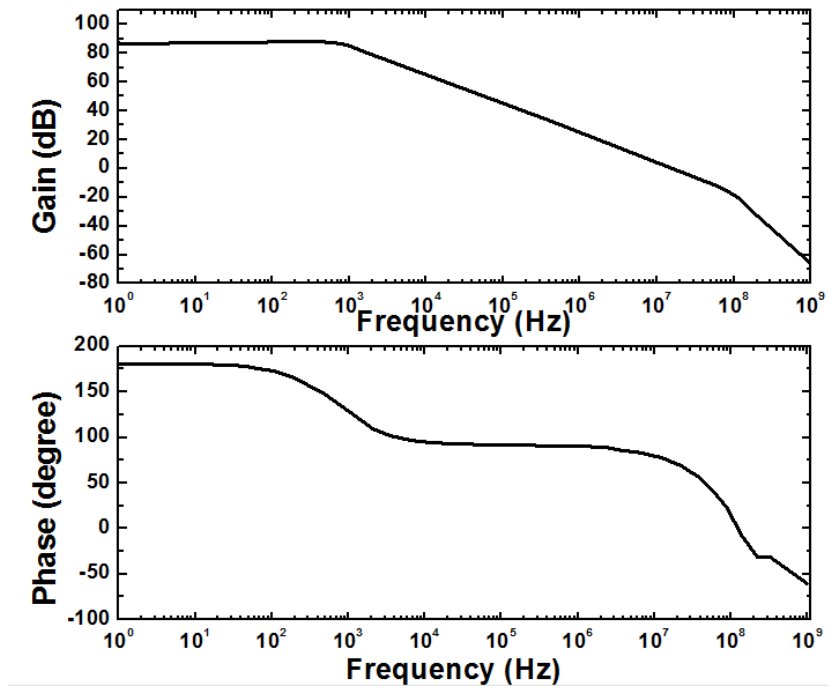
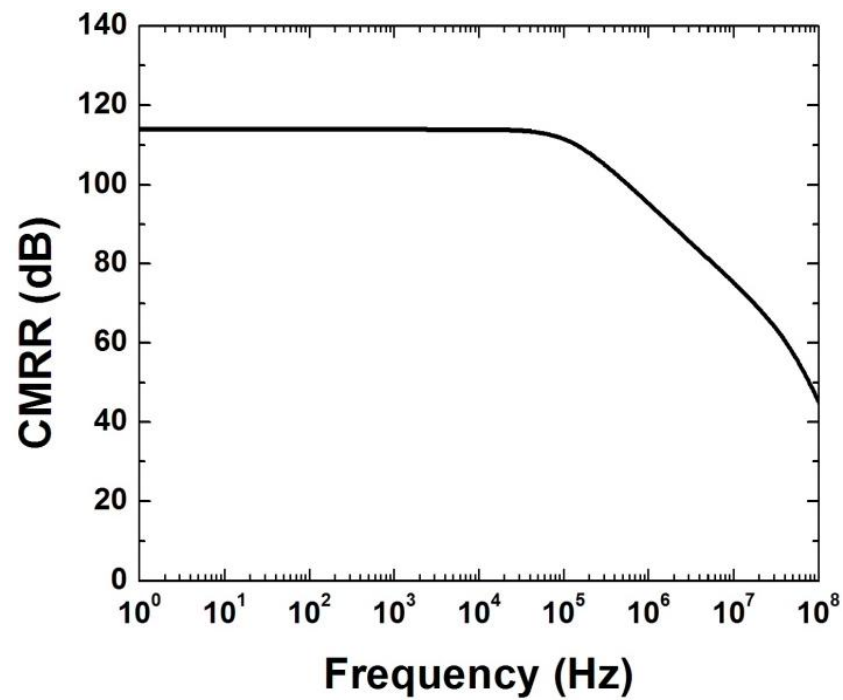


Figure 5-5. Circuit diagram for the operation amplifier with biasing circuit.



(a)



(b)

Figure 5-6. Frequency response (a) and CMRR (b) for the operation amplifier.

Figure 5-7 shows the generated alpha waves (typically 8~12Hz) with the 60Hz harmonics from the input and a clear OA output signal in which the 60Hz harmonics get suppressed significantly. The frequency spectrum is also examined in Fig. 5-7, that the 60Hz common mode noise has been highly rejected.

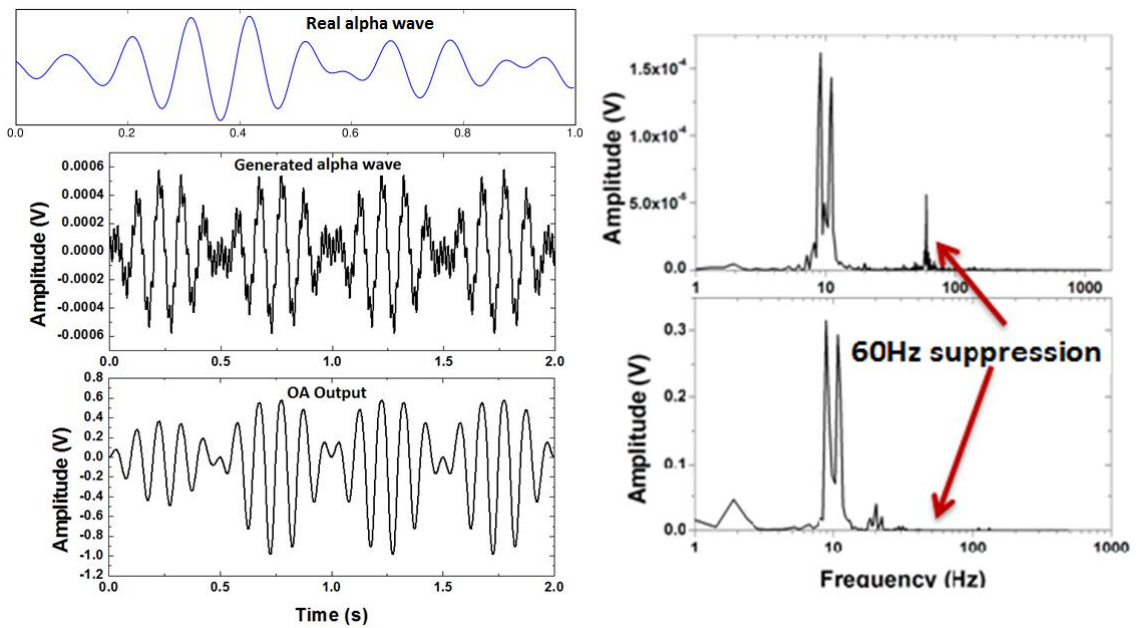


Figure 5-7. Real time signal and frequency spectrum of Alpha waves from OA input and output.

### 5.2.2 On-chip Lock in Amplifier

The principle of the carrier wave modulation (usually called amplitude modulation (AM)) can be expressed as

$$\begin{aligned}v_s(t) &= V_s \cos(\omega_s t) \\v_c(t) &= V_c \cos(\omega_c t) \\v_o(t) &= v_s(t) * v_c(t) = \frac{1}{2} V_s V_c [\cos(\omega_c - \omega_s)t + \cos(\omega_c + \omega_s)t]\end{aligned}$$

where  $v_s(t)$  is the signal,  $v_c(t)$  is the carrier wave, and  $v_o(t)$  is the output from mixer.

The demodulation principle is the same as the modulation, which we use the same carrier wave to modulate the signal coming from the mixer.

$$\begin{aligned}v_i(t) &= K[\cos(\omega_c - \omega_s)t + \cos(\omega_c + \omega_s)t] \\v_c(t) &= V_c \cos(\omega_c t + \phi) \\v_o(t) &= K \{ \cos(-\omega_s t - \phi) + \cos[(2\omega_c - \omega_s)t + \phi] + \cos(\omega_s t - \phi) + \cos[(2\omega_c + \omega_s)t + \phi] \}\end{aligned}$$

Then we use a low pass filter (LPF) to eliminate the high frequency components and leave only low frequency components which contain the brain wave information. Then the total output from the low pass filter is shown

$$v(t) = K'' \cos \omega_s t \cdot \cos \phi$$

This shows the original brain wave signal can be recovered by a factor of  $K \cos \phi$ . However, if  $\phi$  is not choosing properly, we may get a very weak output response. For example, if  $\phi = 90^\circ$ , the output has no response to the input signal. By maximizing the output voltage, we need  $\phi = 0$ , so a phase shifter is needed for this analog lock in amplifier.

The total design is simulated using IMEC 65 nm technology process. The output waveform of each block is shown in Fig. 5-8 and Fig. 5-9.

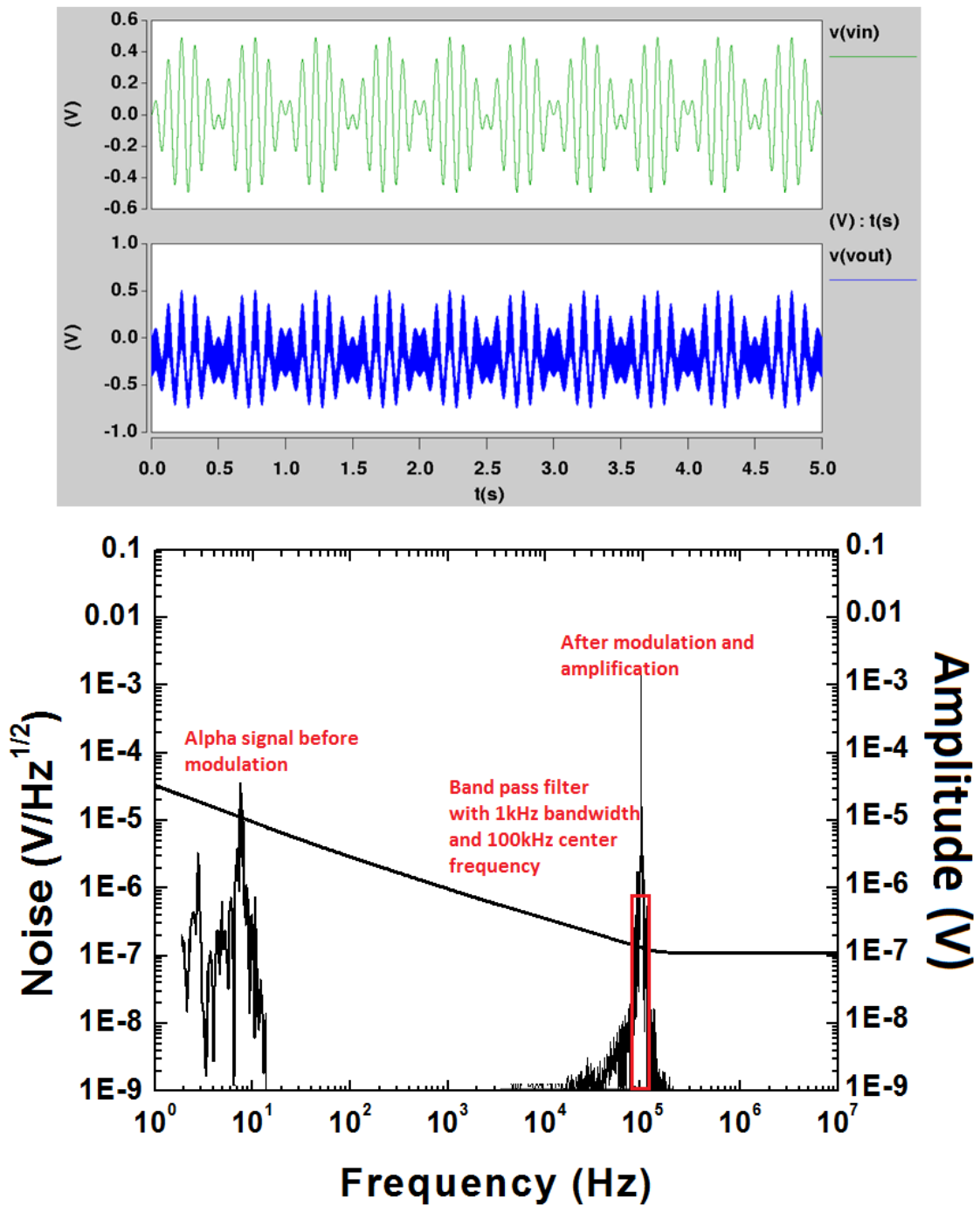


Figure 5-8. Real time output and frequency spectrum of Alpha waves after modulation.

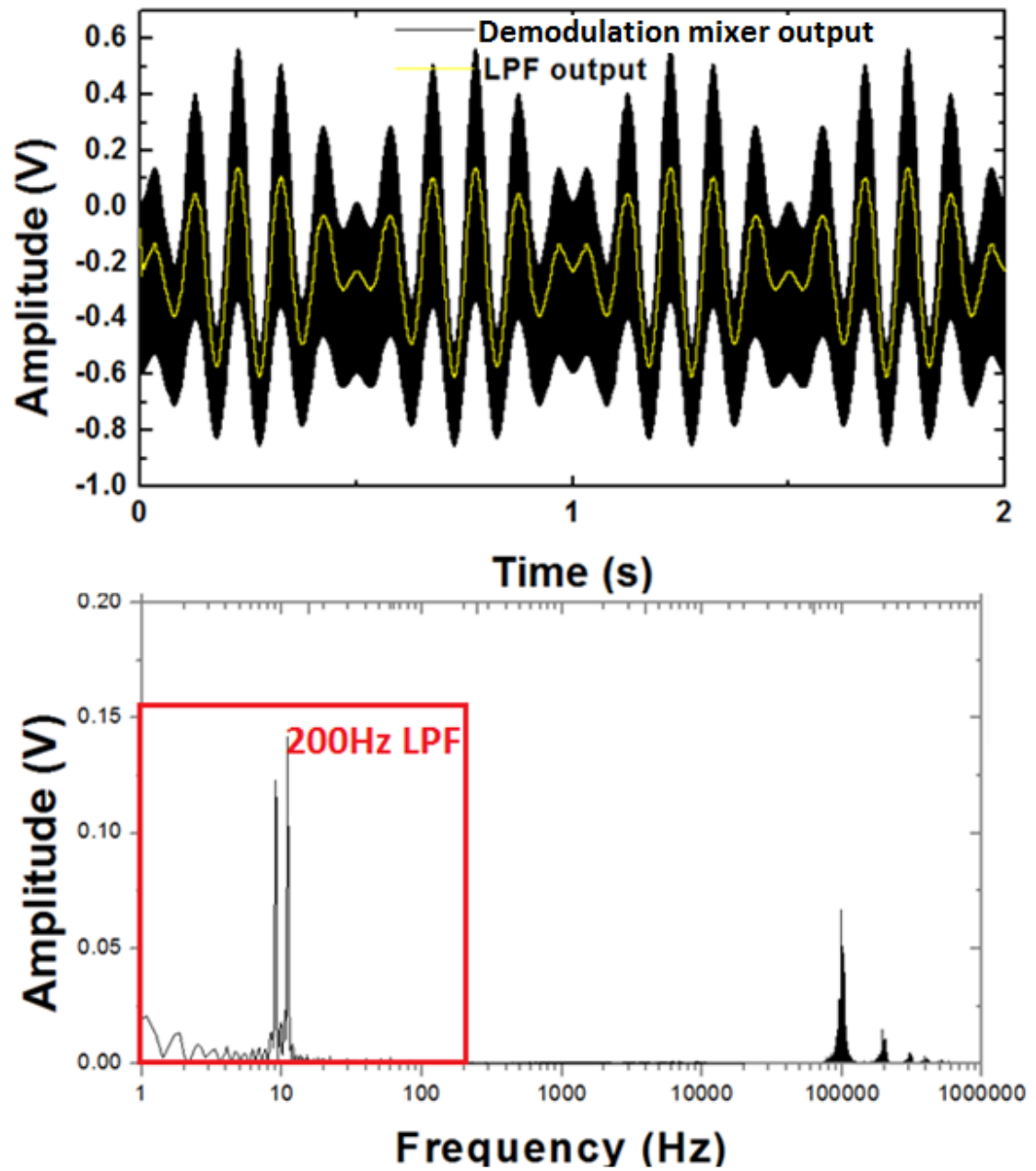


Figure 5-9. Real time output and frequency spectrum of Alpha waves after demodulation.

## Chapter 6 Conclusions and Future Work

### 6.1 Conclusion

The main goal of this research has been to design and fabricate the next generation magnetic sensors for future ultra-low power and high performance biomedical imaging applications. In this regard, the concept of magnetoelectric laminates sensors is introduced in chapter 1. In chapter 2, several signal improvement methods for bulky ME laminates sensor are presented. The needs for sensor arrays and portable devices require the integrated magnetoelectric sensors. Further the strategy for thin film magnetostrictive selection and in-situ magnetization deposition in chapter 3 brings the significant benefits to low power and high sensitivity sensors. Also, the vector sensing of ME sensors results from the unique directional property.

Complete fabrication of Metglas<sup>®</sup>/PZT ME laminate cantilever sensors along with its characterization is explained in the first part of chapter 4. From the sensitivity and noise analysis, the identification of two different knobs can be used to improve the device performance: (i) reduce load for magnetostrictive thin films (ii) dielectric noise reduction. Considering the low sensitivity of the first type of integration, a novel concept of magnetoelectric flexural gate transistors (MEFGT) is also presented in chapter 4. Both optical behavior and electrical performance of MEFGT is studied in great detail. The device shows the highest sensitivity of the integrated ME sensors till date. Also, it is clearly shown that MEFGT inherently suffers from residue stress of the microcantilever gate and the transistor flicker noise. The analytical and simulation results for the flexural gate capacitance give the key insight into MEFGTs operating

principle. Noise performance of MEFGTs is addressed in following section with modeling of different types of noise sources. The flicker noise of the readout transistor is the limiting factor of the entire system noise. Discussions on advanced buried channel devices, SiGe quantum well transistors, show the improvement in the low frequency flicker noise. More details on the sensitivity and resolution enhancement of MEFGTs will be discussed in the following sections. A newly designed inplane mode detection MEFGTs will bring the solution to the residue stress issue and result in a higher sensitivity than the out of plan detection MEFGTs.

In chapter 5, We have studied the signal conditional circuits for the sensor readout circuits. Post signal processing circuits including amplifier and modulation are simulated with the incident real time brain signal. In future, moving towards the direct integration of MEFGTs and signal processing circuits will result in the realization of portable magnetometers.

To summarize, we compare the resolution of different type of ME sensor in Table 6-1. The integrated ME sensor, MEFGT, shows a great improvement in the resolution both at low frequency and at resonance. Figure 6-1 presents the sensitivity comparison between MEFGT and other type of magnetic sensing techniques at 1Hz. The MEFGT is comparable to the magnetoresistor and has the potential to challenge the flux gate magnetic sensors to achieve picoTesla minimum detectable field (MDF) sensing capability.

Table 6-1. Resolution Comparison

Type	at resonance (nT/ $\sqrt{\text{Hz}}$ )	At 1Hz (nT/ $\sqrt{\text{Hz}}$ )
<i>Bulk ME sensor</i>	0.02	0.9
<i>ME cantilever sensor</i>	100	24000
<i>MEFGT</i>	0.15	60

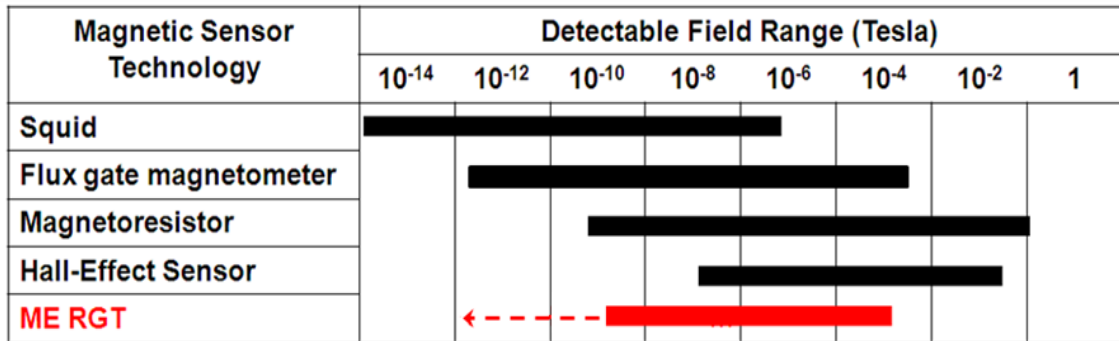


Figure 6-1. MEFGT sensitivity benchmarked with current magnetic sensing technologies.

## 6.2 MEFGT Sensitivity Improvement

By reducing the effective air gap via better stress mismatch control of the two constituent layers (Ti and Metglas<sup>®</sup>) of the suspended flexural gate, the sensitivity can be further improved, as shown in Fig. 6-2. These considerations suggest the strong potential of the next generation MEFGT in achieving pico Tesla detection.

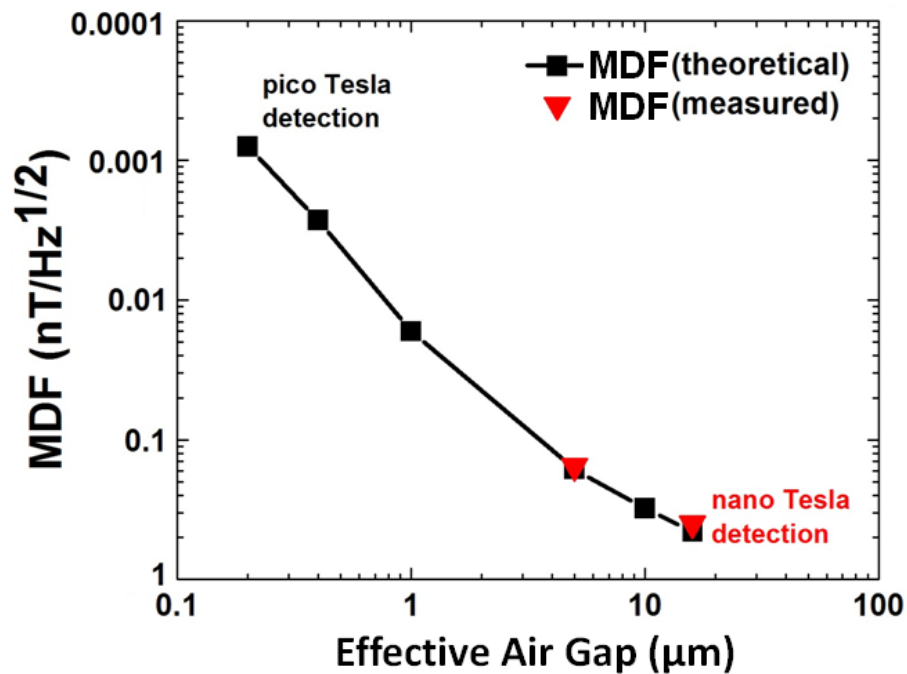
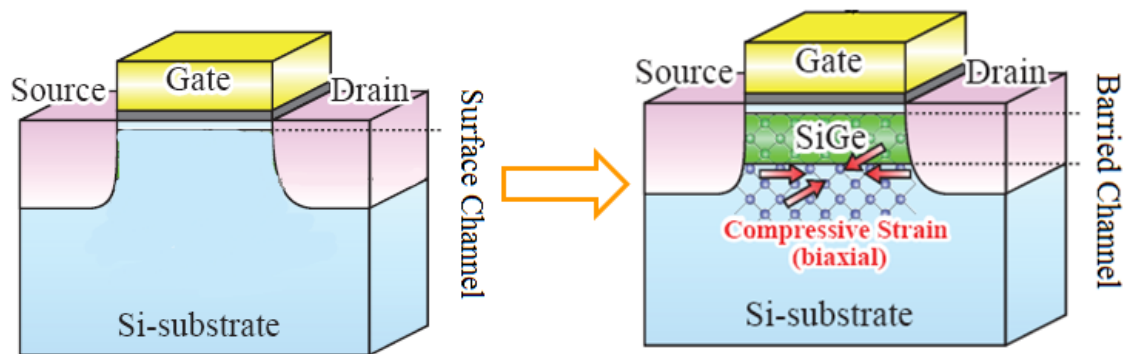


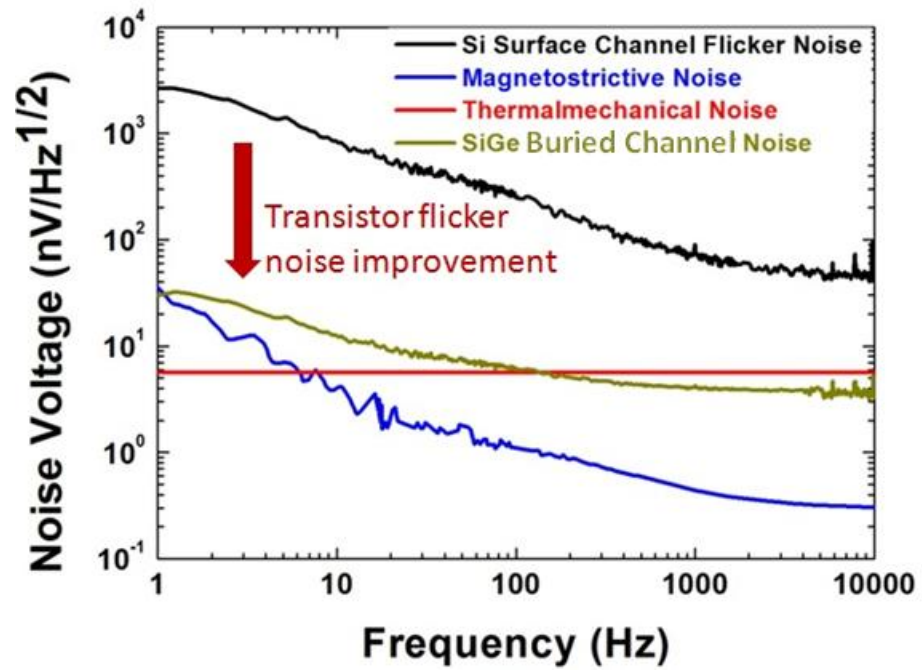
Figure 6-2. SNR as a function of effective air gap. The MEFGT shows the potential to achieve pico Tesla minimum AC magnetic field detection capability.

Knowing that the MEFGT noise performance is limited by the sensing transistors, we will introduce more advanced field effect transistors (FETs) with low flicker noise as a candidate to replace the noisy silicon surface channel transistors. A  $\text{Si}_{0.5}\text{Ge}_{0.5}$  buried channel quantum well

FET is characterized with record low flicker noise density (Fig. 6-3 (a)). The ultra thin film Si cap layer preserves SiGe quantum well channel from the high-k gate dielectric. The strong hole quantum well confinement provides a low interface scattering and results in a low flicker noise density. Comparing to the Si surface channel FETs, an improvement of 100× in the output noise voltage has achieved, as shown in Fig. 6-3 (b). The intrinsic sensor noise, including thermalmechanical noise and magnetostrictive noise, is also considered. A below 1 nV/ $\sqrt{\text{Hz}}$  is expected with SiGe quantum well FETs. This, in conjunction with the in-plane mode detection MEFGT, will lead to a picoTesla magnetic field detection sensitivity for the bioimaging applications.



(a)



(b)

Figure 6-3. SiGe buried channel transistor as a candidate for low noise application (a) schematic of Si surface channel FETs and SiGe quantum well FETs. (b) Flicker noise improvement.

### 6.3 In-plane Magnetolectric Flexural gate Transistors:

Targeting the bending issue of the laminates micromechanical cantilevers, novel in-plane mode detection MEFGT is investigated and the principle of operation is illustrated in Fig. 6-4. A single layer magnetostrictive (MS) thin film flexural gate replaces the multilayer cantilever which eliminates the bending issue. This also reduces the complexity in process fabrication. Moreover, the in-plane motion will overcome the electrostatic force problem during the displacement sensing. The incident magnetic field generates a strain in the MS film and a micron strain gauge will be introduced to amplify the strain. The corresponding in-plane displacement in the flexural gate will result in the change in the air capacitance. Similar capacitance sensing is accomplished by the transistor underneath. The analytical modeling of the strain gauge amplifier is presented in Fig. 6-5 (a). The sensing beam stresses in response to the input magnetic field and this results in a small displacement  $\delta_{tb}$  in the transfer beam. The resistant moment  $M_{sb} (= F_{sb}L_{tb})$  causes the angle change ( $\theta_{ab}$ ) in the amplify beam and large displacement in the flexural gate ( $L_{ab}$ ) is magnified through the mechanical amplification. The angle of deflection at the center of the transfer beam can be represented by

$$\theta_{tb} \approx \tan(\theta_{tb}) = \alpha (3\delta_{sb}) / (2L_{tb})$$

where  $L_{tb}$  is the length of the transfer beam and  $\alpha$  is the correction factor due to the presence of the amplifier beam. The value of  $\alpha$  can be optimized close to 1 with proper design (width of amplify beam is much smaller than the transfer beam length). The total flexural gate displacement  $\delta_{ab}$  can be expressed as

$$\delta_{ab} \approx L_{ab} \theta_{tb} = \alpha (3L_{ab}) / (2L_{tb}) \delta_{sb}$$

If we design  $L_{tb} = 20 \mu\text{m}$ ,  $L_{ab} = L_{sb} = 400 \mu\text{m}$ , a displacement of  $1.2 \mu\text{m}$  in the flexural gate will be achieved with only 0.01% of strain. Further, interdigitated electrode (IDE) design will increase the capacitance change due to the flexural gate displacement (Fig.7-4 (b)).

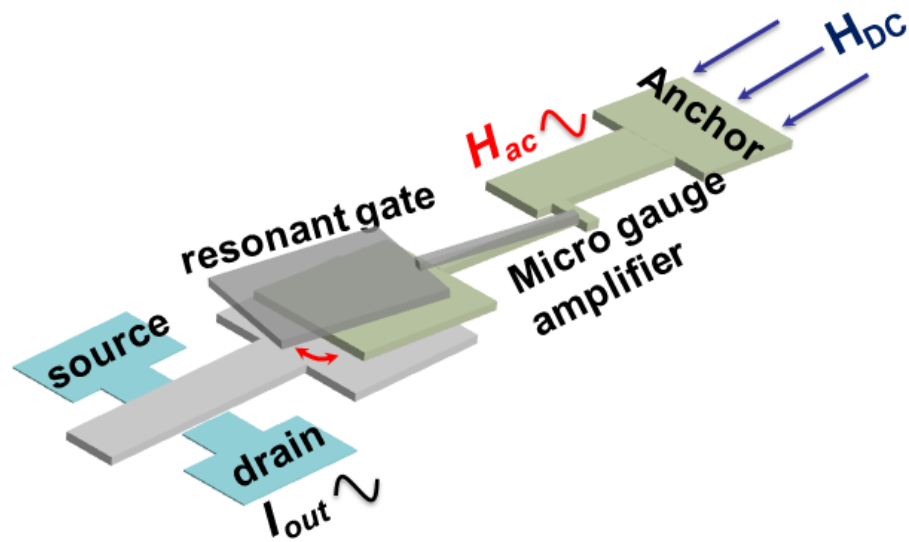
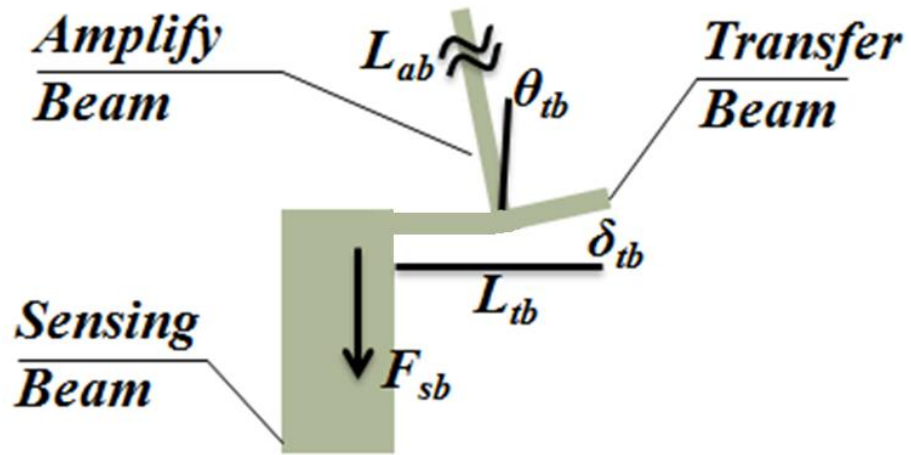
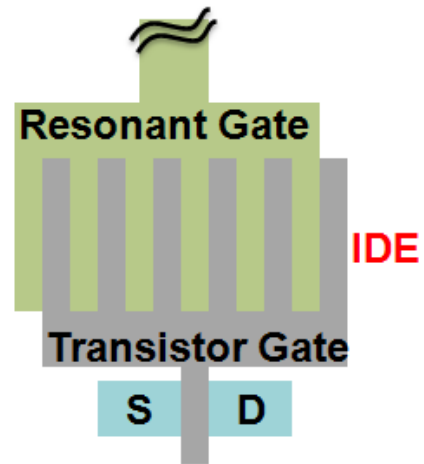


Figure 6-4. The principle of operation of an in-plane ME RGT.



(a)



(b)

Figure 6-5. (a) Micron strain gauge analytical modeling. (b) Interdigitated electrode (IDE) gate design.

## Reference

- [1] J. Lenz, and A. S. Edelstein, "Magnetic Sensors and Their Applications, " *IEEE Sensors Journal*, vol. 6, no.3, pp. 631, 2006
- [2] P. Ripka, "Magnetic Sensors and Magnetometers, " Artech House, Norwood, MA, 2001.
- [3] R. S. Popovic, Hall Effect Devices. Bristol, U.K.: Inst. Physics, 2004.
- [4] G. T. Rado and V. J. Folen, "Observation of the Magnetically Induced Magnetoelectric Effect and Evidence for Antiferromagnetic Domains," *Physical Review Letters*, vol.7, pp. 310, 1961.
- [5] M. Fiebig, "Revival of the magnetoelectric effect," *Journal of Physics D: Applied Physics*, vol. 38, pp. 123, 2005.
- [6] C. W. Nan, M. I. Bichurin, S. X. Dong, D. Viehland, and G. Srinivasan, "Multiferroic magnetoelectric composites: Historical perspective, status, and future directions," *Journal of Applied Physics*, vol. 103, 031101, 2008.
- [7] S. X. Dong, J. F. Li, and D. Viehland, "Characterization of magnetoelectric laminate composites operated in longitudinal-transverse and transverse-transverse modes," *Journal of Applied Physics*, vol. 95, 2625, 2004.
- [8] K. Mori and M. Wuttig, "Magnetoelectric coupling in Terfenol-D/polyvinylidenedifluoride composites," *Applied Physics Letters*, vol. 81, 100, 2002.
- [9] S. S. Guo, S. G. Lu, Z. Xu, X. Z. Zhao, and S. W. Or, "Enhanced magnetoelectric effect in Terfenol-D and flextensional cymbal laminates," *Applied Physics Letters*, vol. 88, 182906 2006.

- [10] J. Zhai, Z. Xing, S. Dong, J. Li, and D. Viehland, "Magneto-electric Laminate Composites: An Overview," *Journal of American Ceramics Society*, vol. 91, no. 2, pp. 351-358, 2008.
- [11] J. Ryu, A. V. Carazo, K. Uchino, and H.-E. Kim, "Magnetolectric Properties in Piezoelectric and Magnetostrictive Laminate Composites," *Japanese Journal of Applied Physics*, vol. 40, no.8, 2001.
- [12] M. I. Bichurin, V. M. Petrov, and G. Srinivasan (2002), "Theory of low-frequency magnetolectric effects in ferromagnetic-ferroelectric layered composites," *Journal of Applied Physics*, vol. 92, no. 12, pp. 7681-7683, 2002.
- [13] S. Dong, J. Cheng, J. F. Li, and D. Viehland, "Enhanced magnetolectric effects in laminate composites of Terfenol-D/Pb(Zr,Ti)O<sub>3</sub> under resonant drive," *Applied Physics Letters*, vol. 83, no. 23, pp. 4812-4814, 2003.
- [14] S. Dong, J. Li, and D. Viehland, "Longitudinal and Transverse Magnetolectric Voltage Coefficients of Megnetostrictive/Piezoelectric Laminate Composite: Theory," *IEEE Transaction Ultrasonics, Ferroelectrics and Frequency Control*, vol. 50 no. 10, pp. 1253-1261, 2003
- [15] M. I. Bichurin, V. M. Petrov, and G. Srinivasan, "Theory of low-frequency magnetolectric coupling in magnetostrictive-piezoelectric bi-layers," *Physics Review B*, vol. 68, no. 13, pp. 054402-054402-13, 2003.
- [16] S. Dong, J. Li, and D. Viehland, "Longitudinal and Transverse Magnetolectric Voltage Coefficients of Megnetostrictive/Piezoelectric Laminate Composite: Experiments," *IEEE Transaction Ultrasonics, Ferroelectrics and Frequency Control*, vol. 51, no. 7, pp. 793-798, 2004.
- [17] J. Zhai, N. Cai, Z. Shi, Y. Lin, and C.-W. Nan, "Coupled magnetodielectric properties of laminated PbZr<sub>0.53</sub>Ti<sub>0.47</sub>O<sub>3</sub>/NiFe<sub>2</sub>O<sub>4</sub> ceramics," *Journal of Applied Physics*, vol. 95, no. 10, pp. 5685-5690, 2004.

- [18] S. Dong, J. Zhai, F. Bai, J. Li, D. Viehland, and T. A. Lograsso, "Magnetostrictive and magnetoelectric behavior of FeGa/Pb(Zr,Ti)O<sub>3</sub> laminates," *Journal of Applied Physics*, vol. 97, no. 10, pp. 103902-103902-6, 2005.
- [19] C. W. Nan, N. Cai, Z. Shi, J. Zhai, G. Liu, and Y. Lin, "Large magnetoelectric response in multiferroic polymer-based composites," *Physics Review B*, vol. 71, no.5, pp. 014102-014102-5, 2005.
- [20] S. Dong, J. Zhai, F. Bai, J.-F. Li, and D. Viehland, "Push-pull mode magnetostrictive/piezoelectric laminate composite with an enhanced magnetoelectric voltage coefficient," *Applied Physics Letters*, vol. 87, no. 6, pp. 062502-062502-3, 2005.
- [21] J. Zhai, Z. Xing, S. Dong, J. Li, and D. Viehland, "Thermal noise cancellation in symmetric magnetoelectric bimorph laminates," *Applied Physics Letters*, vol. 93, no. 7, pp. 072906-072906-3, 2008.
- [22] Z. Xing, J. Zhai, J. Li, and D. Viehland, "Investigation of external noise and its rejection in magnetoelectric sensor design," *Journal of Applied Physics*, pp.106, no. 2, pp. 024512-024512-7, 2009.
- [23] F. Fang, S. C. Shan, and W. Yang, "A multipeak phenomenon of magnetoelectric coupling in Terfenol-D/P(VDF-TrFE)/Terfenol-D laminates," *Journal of Applied Physics*, vol. 108, no. 10, pp. 104505-104505-5, 2010.
- [24] N. Cai, J. Zhai, C.-W. Nan, Y. Lin, and Z. Shi, "Dielectric, ferroelectric, magnetic, and magnetoelectric properties of multiferroic laminated composites," *Physics Review B*, vol. 68, no. 7, pp. 224103-224103-7, 2003.
- [25] <http://www.comsol.com/>.
- [26] C. P. Zhao, F. Fang, and W. Yang, "A dual-peak phenomenon of magnetoelectric coupling in laminated Terfenol-D/PZT/Terfenol-D composites," *Smart Materials and Structures*, vol. 19, no. 12, pp. 125004-125004-7, 2010.

- [27] J. Zhai, S. Dong, Z. P. Xing, J. Gao, J. F. Li, and D. Viehland, "Tunable magnetoelectric resonance devices," *Journal of Physics D: Applied Physics*, vol. 42, no. 12, pp. 122001-122001-3, 2009.
- [28] Z. Xing, S. Dong, J. Zhai, L. Yan, J. Li, and D. Viehland, "Resonant bending mode of Terfenol-D/steel/Pb(Zr,Ti)O<sub>3</sub> magnetoelectric laminate composites," *Applied Physics Letters*, vol. 89, no. 11, pp. 112911-112911-3, 2006.
- [29] J. G. Wan, Z. Y. Li, Y. Wang, M. Zeng, G. H. Wang, and J. M. Liu, "Strong flexural resonant magnetoelectric effect in Terfenol-D/epoxy-Pb(Zr,Ti)O<sub>3</sub> bilayer," *Applied Physics Letters*, vol. 86, no. 20, pp. 202504-202504-3, 2005.
- [30] Z. Fang, S. G. Lu, F. Li, S. Datta, and Q. M. Zhang, "Enhancing the magnetoelectric response of Metglas/Polyvinylidene fluoride laminates by exploiting the flux concentration effect," *Applied Physics Letters*, vol. 95, 112903, 2009.
- [31] J. Zhai, Z. Xing, S. Dong, J. Li, and D. Viehland, "Detection of pico-Tesla magnetic fields using magnetoelectric sensors at room temperature," *Applied Physics Letters*, vol. 88, 062510, 2006.
- [32] S. Dong, J. Zhai, J. Li, D. Viehland, "Near-ideal magnetoelectricity in high-permeability magnetostrictive piezofibere laminates with a (2-1) connectivity," *Applied Physics Letters*, vol. 89, 252904, 2006.
- [33] Y. Wang, D. Gray, D. Berry, J. Gao, M. Li, F. Li, and D. Viehland, "An extremely low equivalent magnetic noise magnetoelectric sensor," *Advanced Materials*, vol. 23, pp. 4111-4114, 2011.
- [34] Q. Wang, Q. Zhang, B. Xu, R. Liu, and L. Cross, "Nonlinear piezoelectric behavior of ceramic bending mode actuators under strong electric fields," *Journal of Applied Physics*, vol. 86, no. 6, pp. 3352-3360, 1999.

- [35] Q. Wang, X. Du, B. Xu, and L. Cross, "Electromechanical coupling and output efficiency of piezoelectric bending actuators," *IEEE Transaction of Ultrasonics, Ferroelectrics and Frequency Control*, vol. 46, pp. 638-646, 1999.
- [36] Q. F. Zhou, E. Hong, R. Wolf, and S. Trolier-McKinstry, "Dielectric and piezoelectric properties of PZT 52/48 thick films with (100) and random crystallographic orientation," *Proceedings of Materials Research Society Symposium*, vol. 655, cc11.7, 2000.
- [37] Q. Q. Zhang, Q. F. Zhou, and S. Trolier-McKinstry, "Structure and piezoelectric properties of sol-gel-derived  $0.5\text{Pb}[\text{Yb}_{1/2}\text{Nb}_{1/2}]\text{O}_3$ - $0.5\text{PbTiO}_3$  thin films," *Applied Physics Letters*, vol. 80, no. 18, pp. 3370–3372, 2002.
- [38] Q. F. Zhou, Q. Q. Zhang, T. Yoshimura, and S. TrolierMcKinstry, "Dielectric and transverse piezoelectric properties of sol-gel-derived (001)-oriented  $\text{Pb}[\text{Yb}_{1/2}\text{Nb}_{1/2}]\text{O}_3$ - $\text{PbTiO}_3$  epitaxial thin films," *Applied Physics Letters*, vol. 82, no. 26, pp. 4767–4769, 2003.
- [39] Q. F. Zhou, Q. Q. Zhang, and S. Trolier-McKinstry, "Structure and piezoelectric properties of sol-gel-derived (001)-oriented  $\text{Pb}[\text{Yb}_{1/2}\text{Nb}_{1/2}]\text{O}_3$ - $\text{PbTiO}_3$  thin films," *Journal of Applied Physics*, vol. 94, no. 5, pp. 3394–3402, 2003
- [40] T. Zhu, P. Argyrakis, E. Mastropaolo, K. K. Lee, and R. Cheung, "Dry etch release processes for micromachining applications," *Journal of Vacuum Science & Technology B*, vol. 25, pp. 2553, 2007.
- [41] S. Trolier-McKinstry and P. Murali, "Characterization and aging response of the d31 piezoelectric coefficient of lead zirconate titanate thin films," *Journal of Applied Physics*, vol. 85, no. 9, 1999.
- [42] F. Lochon, I. Dufour, and D. Rebière, "An alternative solution to improve sensitivity of resonant micro cantilever chemical sensors: comparison between using high-order modes and reducing dimensions," *Sens. Actuators B*, vol. 108, pp. 979, 2005.

- [43] F. Li, Z. Fang, R. Misra, S. Tadigadapa, Q. M. Zhang, and S. Datta, "Giant Magnetoelectric Effect in Nanofabricated  $\text{Pb}(\text{Zr}_{0.52}\text{Ti}_{0.48})\text{O}_3\text{-Fe}_{0.85}\text{B}_{0.05}\text{Si}_{0.1}$  Cantilevers and Resonant Gate Transistors," *Device Research Conference*, vol. 37, no. 69, 2011.
- [44] F. Li, Z. Fang, R. Misra, S. Tadigadapa, Q. M. Zhang and S. Datta, "Giant Magnetoelectric effect in nanofabricated  $\text{Pb}(\text{Zr}_{0.52}\text{Ti}_{0.48})\text{O}_3\text{-Fe}_{85}\text{B}_5\text{Si}_{10}$  cantilevers," *International Workshop on Acoustic Transduction Material and Devices*, 2011.
- [45] H. C. Nathanson, W. E. Newell, R. A. Wickstrom, and Davis J. R. Jr., "The Resonant Gate Transistor," *IEEE Transactions on Electron Devices*, vol. 14, no.3, pp.117-133, 1967.
- [46] F. Li, R. Misra, Z. Fang, Y. Wu, Q. M. Zhang, P. Schiffer, S. Tadigadapa and S. Datta, "Magnetoelectric Resonant Gate Transistor", submitted to *IEEE Journal of Microelectromechanical Systems*, 2012.
- [47] J. L. Wallace, "Applications of sputtered thin films of magnetoelastic amorphous alloys," *Materials & Design*, vol. 14, no. 5, 1993.
- [48] M. Cořson, C. Appino, F. Celegato, A. Magni, P. Tiberto, and F. Vinai, "Magnetization processes in sputtered FeSiB thin films," *Physical Review B*, vol. 77, 214404, 2008.
- [49] J. S. Pulskamp, A. Wickenden, R. Polcawich, B. Piekarski, and M. Dubey, "Mitigation of residual film stress deformation in multilayer microelectromechanical systems cantilever devices," *Journal of Vacuum Science & Technology B: Microelectronics and Nanometer Structures*, vol. 21, no. 6, pp. 2482-2486, 2003.
- [50] Y. Lu, and A. Nathan, "Thin film magnetostrictive sensor with on-chip readout and attofarad capacitance resolution," *IEEE International Electron Devices Meeting*, pp. 777-780, 1996.
- [51] M. J. Caruso, T. Bratland, C. H. Smith, R. Schneider, Honeywell, Inc.
- [52] Z. P. Xing, J. Li, and D. Viehland, "Noise and scale effects on the signal-to-noise ratio in magnetoelectric laminate sensor/detection units," *Applied Physics Letters*, vol. 91, pp. 182902–182902–3, 2007

- [53] Z. P. Xing, J. Li, and D. Viehland, "Modeling and the signal-to-noise ratio research of magnetoelectric sensors at low frequency," *Applied Physics Letters*, vol. 91, pp. 142905–142905–3, 2007
- [54] A
- [55] F. N. Hooge, T. G. M. Kleinpenning, and L. K. J. Vandamme, "Experimental studies on 1/f noise," *Rep. Prog. Phys.*, vol. 44, no. 5, pp. 497–532, 1981.
- [56] H. Mikoshiba, "1/f noise in n-channel silicon-gate MOS transistors," *IEEE Transactions on Electron Devices*, vol. ED-29, pp. 965–970, June 1982.
- [57] C. Jakobson, I. Bloom, and Y. Nemirovsky, "1/f noise in CMOS transistors for analog applications from subthreshold to saturation," *Solid-State Electronics*, vol. 42, no. 10, pp. 1807–1817, 1998.
- [58] K. Y. Yasumura, T. D. Stowe, E. M. Chow, T. Pfafman, T. W. Kenny, B. C. Stipe, and D. Rugar, "Quality Factors in Micron and Submicron Thick Cantilevers," *Journal of Microelectromechanical Systems*, vol. 9, no. 1, 2000.
- [59] S. Pamidighantam, R. Puers, K. Baer and H. A C Tilmans, "Pull-in voltage analysis of electrostatically actuated beam structures with fixed–fixed and fixed–free end conditions," *Journal of Micromechanics and Microengineering*, vol. 12, pp. 458–464, 2002.
- [60] D. M. Dagenais and F. Bucholtz, "Measurement and origin of magnetostrictive noise limitation in magnetic fiber-optic sensors", *Optics Letters*, vol. 19, no. 21 , 1994
- [61] F. Li, S. H. Lee, Z. Fang, P. Majhi, Q. M. Zhang, S. K. Banerjee, and S. Datta, "Flicker Noise Improvement in 100 nm  $L_g$   $Si_{0.50}Ge_{0.50}$  Strained Quantum-Well Transistors using Ultra-Thin Si Cap Layer," *IEEE Electron Device Letters*, vol. 31, no. 47, 2010.
- [62] R. Chau, B. Doyle, S. Datta, K. Kavalieros and K. Zhang, "Integrated nanoelectronics for the future," *Nature Materials*, vol 6, pp. 810-812, 2007.

- [63] S.H. Lee, P. Majhi, J. Oh, B. Sassman, C. Young et al "Demonstration of  $L_g \sim 55$  nm pMOSFETs with Si/Si<sub>0.25</sub>Ge<sub>0.75</sub>/Si Channels, high  $I_{on}/I_{off}$  ( $> 5 \times 10^4$ ), and controlled short channel effects (SCEs)," *IEEE Electron Device Letters*, vol. 29, no. 9, pp. 1017-1020, Jul. 2008.
- [64] S-H. Lee, J. Huang, P. Majhi, S.K. Banerjee, R. Jammy et al, "V<sub>th</sub> Variation and Strain Control of High Ge% Thin SiGe Channels by Millisecond Anneal Realizing High Performance pMOSFET beyond 16nm node," *VLSI Symposium Technology Digest*, pp. 74-75, Jun. 2009.
- [65] M. von Haartman, A. C. Lindgren, P. E. Hellstrom, B. G. Malm, S. L. Zhang, and M. Ostling, "1/f noise in Si and Si<sub>0.7</sub>Ge<sub>0.3</sub> pMOSFETs," *IEEE Transaction on Electron Devices*, vol. 50, no. 2, pp. 2513–2519, Dec. 2003.
- [66] T. Tsuchiya, T. Matsuura, and J. Murota, "Low-frequency noise in Si<sub>1-x</sub>Ge<sub>x</sub> p-channel metal–oxide–semiconductor field-effect transistors," *Japanese Journal of Applied Physics*, vol. 40, no. 9A, pp. 5290–5293, Sept. 2001.
- [67] A. D. Lambert, B. Alderman, R. J. P. Lander, E. H. C. Parker, and T. E. Whall, "Low frequency noise measurements of p-channel Si<sub>1-x</sub>Ge<sub>x</sub> MOSFET's," *IEEE Transaction on Electron Devices*, vol. 46, no. 7, pp. 1484-1486, Jul. 1999.
- [68] M. J. Prest, M. J. Palmer, G. Braithwaite, T. J. Grasby, P. J. Phillips, O. A. Mironov, E. H. C. Parker, and T. E. Whall, "Si/Si<sub>0.64</sub>Ge<sub>0.36</sub>/Si pMOSFETs with enhanced voltage gain and low 1/f noise," *Proceedings of European Solid-State Device Research Conference*, Nuremburg, Germany, pp. 179–182, Sept. 11–13, 2001.
- [69] Y. J. Song, J. W. Lim, B. Mheen, S. H. Kim, H. C. Bae, J. Y. Kang, J. H. Kim, J. I. Song, K. W. Park, and K. H. Shim, "1/f noise in Si<sub>0.8</sub>Ge<sub>0.2</sub> pMOSFETs under Fowler–Nordheim stress," *IEEE Transaction on Electron Devices*, vol. 50, no. 4, pp. 1152–1156, Apr. 2003.

- [70] Y. Jiang, W. Y. Loh, D. S. H. Chan, Y. Z. Xiong, C. Ren, Y. F. Lim, G. Q. Lo, and D.-L. Kwong, "Flicker Noise and Its Degradation Characteristics Under Electrical Stress in MOSFETs With Thin Strained-Si/SiGe Dual-Quantum Well," *IEEE Electron Device Letters*, vol 28, no 8, Jul. 2007.
- [71] R. Yang, Y. Xiong, W. Y. Loh, J.D. Ye et al, "Degradation of low frequency noise in SiGe and SiGe-C surface channel p-type MOSFET due to consuming the Si cap," *Applied Physics Letter*, vol. 91, pp. 233505-1, 2007.
- [72] E. Simoen, P. Verheyen, A. Shickova, R. Loo and C. Claeys "On the low-frequency noise of pMOSFETs with embedded SiGe source/drain and fully silicided metal gate," *IEEE Electron Device Letters*, vol. 28, no. 11, 2007.
- [73] G\_erard Ghibaudo, Jan Chroboczek, "On the origin of the LF noise in Si/Ge MOSFETs", *Solid-State Electronics*, vol. 46, pp. 393–398, 2002.
- [74] M. von Haartman, et al., "Low-frequency noise and Coulomb scattering in Si<sub>0.8</sub>Ge<sub>0.2</sub> surface channel pMOSFETs with ALD Al<sub>2</sub>O<sub>3</sub> gate dielectrics," *Solid-State Electronics*, vol. 49, pp. 907–914, 2005.
- [75] Martin von Haartman, B. Gunnar Malm, and Mikael Östling, "Comprehensive Study on Low-Frequency Noise and Mobility in Si and SiGe pMOSFETs With High-κ Gate Dielectrics and TiN Gate," *IEEE Transaction on Electron Devices*, vol. 53, no. 4, 2006
- [76] J. Karki, "Signal Conditioning Piezoelectric Sensors," *Application Report*, Texas Instrument, 2000
- [77] Z. P. Xing, J. Y. Zhai, S. X. Dong, J. F. Li, D. Viehland and W. G. Odendaal, "Modeling and detection of quasi-static nanotesla magnetic field variations using magnetoelectric laminate sensors," *Measurement and Science Technology*, vol. 19, pp. 015206, 2008.
- [78] Z. Fang, F. Li, N. Mokhariwale, S. Datta, and Q. M. Zhang, "Direct integration of magnetoelectric sensors with microelectronics improved field sensitivity, signal-to-noise

ratio and frequency response," pp.15-16, *IEEE Sensors 2010 Conference*, pp. 614-619, Waikoloa, Hawaii, November 2010

- [79] P. Ripka, "Advances in magnetic field sensors", *IEEE Sensors Journal*, Vol. 10, No. 6, 2010.
- [80] P. Ripka, "Sensors based on bulk soft magnetic materials: Advances and challenges, " *JMMM*, vol. 321, pp. 2466-2473, 2008.
- [81] A. E. Clark and D. N. Crowder, "High Temperature Magnetostriction of  $\text{TbFe}_2$  and  $\text{Th}_{.27}\text{Dy}_{.73}\text{Fe}_2$ ," *IEEE Transactions on Magnetics*, 21 1945, 1985
- [82] T. Takahashi, T. Okazaki and Y. Furuya, *Scr. Mater.* 61, 5–7, 2009.
- [83]

## Appendix A

### Metglas®/PZT ME Cantilever Process Flow

Sequence	Process	Material	Conditions
1	(111) Pt/Ti/SiO <sub>2</sub> /Si wafers (80nm/20nm/400nm/500μm) pre-conditioning prior to PZT deposition	1. Acetone 2. IPA	1. 10 min 30-40 °C 2. 5 min at Room Temperature 3. Rinse in DI water 4. low dry with N <sub>2</sub> 5. Pre-anneal 60s at 500 °C
2	PZT deposition	1. PZT solution	1. a Spin 1500 rpm for 30 s 1. b bake 250 °C and 400 °C- 1min 1. c Anneal at 700 °C 1. d Repeat above to 0.93 μm
3	Photoresist Coating (bi-layer)	1. SF 6 2. 3012	1. a Spin 3500 rpm for 45 s (~750 nm) 1. b Bake 200 °C and cool for 1min 2. a Spin 4000 rpm for 45 s (~1.5 μm) 2. b Bake 95 °C and cool for 1min
4	Contact lithography (mask 1)	MA/BA 6	Density: 8mW/cm <sup>2</sup> Time : 7.5 s (Resolution = 1 μm)
5	Develop 3012	CD 26	Dip for 1 min and rinse

6	Deep UV	Deep UV	900s
7	Develop SF 6	101A	Dip for 2 min and rinse
8	Kurt Lesker sputter and lift-off	Pt Metglas® Cr/Au Lift-off	2.5 mTorr 200 W 150s (60nm) 2.5 mTorr 150 W 2 hrs (260 nm) 2.5 mTorr 200 W 300 s (10/50nm) Dip in remover PG (overnight)
9	PR coating	SPR 220	4000 rpm 45s Bake 95 °C, 115 °C, 95 °C for 90 s
10	Contact lithography (mask 2)	MA/BA 6	Density: 8mW/cm <sup>2</sup> 10 s exposure, 10 s wait (5 times)
11	Develop	CD 26	Wait 30 min after exposure Dip for 2 min
12	Bottom electrode etch (PZT etch)	Tegal 6540	Ar/Cl <sub>2</sub> 45/7 sccm 5 mTorr 500 W at 13.56 MHz 30 s etch, 60 s cool (14 times)
13	Repeat 9-10 for mask 3		
14	Cantilever etch for release (PZT/Pt/Ti/SiO <sub>2</sub> )	Tegal 6540 Pt/Ti  SiO <sub>2</sub>	Repeat 12 Cl <sub>2</sub> /Ar/CF <sub>4</sub> 20/40/28 sccm 5 mTorr 500 W at 13.56 MHz 80 s etch CF <sub>4</sub> 155 sccm 5 mTorr 500 W at 13.56 MHz 3 min
15	Release	Xactix	XeF <sub>2</sub> 3 Torr for 60 s (40 cycles)

## Appendix B

### Metglas<sup>®</sup> MEFGT Process Flow

Sequence	Process	Material	Conditions
1	Pre-cleaning prior to SiO <sub>2</sub> deposition on Si substrate (10 <sup>17</sup> boron doped single side polished 100 Si wafer)	1. Acetone 2. IPA 3. SC1 4. SC2	1. 10 min 30-40 °C 2. 5 min at Room Temperature 3. 10 min 85 °C 4. 10 min 85 °C 5. HF dip (H <sub>2</sub> O:HF 50:1) 6. Rinse
2	Wet thermal oxidation	H <sub>2</sub> O	furnace 1050 °C for 3 hrs (~1µm)
3	Photoresist Coating	3012	a dehydration bake 5min 110 °C b Spin 4000 rpm for 45 s (~1.5 µm) c Bake 95 °C and cool for 1min
4	Contact lithography (mask 1 S/D)	MA/BA 6	Density: 8mW/cm <sup>2</sup> Time : 8 s (Resolution = 1 µm)
5	Develop 3012	CD 26	Dip for 1 min and rinse Post bake 120 °C for 2min
6	Oxide etch for S/D window	BOE(6:1)	Dip for 10 min (till back side of Si is hydrophobic )
7	Remove resist	Remover PG	Dip till PR is gone and rinse
8	Diffusion	POCl <sub>3</sub>	Repeat pre-cleaning sequence 1 Pre-deposition 1000 °C 20 min

			Drive in 1050 °C 30 min in O <sub>2</sub>
9	Contact lithography (mask2 gate oxide)	MA/BA 6	Repeat 3-5 using mask 2
10	Oxide etch for gate window	BOE(6:1)	Repeat sequence 6-7
11	Gate dielectric deposition	O <sub>2</sub>	Repeat pre-cleaning sequence 1 Furnace 950 °C 30min (~22nm) Post anneal in N <sub>2</sub> 30 min
12	Contact lithography (mask3 contact via)	MA/BA 6	Repeat 3-5 using mask 3
13	Oxide etch for contact via	BOE(6:1)	Dip for 3 min (till back side of Si is hydrophobic )
14	Metal contact lift-off (Mask 4 metal)	MA/BA 6 Pt/Ti	Repeat 3-5 using mask 4 2.5 mTorr 200 W 300s Dip in remover PG (overnight)
15	Amorphous Silicon	PECVD	Ar/SiH <sub>4</sub> 400/25 sccm 2 Torr 220 °C 360 s (~500 nm)
16	Photoresist Coating (bi-layer)	1. SF 6 2. 3012	1. a Spin 3500 rpm for 45 s (~750 nm) 1. b Bake 200 °C and cool for 1min 2. a Spin 4000 rpm for 45 s (~1.5 μm) 2. b Bake 95 °C and cool for 1min
17	Contact lithography (mask 5)	MA/BA 6	Density: 8mW/cm <sup>2</sup> Time : 7.5 s (Resolution = 1 μm)

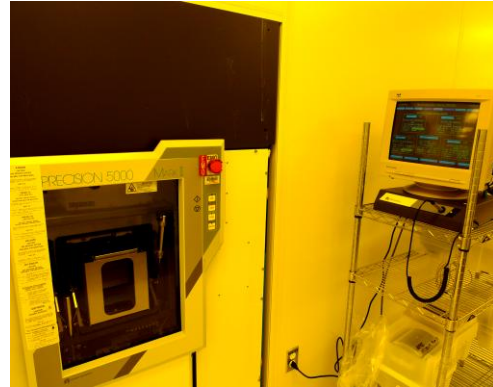
18	Develop 3012	CD 26	Dip for 1 min and rinse
19	Deep UV	Deep UV	900s
20	Develop SF 6	101A	Dip for 2 min and rinse
21	Kurt Lesker/Ion mill sputter and lift-off	Ti Metglas <sup>®</sup> Pt Lift-off	2.5 mTorr 200 W 1500s (500 nm) 0.5 mTorr 45 W 1 hrs (100 nm) 2.5 mTorr 200 W 50 s (20 nm) Dip in remover PG (overnight)
22	Contact lithography (mask 6)	MA/BA 6	Density: 8mW/cm <sup>2</sup> Time : 7.5 s (Resolution = 1 μm)
23	Release	Xactix	XeF <sub>2</sub> 3 Torr for 60 s (20 cycles)
24	PR remove	M4L	O <sub>2</sub> 45 sccm Plasma 100 W, 5 min

## Appendix C

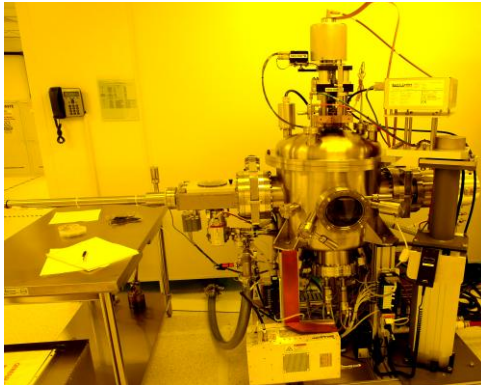
### Process Facilities



Thermal Oxide Furnace



Precision 5000 Plasma Enhanced Chemical Vapor Deposition



Kurt Lesker Sputter Deposition



Tegal 6500 Oxide Reactive Ion Etching



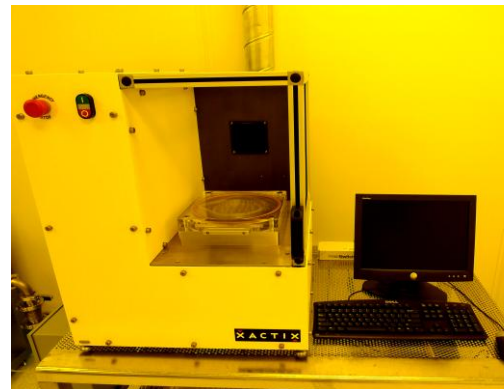
Karl Suss MA 6/BA 6 Contact Aligner



Gemini Leo Scanning Electron Microscopy



Reactive Ion Etching M4L



XACTIX Xef2 Deep Silicon Etcher

## **VITA**

### **Feng Li**

Feng Li was born in Harbin, China on June 26, 1986. Prior to Penn State, he received B.S. degree in Electrical Engineering from Tsinghua University, Beijing, China in 2008. He began his Ph.D. study in the department of Electrical Engineering from Aug. 2008 with Dr. Suman Datta. His research interests include thin film integrated magnetometers for biomedical imaging application, novel device/transistor modeling, and in-situ process for ferromagnetic thin film electronics.